A measurement of the Inclusive Branching Fraction for the Radiative B Meson Decay $B \to X_s\gamma$ with the Belle Detector

by
Yutaka Ushiroda

A Dissertation Submitted
in Partial Fulfillment
of the
Requirements for the Degree of
Doctor of Science (Physics)

Graduate School of Kyoto University
Kitashirakawa, Kyoto.

Acknowledgments

This thesis work is never the only effort of mine, rather so many people has helped to complete this. I am quite thankfull to all who have helped me at a variety of levels. My sincere apology is to all those whom I forgot to acknowledge in this short list.

First of all, I would like to express my deep gratitude to my supervisor Prof. N. Sasao and Prof. H. Sakamoto of Kyoto university, for picking me up in the experimental world of high energy physics. I have been working mainly at KEK, away from Kyoto, but I know I was always under their umbrellas.

I am grateful to Prof. K. Nishikawa, Dr. T. Nomura, Dr. T. Nakaya of Kyoto university. Since we have been working for different experiments we could not have frequent discussions, but still I could get some critical advice from time to time.

I am grateful to all the members of our university group. I could learn many things from senior students, Suehiro-san, Takeuchi-san, Murakami-san, and Mato-san. My colleagues, H. R. Sakai, Inagaki, and Akky have been good rivals. We could discipline and improve each other. Also, I had been quite encouraged to be a good example for junior students; Yumura, N6, Yoko6, Honda-kun, Issei, Mizouchi, Kirika and Maesaka. I was not quite *kind* or *tender* to them; I'm afraid it might have been a bit pain for some of them.

I am deeply thankful to the secretary Ms. T. Ishino (Kiyosawa) and Ms. A. Nakao of our department, Ms. K. Nakagawa, Ms. A. Saito and all the secretariat members of the department, for taking care of every official/private businesses, while I'm not in Kyoto.

I express my heartfelt gratitude and thanks to Prof. Y. Sakai of KEK, without whose supervision I wouldn't have survived in the high energy physics society. I have learnt many things from his sincere attitude to experiment, prudent way of analysis, diligence in daily work. His guidance not in eloquent lips but in his manner as a physicist encouraged and led me to where I am today.

I express my deep gratitude to Dr. M. Nakao. He taught me a lot of things related to B physics, not only the radiative B decay physics. Discussion with him never allows me a compromise, and I was quite encouraged to do strict analysis by his supervision. I bet I could not have finished this analysis without his advice. I must not forget to thank him for bottles of nice wines, too!

I would like to thank to the internal referees, Prof. W. Bartel, Prof. H. Aihara and Prof. K. Miyabayashi, who helped me to submit the paper on this analysis. They were very quick to understand what has been done in my analysis and what is necessary in the paper.

I am deeply thankful to all the members of the Belle collaboration and the KEKB group for their cooperation and hard working. I would like to thank the members of the DCPV/Rare

group and the Trigger/DAQ group for their generous help and valuable suggestions at each step. I am specially grateful to Dr. M. Nakao, Mr. L. Moffitt, Dr. H. Ikeda, Dr. R. S. Lu, Mr. S. Nishida, Prof. T. E. Browder, Mr. B. C. K. Casey, Dr. T. Iijima, Prof. Y. Sakai, Dr. Y. Iwasaki, Dr. E. Nakano, Dr. M. Tomoto, Dr. S. Uehara, Dr. M. Tanaka, Prof. M. Yamauchi, Dr. R. Itoh, Dr. S. Y. Suzuki, Prof. B. G. Cheon, Mr. H. J. Kim for discussions and advice.

I would like to acknowledge and thank all the students worked together in a busy period of construction of the Belle detector taking just a nap even in the laboratory. I am grateful to Tsujita-san, Kawasaki-san, Sumisawa-san, Takeo-chan, Yokoyama-kun, J. Tanaka-kun, Tomura-kun, Nakadaira-kun, Tomoto-san, Yoshida-san, Okabet, Ishikawa, Akatsu, Hirano-san, Kuniboo, K. Suzuki-kun, Unno-kun, Ikeda-san, Syunsuke, Kakuno-kun, Nishida, Ajit, Asish, ChulSu-hyung, HeeJong, Ahn-san, DonUk, HyunWoo, HyunKi, Nam-san, SangHee, ChaWon, TaeHang, Lu-san, Huang-san, Brendan, Leon, for their friendship and *occasional* diversion. We had many fruitful discussions on physics, hardware, software; and sometimes on politics, economics, history and international situations. Some of my foreign friends taught me their mother tongue and cooked their folk dishes for me. I hope we can get together working for high energy phisics in somewhere, some future, again.

I express my sincere gratitude to the secretary of the collaboration Ms. R. Ohta, for making conveniences in my KEK life.

I would like to acknowledge to Mr. H. Matsuo in heaven, who joined to the collaboration from the same university, worked together, studied together, but unfortunately deceased on the way. He worried that the theory and the experiment of the elementary particle physics are too far apart in the energy scale, and wanted to obtain more experimental facts for an effective and helthful development of the field. I live in this field and respect for his wish. I pray his soul may rest in peace.

Finally, I can't thank my family enough for love and support they have given me through the years. I owe much to my parents to continue the years of the student life at the graduate school in Japan. My brother is really a steady and smart guy that I can dedicate to the study without worry. My wife has been always a source of encouragement; without her devotional support, I could not have made up this thesis. And finally, my dear daughter drove me finalizing this work.

Sincerely,
Yutaka USHIRODA

Kyoto, Japan
May 11, 2001.

Abstract

According to the Standard Model, the decay of a b quark into an s quark in a tree level diagram through a direct Z emission is not allowed. As the lowest order diagram, we have a one loop flavor changing neutral current process, where the loop is dominantly mediated by virtual W and t. Instead of W and t, charged Higgs or other non-Standard-Model particles can contribute. The presence of such additional contributions may either enhance or suppress the branching ratio for $B \to X_s\gamma$. A measurement of the branching ratio for $B \to X_s\gamma$, therefore, provides a precise testing ground of the Standard Model, and constrains the parameters for extensions of the Standard Model.

In this thesis, the inclusive branching ratio of $B \to X_s\gamma$ process is measured. The measurement is based on 5.84fb^{-1} of data collected on the Υ(4S) resonance by the Belle detector at the KEKB e^+e^- storage ring.

The signal contains a prominent semi-monochromatic hard photon since it is from a quasi-two-body decay of a B meson. The recoil system (X_s) that carries the strangeness is semi-inclusively reconstructed from one kaon plus one to four pions. The contribution from modes which are not reconstructed by these combinations is extrapolated by a theory model. One inherent problem in the inclusive analysis is that there are possibly more than one X_s candidate in an event. Here, the advantage of our vertex detector is used to select the best candidate.

The largest background come from light quark pair production ($e^+e^- \to q\bar{q}$). In order to suppress the $q\bar{q}$ background, a new event shape variable called SFW has been developed. The $q\bar{q}$ background contribution is estimated from the SFW sideband data, which provides a pure sample of $q\bar{q}$ events.

We determined the branching ratio for $B \to X_s\gamma$ as

$$\mathcal{B}(B \to X_s\gamma) = (\ 3.36 \pm 0.53 \pm 0.42\ ^{+0.50}_{-0.54}\ ) \times 10^{-4}$$

where the first error term is the statistical error, the second is the systematic error and the third is the theoretical error.

Contents

List of Figures

List of Tables

Chapter 1

Introduction

In the long history of human beings, there has been a profound theme of elementary particle physics : that is a pursuit of the ultimate component of matter and the relating laws or principles. Dēmokritos'[1] atomism was embodied experimentally by Boyle[2] , who became the pioneer of the systematical and analytical study of particle physics. Mendeleev[3] listed up more than hundred of atoms periodically, which turned out that the periodic pattern was imposed by the Pauli[4] exclusion principle for electrons in an atom. The *ultimate* component of the time has changed era to era, and lows and principles have changed, too; however, our interest to the *ultimate* things has not changed.

The current view of physical world is that it is composed of spin 1/2 (fermion) and spin 1 (boson) particles which show no internal structure at least with our currently reachable resolutions. They interact by one or more of the three[5] fundamental forces – strong, electromagnetic and weak – via an exchange of spin 1 particles. The fermions are grouped by the types of charge it has. All the fermions carry the weak charge and therefore interact via weak force. The fermions which have the charge of strong (color charge) are called quarks. Only quarks can interact via strong force, and the rest of fermions are called leptons. These fundamental particles all exist around us. An ordinary matter, for e.g. a stone, an eraser, or your hands, consists of atoms, an atom consists of electrons (lepton) and a nucleus, a nucleus consists of nucleons and a nucleon consists of quarks. Also, we can find another type of leptons (muon) in cosmic rays showering onto our globe.

The Standard Model (SM) describes the interactions between these particles very well. Almost all the phenomena observed in high energy experiments could have been explained by the SM, although there is one big weakness in the SM; it does not predict the masses of the quarks and leptons, and hence it does not explain why there are three generations in the currently reachable mass region. As an interest of experimentalist, we thus search for any phenomena that disagrees with the SM prediction. Finding a tiny but critical fact that requires a perfect thing to be alternated is a big fun, like defeating the Yomiuri Giants[6].

One of the biggest issue left to be solved in the SM is the CP violation mechanism. A

[1] about B.C.460 - B.C.370

[2] 1627 - 1691

[3] 1834 - 1907

[4] 1900 - 1958

[5] Although gravity is the most familiar force to us, it is utterly negligible at the energy scale of subnuclear particles (*high* energy physics).

[6] A professional baseball team in Japan

CP violating phenomenon was observed in 1964 in a K meson system [1]. The mechanism of CP violation has been modeled by Kobayashi and Maskawa [2]. It is very beautiful and plausible model since it is built within the framework of the SM. Despite its beautifulness, its key parameters which form a matrix are not determined by the model itself. People call the matrix, heading another great physicist's name, Cabbibo-Kobayashi-Maskawa (CKM) matrix. This matrix represents a mixing of the weak and mass eigenstates of the quarks. The weak eigenstates of d, s, b quarks are the superposition of the mass eigen states of d, s, b. Labeling the weak state with a prime, the superposition is written as the following equation.

$$\begin{pmatrix} d' \\ s' \\ b' \end{pmatrix} = \begin{pmatrix} V_{ud} & V_{us} & V_{ub} \\ V_{cd} & V_{cs} & V_{cb} \\ V_{td} & V_{ts} & V_{tb} \end{pmatrix} \begin{pmatrix} d \\ s \\ b \end{pmatrix} \tag{1.1}$$

Determining these parameters and testing the Kobayashi-Maskawa model is one of the urgent tasks for experimentalists.

According to the SM, the CKM matrix is unitary and it forbids the decay of b quark into an s quark in a tree level diagram through a direct Z emission. As the lowest order of diagram, we have a one loop flavor changing neutral current (FCNC) process, which is a famous electroweak penguin diagram shown in Figure 1.1. Instead of a virtual W in Figure 1.1, a charged Higgs or other non-SM particles can mediate the loop. The presence of such additional contributions may either enhance or suppress the branching fraction for $B \to X_s\gamma$. A measurement of the branching fraction for $B \to X_s\gamma$, therefore, tests the SM precisely, and constrains extensions of the SM[3].

For example in the supersymmetric standard model, flavor mixing is also present in the squark sector. There are five classes of contributions to $B \to X_s\gamma$ in supersymmetric theories; the virtual exchange of (1) the up-type quarks and the W boson in the SM, (2) the up-type quarks and the charged Higgs ($H^{\pm}$), (3) the up-type squarks and charginos ($\tilde{\chi_i}^{\pm}$), (4) the down-type squarks and neutralinos ($\tilde{\chi_i}^{0}$), and (5) the down-type squarks and gluinos ($\tilde{g}$). The contributions from (1) and (2) are large and interfere constructively. The contributions from (4) and (5) are usually small in the minimal super symmetric model and are not competitive with those induced by W boson and $H^{\pm}$ exchange. On the other hand, the size and the relative sign of the chargino contributions (3) depend on the parameters of the chargino mass matrix and on those responsible for the masses and mixings of the squark sector; and for some range of the parameter space, it can cancel the charged Higgs contributions to give a value of $\mathcal{B}(B \to X_s\gamma)$ at or even below the SM prediction.

Recently, the next-to-leading order (NLO) QCD correction in $\alpha_s(m_b) \sim 0.2$ have been completed [4], resulting the branching fraction prediction with smaller error.

$$\mathcal{B}(B \to X_s\gamma) = (3.28 \pm 0.33) \times 10^{-4} \tag{1.2}$$

As for experimental results, the branching fraction is first measured by the CLEO collaboration with B mesons from Υ(4S) decay in 1995[5],

$$\mathcal{B}(B \to X_s\gamma) = (2.32 \pm 0.57 \pm 0.35) \times 10^{-4}, \tag{1.3}$$

followed by the ALEPH collaboration in hadronic Z decay[6],

$$\mathcal{B}(B \to X_s\gamma) = (3.11 \pm 0.80 \pm 0.72) \times 10^{-4}. \tag{1.4}$$

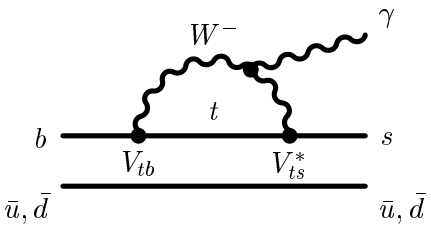

Figure 1.1: Electroweak Penguin Diagram – a virtual W is emitted and re-absorbed in way of b decays into s. The photon can be emitted from any of the charged particles except for the spectator quark.

All the experimental results so far are consistent with the SM prediction. The errors in these measurements are very large comparing to the error of the SM prediction (10%), and are limited mainly by the statistical error. Further investigation in an experiment with a large statistics is desired. A measurement of this branching fraction at the KEK B-factory is the main subject of this dissertation. In the following chapters, an introduction to a B-factory experiment is first given in Chapter 2. We then move to the analysis. The reconstruction mothod of $B \to X_s\gamma$ is described in Chapter 3. In Chapter 4, discussions on data analyses are given. We then discuss about our signal reconstruction efficiency in Chapter 5. Finally, we conclude in Chapter 6.

Chapter 2

B-factory

A B-factory produces a copious number of B mesons like a factory, which enables a detailed study of physics topics related to B meson; for example, CP violation, rare B decays, and so forth. Experimentally, it requires a high luminosity in order to study B decays of which typical cross section is about $\times 10^{-4} \sim \times 10^{-6}$ nb.

B-factory is a highlight of current particle physics and there are several B-factory projects in the world as listed in Table 2.1. This trend is led off with a success of the CLEO experiment and we – the Belle – and the BABAR experiments are now being blessed with plenty of data and studying various aspects of B physics.

CESR, PEP-II and KEKB are electron-positron colliders whose center of mass energy is targeting at the $\Upsilon(4S)$ resonance. Either of PEP-II and KEKB has two beam lines for e^+ and e^- separately, in order to achieve an asymmetric beam energy and produce boosted B mesons in our laboratory frame, while CESR is a symmetric beam energy collider.

Tevatron, HERA and LHC are hadronic machines. Characteristics of these experiments are (1) a large production cross section, (2) production of B_s and other higher B mesons, too, (3) a big boost of B mesons. An analysis on $J/\Psi K_s$ is clean enough and good to be done in hadron machines, but, a darty environment of hadron collision often makes the experiment and data analysis difficult.

The B-factory in Japan is built at KEK (High Energy Accelerator Research Organization, Tsukuba-city, Ibaraki-pre. Japan). Data taking has started in June, 1999. We have accumulated about $10.5\,\mathrm{fb}^{-1}$ of data by the end of 2000, and we could have extracted some physics results. In the following sections, relating issues on KEK B-factory project will be described. We introduce about $\Upsilon(4S)$ and B mesons, their cross sections, mass, width, and decays, in

Accelerator	Detector	Institute
CESR	CLEO III [7]	Cornell University
PEP-II	BABAR [8]	SLAC (Stanford Linear Accelerator Center)
KEKB	Belle [9]	KEK (High Energy Accelerator Research Organization)
Tevatron	BTeV [10]	FNAL (Fermi National Accelerator Laboratory)
HERA	HERA-B [11]	DESY (Deutsches Elektronen-Synchrotron)
LHC	LHCb [12]	CERN (European Laboratory for Particle Physics)

Table 2.1: B-factory projects in the world

Υ state	Mass (MeV/c^2)	Total Width (MeV)
$1S$	9460.30 ± 0.26	0.0525 ± 0.0018
$2S$	10023.26 ± 0.31	0.044 ± 0.007
$3S$	10355.2 ± 0.5	0.0263 ± 0.0035
$4S$	10580.0 ± 3.5	14.0 ± 5
$5S$	10865 ± 8	110 ± 13
$6S$	11019 ± 8	79 ± 16

Table 2.2: Properties of the Υ resonances (from the PDG tables [14])

section 2.1. In section 2.2, a brief introduction to our KEKB e^+e^- storage ring is given. In section 2.3, each components of the Belle detector is described. Finally, in section 2.4, issues on online/off-line filters of events (Trigger/DAQ, etc.) are described.

2.1 $\Upsilon(4S)$ mesons and B mesons

The Υ mesons are a family of spin 1 bound state of b and $\bar{b}$ quarks. P and C parities are both negative. Figure 2.1 shows the hadronic cross section for e^+e^- measured by CLEO and CUSB at the $\Upsilon(1S)$, $\Upsilon(2S)$, $\Upsilon(3S)$ and $\Upsilon(4S)$ resonances. The masses and widths of Υ mesons are listed up in Table 2.2.

Our experiment runs at the Υ(4S) resonance energy. More than 96% of Υ(4S) decays into B^+B^- or $B^0\bar{B}^0$ pairs. CLEO has measured the ratio of charged pair to neutral pair decay fractions using semileptonic B decays[15]. Result is consistent with equal production of B^+B^- and $B^0\bar{B}^0$ pairs,

$$\frac{\mathcal{B}(\Upsilon(4S) \to B^+B^-)}{\mathcal{B}(\Upsilon(4S) \to B^0\bar{B}^0)} = 1.04 \pm 0.07 \pm 0.04 \tag{2.1}$$

where the first error is statistic, the second is systematic.

Υ(4S) is not a sharp peak as the lower Υ resonances. The total width drastically changes from Υ(4S). This is because the lightest bottom meson channel ($B\bar{B}$ channel) opens at just below the Υ(4S) mass, and therefore the OZI (Okubo-Zweig-Iizuka) mechanism[13] that suppresses the width of lower three Υ mesons does not work for Υ(4S) and higher.

At the Υ(4S) peak position, signal to background ratio is about 1/3. Namely, we have three times larger cross section of $q\bar{q}$ light quark pair production background[1]. Most of the rare decay analysis of B meson suffer from this $q\bar{q}$ background. $B \to X_s\gamma$ is one of the severest analysis among them. How to treat the $q\bar{q}$ background is one of the main issue of this thesis. A traditional and the most reliable way is to study the $q\bar{q}$ background using the data at just off the Υ(4S) resonance. We actually take data at about 60 MeV below the Υ(4S) resonance, but not so eagerly at KEK B-factory as the CLEO experiment, because we have the highest priority in an urgent physics topics of the $\sin 2\phi_1$ measurement, in which we do not need the off-resonance data so much.

Figure 2.2 is a list of typical diagrams for B meson decays. A B meson mainly decays through a $b \to c$ transition. The dominant decay diagram is the external tree diagram shown

[1]Since its contribution is continuous in the energy region, we sometimes call it the continuum background.

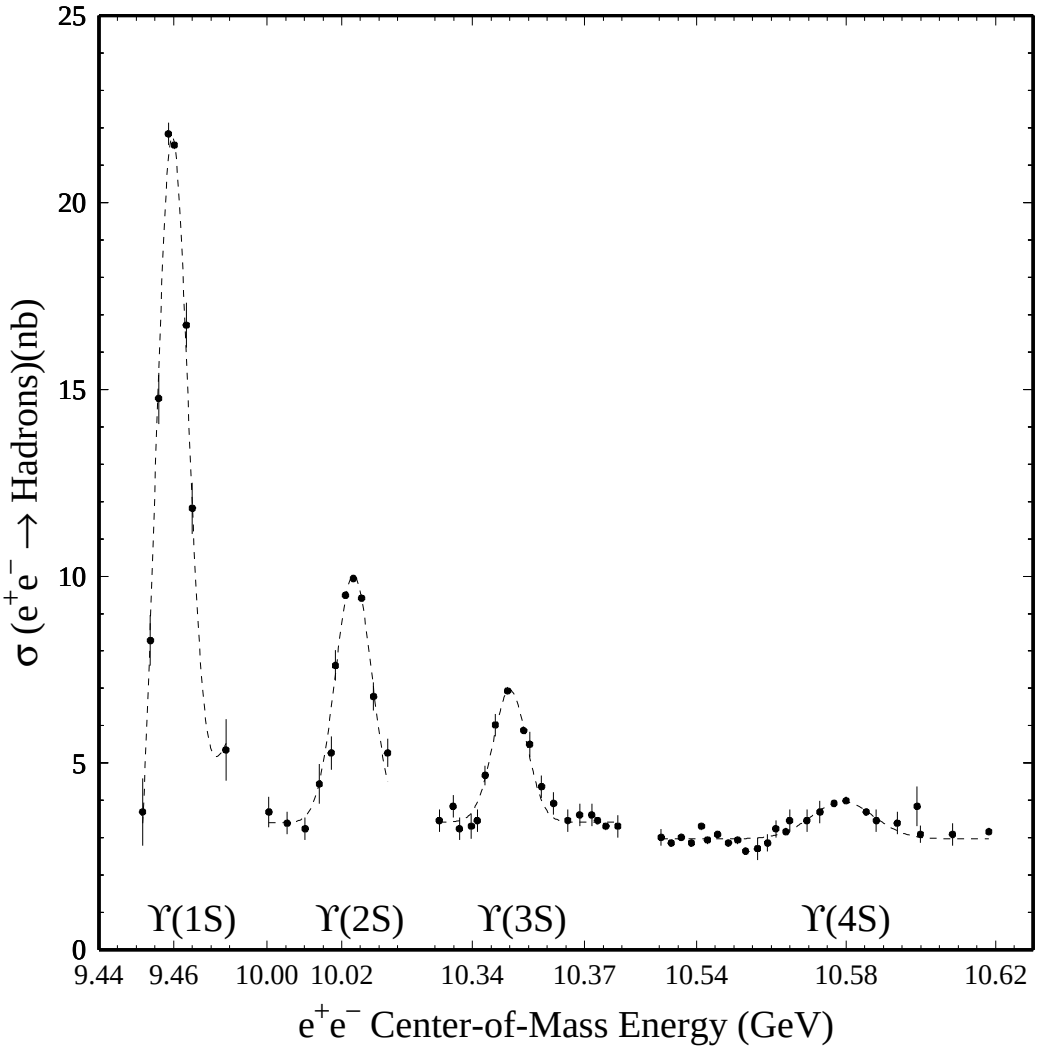

Figure 2.1: $e^+\,e^-$ cross section into hadrons measured by CLEO and CUSB – mass peaks of the Υ resonances can be seen.

in Figure 2.2(a), where a virtual W^- materializes either into a lepton pair (ℓ, ν_ℓ) that we call the semi-leptonic B decay or into a quark pair ($\bar{u}\,d$ or $\bar{c}\,s$) that we call the hadronic B decay.

The major difficulty in comparing an experimental result to a theory lays in the hadronization process of quarks. In such a sense, semi-leptonic B decays are less affected by hadronization processes than hadronic decays and give us the best matching of an experimental result and a theoretical calculation. This is one of the reasons why the $\mathcal{B}(B \to X_s\gamma)$ is often normalized with $\mathcal{B}(B \to X_c\ell\nu_\ell)$ in the theoretical calculation.

In a spectator hadronic decay, we obtain Figure 2.2(b) by pairing different quarks in the final state. In Figure 2.2(a), the color of quark pair from W^- decay can be any of $red - \overline{red}$, $green - \overline{green}$ or $blue - \overline{blue}$. On the other hand, in Figure 2.2(b), the final state quark pairs must carry the same color that the initial state quark pair had; thus, the decay of Figure 2.2(b) is color suppressed.

We define all the B meson decays which do not undergo via $b \to c$ transition as rare decays. The simplest diagram for a rare B decay is the spectator diagram with $b \to u$ transition shown in Figure 2.2(c). The branching fraction for this diagram is small due to the smallness of V_{ub}; we call when an amplitude of a diagram is small due to the smallness of the corresponding CKM matrix element that the diagram is CKM suppressed[2]. For instance, a semi-leptonic $b \to u$ decay $B \to \pi\ell\nu_\ell$ is observed by CLEO [16]. Comparing the branching fraction to that of $B \to D\ell\nu_\ell$, we see approximately the following relation.

$$\frac{\mathcal{B}(B \to \pi\ell\nu_\ell)}{\mathcal{B}(B \to D\ell\nu_\ell)} \simeq 10^{-2} \sim \left|\frac{V_{ub}}{V_{cb}}\right|^2$$

The one loop flavor changing neutral current (FCNC) diagram (or electroweak penguin diagram) of the $b \to s\gamma$ transition in question of this dissertation (Figure 2.2(d)) is also categorized in rare decays. The $b \to d\gamma$ transition can be written in the same way only by changing the s quark into d quark. Since V_{td} is small, this is further CKM suppressed. Decay via $b \to d\gamma$ transition has not been observed yet.

There are two more famous diagrams for rare decays; W-exchange Figure 2.2(e) and W-annihilation Figure 2.2(f). The lifetime of charged and neutral B mesons are similar because these two diagrams are highly suppressed, unlike the case of D mesons. Decays only via these diagrams have not been observed yet.

[2]Or, we call *Cabbibo suppressed* when the matrix element is in the 2×2 matrix upto the second generation, and *KM suppressed* when the matrix element is relevant to the third generation

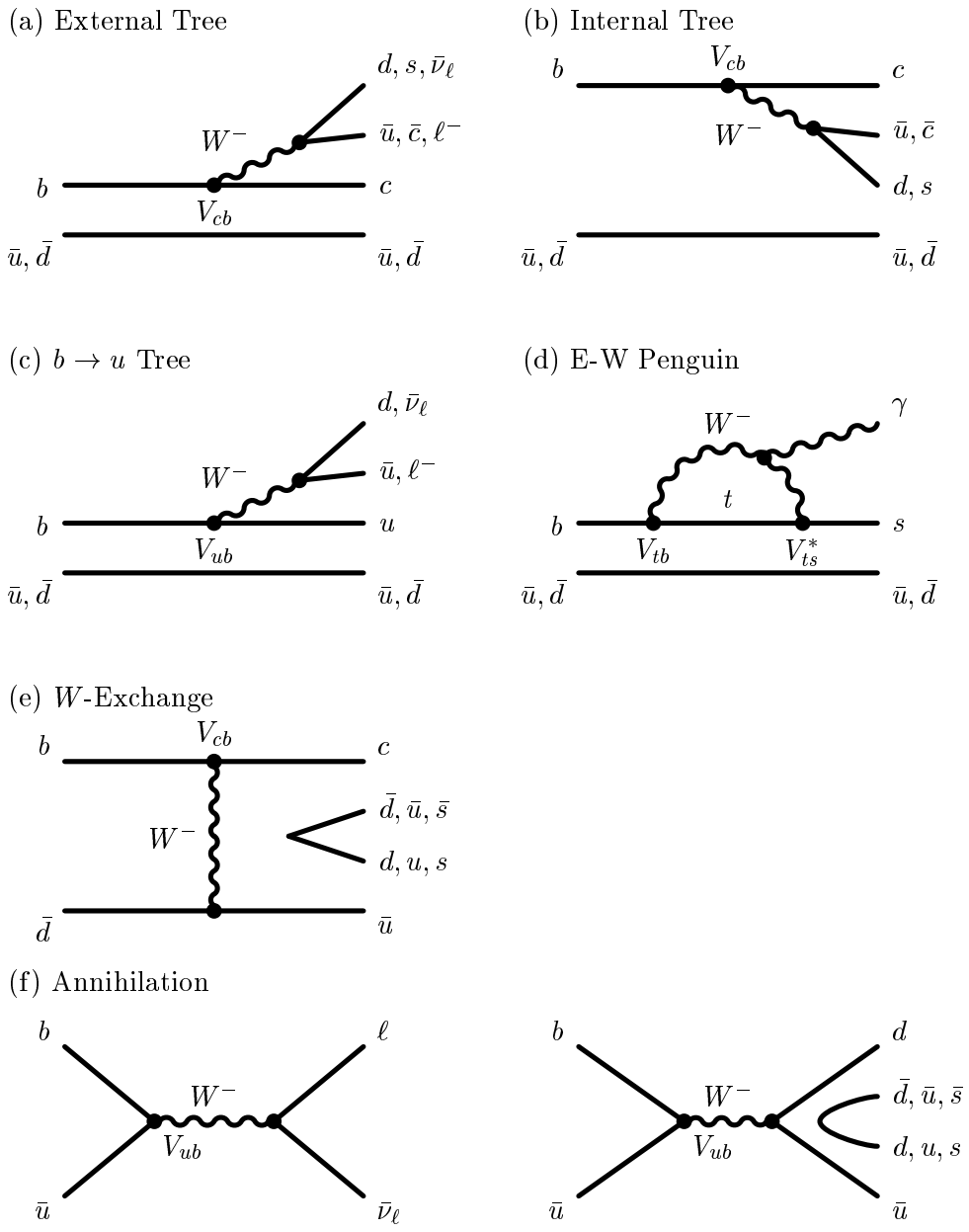

Figure 2.2: Diagrams for B meson decays – external spectator diagram (a), color suppressed spectator diagram (b), $b \to u$ spectator diagram (c), $b \to s\gamma$ electroweak penguin diagram (d) W-exchange diagram (e) and W-annihilation diagram (f).

2.2 KEKB Storage Ring

The main purposes of KEK B-factory project is to study CP violation at the B meson decay and to test the Kobayashi-Maskawa model. In order to observe a time dependent CP asymmetry, we need to know the decay time of each B meson. We actually measure the decay positions of B and $\bar{B}$ mesons, and therefore B mesons are necessarily being boosted toward one direction in our laboratory frame to make our measurement easier.

In order to produce largely boosted B meson pairs, the e^+ beam energy and the e^- beam energy (and momentum) must be asymmetric. If the e^+ and e^- beams have different momenta, they cannot have the same orbit in a common magnetic field, so KEKB is designed to have two seperate rings for e^+ and e^- beams. The e^+ and e^- rings were constructed side by side in the tunnel used for TRISTAN as shown in Figure 2.3. The e^+ and e^- beams are injected directly into the main rings at Fuji area from a linear accelerator. The e^+ beam circulates anti-clockwise with energy $E^+ = 3.5\,\mathrm{GeV}$, and the e^- beam circulates clockwise with energy $E^- = 8.0\,\mathrm{GeV}$. These two rings are called as the Low Energy Ring (LER) and the High Energy Ring (HER), respectively. The e^- beam is chosen to be high energy in order to avoid an ion trapping phenomenon [3]. It is an instability of an e^- beam due to an interaction with residual gas molecules in the vacuum chamber, from which the lower energy electron suffers more seriously. In Tsukuba-Oho-Fuji semicircle, HER(LER) placed outside(inside) and vice versa in Fuji-Nikko-Tsukuba semicircle, having two crossing points at Tsukuba and Fuji experimental hall. The two beams are made collide at the interaction point (IP) in the Tsukuba experimental hall, where the Belle detector is furnished; at Fuji, on the other hand, two beams are displaced vertically and pass through each other.

The center of mass energy is

$$\sqrt{s} = \sqrt{4E^+E^-} = 10.58\,\mathrm{GeV}. \tag{2.2}$$

This is equal to the invariant mass of $\Upsilon(4S)$ which decays into $B^0\bar{B}^0$ or B^+B^- pairs with more than 96% of branching fraction, so we can produce B mesons efficiently. The Lorentz boost parameter is

$$\beta\gamma = \frac{E^- - E^+}{\sqrt{s}} = 0.425. \tag{2.3}$$

For example, a boosted B^0 meson runs about $200\,\mu$m in average before it decays, since the lifetime($c\tau$) of a B^0 meson is $464\,\mu$m.

We have adopted a finite angle crossing scheme of ± 11 mrad for the IP. With this scheme, parasitic collisions will not be a concern. Also, we do not need separation magnets near the IP, and the design of the synchrotron light masks become simpler. The risk associated with this scheme is the possibility of luminosity loss caused by the excitation of synchro-beta resonances[17].

The design parameters of KEKB are listed in Table 2.3 [17]. The most important parameter for high energy physicists among them is the luminosity. The luminosity (L) can be

[3] After we started the operation, we found that the low energy e^+ beam suffers from an instability due to an interaction with e^- cloud. To avoid this instability, we have done and plan to do several ideas. We have wound solenoid coils around the vacuum chambers of LER in order to trap the e^- cloud. This improved the beam stability significantly. We plan to wind more solenoid coils, we also plan to introduce ante-chambers, and we have a plan to swap the energies of two beams in future.

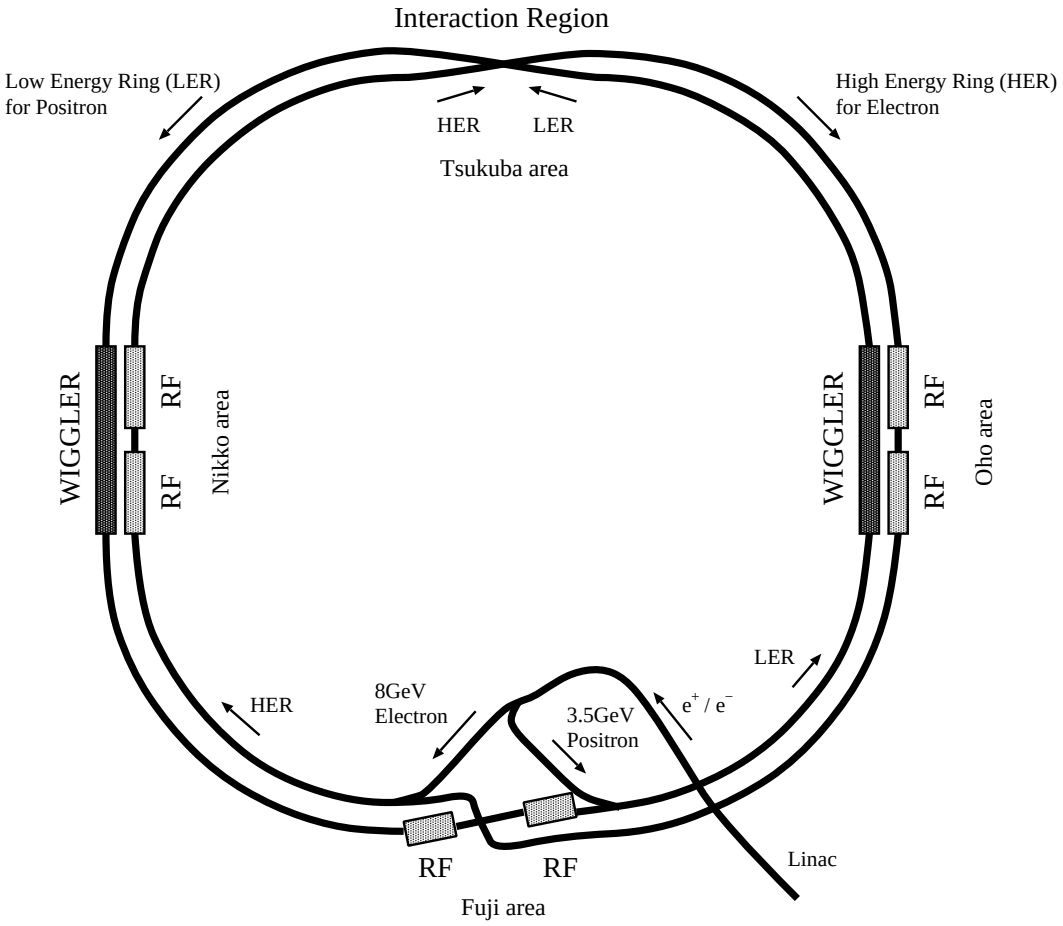

Figure 2.3: Configuration of the KEKB storage ring

expressed using the beam-beam tune shift parameter (ξ) as follows[18]. Although this is a equation for head-on collision, it is a good approximation for our finite angle crossing case[17], too.

$$L = \frac{N_+ N_- f}{4\pi\sigma_x^*\sigma_y^*} \tag{2.4}$$

$$= \frac{1+r}{2er_e}\frac{\gamma_\pm\xi_\pm I_\pm}{\beta_{y\pm}^*} \tag{2.5}$$

$$\xi_{x,y;\pm} = \frac{r_e N_\mp \beta_{x,y;\pm}^*}{2\pi\gamma_\pm\sigma_{x,y}^*(\sigma_x^*+\sigma_y^*)} \tag{2.6}$$

where

$\pm$: the suffix for $e^\pm$ beam, respectively
$N_\pm$: the number of the particles per bunch
f : the collision rate
$\sigma_{x,y}^*$: the beam sizes at the IP
r : the aspect ratio of the beam shape
1 for a round and 0 for a flat beam
e : the elementary electric charge
r_e : the classical electron radius
$\gamma_\pm$: Lorentz boost parameter
$I_\pm$: the circulating current
$\beta_{x,y}^*$: β functions

We have assumed that the beam sizes and the β functions of two beams are equal. This implies that $N_+\gamma_+ = N_-\gamma_-$, and hence the LER current is higher than the HER current. The design luminosity of KEKB is $10^{34}\,\mathrm{cm}^{-2}\,\mathrm{s}^{-1}$, which will be the world highest luminosity ever. In order to achieve high luminosity, we choose as large ξ's and as small β's as possible (Table 2.3). To obtain the target luminosity with these ξ's and β's, the beam currents must be $I_+ = 2.6\,\mathrm{A}$ and $I_- = 1.1\,\mathrm{A}$. Since one bunch can contain order of 10^{10} electrons or positrons, the charge per bunch can be about 10^{-8} to 10^{-9} Coulomb. We will circulate 5,000 bunches that cross in each 2 ns to achieve the target beam current.

Ring	LER	HER	unit
Particles	e^+	e^-	
Energy (E)	3.5	8.0	GeV
Circumference (C)	3016.26		m
Luminosity (L)	1×10^{34}		$\mathrm{cm}^{-2}\,\mathrm{s}^{-1}$
Crossing angle (θ_x)	± 11		mrad
Tune shifts (ξ_x/ξ_y)	0.039/0.052		
Beta function at IP (β_x^*/β_y^*)	0.33/0.01		m
Beam current (I)	2.6	1.1	A
Natural bunch length (σ_z)	0.4		cm
Energy spread (σ_E/E)	7.1×10^{-4}	6.7×10^{-4}	
Bunch spacing (s_B)	0.59		m
Particles/bunch	3.3×10^{10}	1.4×10^{10}	
Emittance ($\varepsilon_x/\varepsilon_y$)	$1.8 \times 10^{-8}/3.6 \times 10^{-10}$		m
Synchrotron tune (ν_s)	$0.01 \sim 0.02$		
Betatron tune (ν_x/ν_y)	45.52/45.08	47.52/43.08	
Momentum compaction factor (α_p)	$1 \times 10^{-4} \sim 2 \times 10^{-4}$		
Energy loss/turn (U_0)	$0.81^\dagger/1.5^\ddagger$	4.8	MeV
RF voltage (V_c)	$5 \sim 10$	$10 \sim 20$	MV
RF frequency (f_{RF})	508.887		MHz
Harmonic number (h)	5120		
Longitudinal damping time (τ_ε)	$43^\dagger/23^\ddagger$	23	ms
Total beam power (P_b)	$2.7^\dagger/4.5^\ddagger$	4.0	MW
Radiation power (P_{SR})	$2.1^\dagger/4.0^\ddagger$	3.8	MW
HOM power (P_{HOM})	0.57	0.15	MW
Bending radius (ρ)	16.3	104.5	m
Length of bending magnet (L_b)	0.915	5.86	m

Table 2.3: Design parameters of KEKB (†: without wigglers, ‡: with wigglers)

2.3 Belle Detector

The Belle detector is illustrated in Figure 2.4 and 2.5. The Belle detector makes precise measurements of charged and neutral particles over a large fraction of the total center-of-mass solid angle. The detector components dedicated for this analysis are a silicon vertex detector (SVD)[19], a central drift chamber (CDC)[20], an array of 1188 aerogel Čerenkov counters (ACC)[21], 128 time-of-flight (TOF) scintillation counters[22], and an electromagnetic calorimeter containing 8736 CsI(Tl) crystals (ECL)[23], all located inside the 3.4-m-diameter superconducting solenoid that generates a 1.5 T magnetic field. In addition, although they are not used for this analysis, an iron return yoke outside the solenoid is segmented into 14 layers of 4.7-cm-thick iron plates alternating with a system of resistive plate counters that is used to identify muons and K_L^0 mesons (KLM)[24], and an extreame forward calorimeter (EFC) containing 160 BGO ($Bi_4Ge_3O_{12}$) crystals in each end is placed around the beam line.

The parameters and performance of these sub-detectors are summarized in Table 2.4. Brief descriptions of the sub-detectors are given in the following subsections. Consult also to the reference [25] for any details.

Note that the coordinate system used in this dissertation is defined as follows (x,y, and z form a right-handed orthogonal coordinate system).

x	horizontal, inward to the KEKB ring.
y	vertical, upward.
z	opposite of the positron beam direction.
r	$\sqrt{x^2+y^2}$
θ	the polar angle regarding to z axis.
ϕ	the azimuthal angle around z axis.

The low energy beam (e^+) line is aligned with the axis of the solenoid field (z) since the lower-momentum beam particles would suffer more bending in the solenoid field if they were off-axis.

2.3.1 Silicon Vertex Detector (SVD)

In order to observe a mixing oriented and time dependent CP violation, we have to measure the flight length difference of the two B mesons. The SVD measures charged track points with $\sim 10\,\mu$m of position resolution, and a vertex point of charged tracks with a precision of $\sim 100\,\mu$m. The vertex measurement also provides us a suppression method of $B\bar{B}$ combinatorial background, since the two B mesons usually decay in different points.

The cross-sectional view of the SVD is given in Figure 2.6. The SVD is placed just around the beam pipe. The SVD comprises three layers of the $300\,\mu$m thick double sided silicon detector (DSSD) ladders, each consists of 8, 10 and 14 ladders from the inner to the outer layer. Each DSSD has orthogonal strips in each sides and provides two orthogonal measurements along ϕ and z directions.

The momentum and angular dependence of the impact parameter resolution for real data

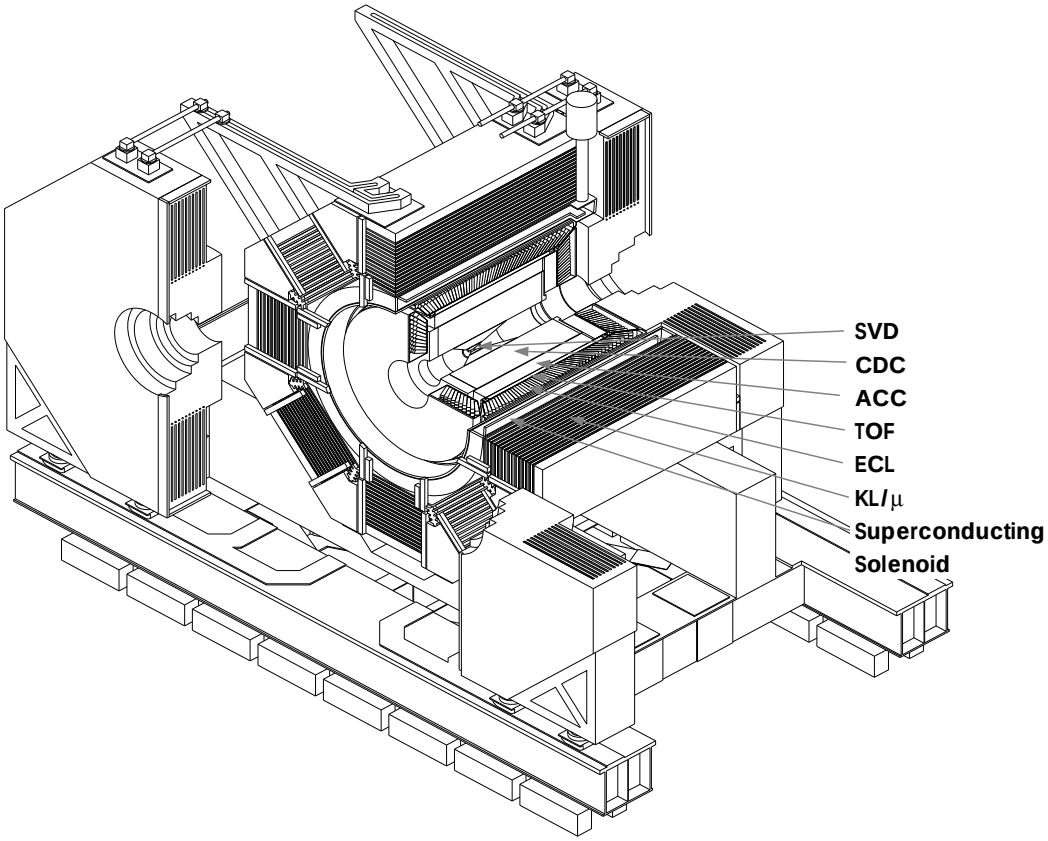

Figure 2.4: Belle detector

Detector	Type	Configuration	Readout	Design Performance
SVD	Double sided Si strip	$300\,\mu$m thick, 3 layers $r = 3.0 \sim 5.8\,$cm Length $= 22 \sim 34\,$cm	ϕ : 41 k θ : 41 k	$\sigma_{\Delta z} \sim 105\,\mu$m
CDC	Small cell drift chamber	Anode : 50 layers Cathode : 3 layers $r = 7.7 \sim 88\,$cm $-77 \leq z \leq 160\,$cm	A : 8.4 k C : 1.8 k	$\sigma_{r\phi} = 130\,\mu$m $\sigma_z = 200 \sim 1400\,\mu$m $\sigma_{p_t}/p_t = 0.3\%\sqrt{p_t^2+1}$ $\sigma_{\mathrm{d}E/\mathrm{d}x} = 6\%$
ACC	$n = 1.01 \sim 1.03$ Silica Aerogel	$\sim 12 \times 12 \times 12\,$cm^3 blocks 960 barrel / 228 endcap FMPMT readout	1788	$\mu_{eff} \geq 6$ $K/\pi : 1.2 \leq p \leq 3.5\,$GeV/$c$
TOF	Plastic Scintillator	128 ϕ segmentation $r = 120\,$cm Length $= 3\,$m	128×2	$\sigma_t = 100\,$ps $K/\pi : p \leq 1.2\,$GeV/c
TSC		64 ϕ segmentation	64	
ECL	CsI(Tl)	$\sim 5.5 \times 5.5 \times 30\,$cm^3 crystals Barrel : $r = 125 \sim 162\,$cm Endcap : $z = -102$ and $+196\,$cm	B : 6624 FE : 1152 BE : 960	$\sigma_E/E = 0.066\%/E$ $\oplus\ 0.81\%/E^{1/4} \oplus 1.34\%$ $\sigma_{pos} = 0.5\,\mathrm{cm}/\sqrt{E}$
KLM	Resistive plate counter	14 layers (5 cm Fe + 4 cm gap) 2 RPCs in each gap θ and ϕ strips	θ : 16 k ϕ : 16 k	$\Delta\phi = \Delta\theta = 30\,$mrad for K_L $\sigma_t = 1\,$ns 1% hadron fakes for μ
EFC	BGO	$2 \times 1.5 \times 12\,$cm^3	θ : 5 ϕ : 32	$\sigma_E/E = (0.3 \sim 1)\%/\sqrt{E}$
Beam pipe	Be double-wall	Cylindrical, $r = 2.3\,$cm 0.5 mm Be / 2 mm He / 0.5 mm Be		
Magnet	Superconducting	Inner radius $= 170\,$cm		$B = 1.5\,$T

Table 2.4: Performance parameters of the Belle detector (p and p_t in GeV/c, E in GeV)

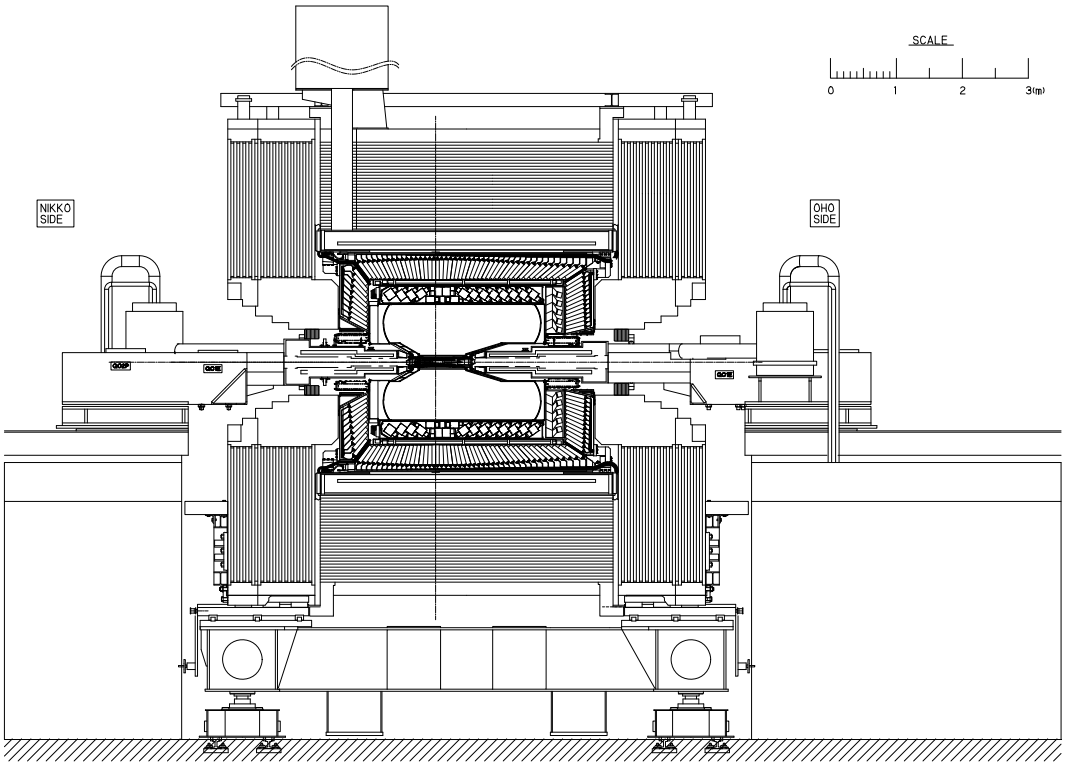

Figure 2.5: Side view of the Belle detector

is well represented by the following formula:

$$\sigma_{xy} = 19 \oplus 50/(p\beta \sin^{3/2}\theta)\,\mu\mathrm{m} \quad (2.7)$$

$$\sigma_{z} = 36 \oplus 42/(p\beta \sin^{5/2}\theta)\,\mu\mathrm{m} \quad (2.8)$$

More details are available in the reference [19].

2.3.2 Central Drift Chamber (CDC)

The role of the CDC is to measure the track position, momentum and specific ionization ($\mathrm{d}E/\mathrm{d}x$) of charged particles. The $\mathrm{d}E/\mathrm{d}x$ information is used for the particle identification (PID), combined with other particle identification detectors (ACC/TOF). In addition, another indispensable role of the CDC is to provide an online hardware trigger (Level 1 trigger). So far, only the CDC can provide a trigger for particles which come from near the IP. More descriptions on Level 1 trigger will be given in section 2.4.1.

The CDC is a small-cell drift chamber containing 50 anode layers (32 axial and 18 stereo wire layers) and 3 cathode strip layers. The anode layers are grouped into 11 superlayers (6 axial and 5 stereo superlayers). Combining axial and stereo hit information, 3-dimensional track reconstruction becomes possible. The cathode layers are located at the inner most part of the CDC, which measure the z position of a charged track. The number of readout channels is 8,400 for anodes and 1,792 for cathodes in total.

Figure 2.7 shows the geometrical configuration of the CDC. The CDC covers the region of 77 mm to 880 mm in radius and 17° to 150° in polar angle.

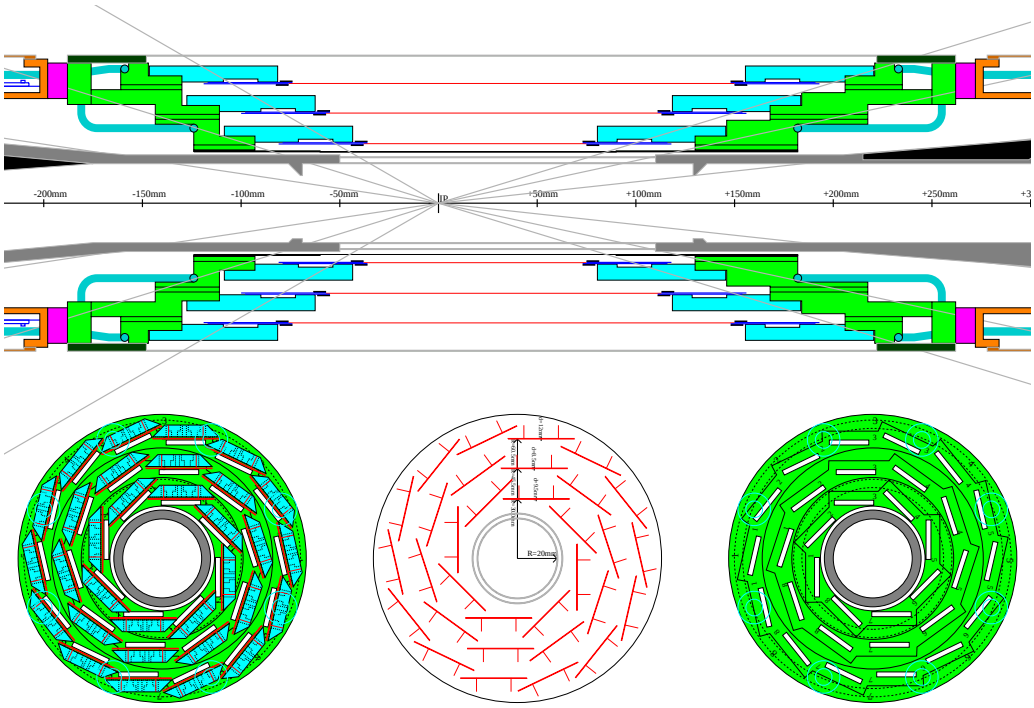

Figure 2.6: Silicon vertex detector

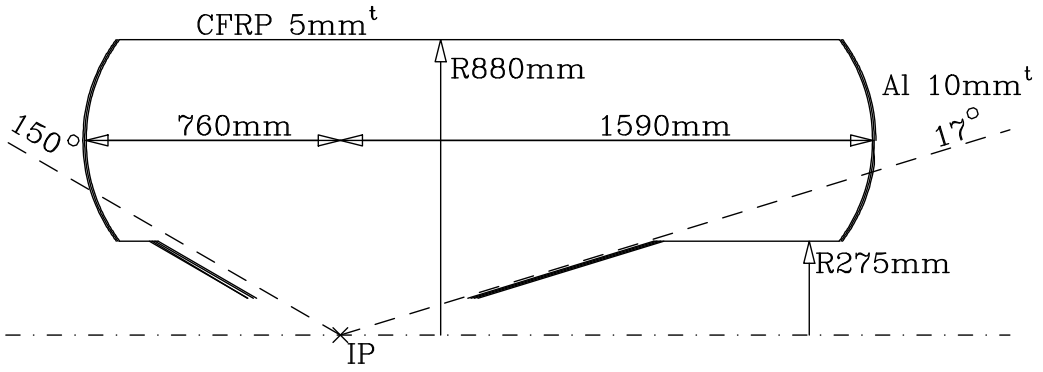

Figure 2.7: Central drift chamber

Low Z-gas (50% He and 50% C_2H_6) whose radiation length is ~ 640 m is used to reduce multiple scattering of a charged particle [26]. In spite of low Z gas, a good dE/dx resolution is obtained owing to a large content of ethane [27].

The spatial resolution is 130 μm in $r-\phi$ plane and less than 2 mm in z, which leads the transverse momentum resolution σ_{p_t}/p_t of $\sqrt{(0.19p_t)^2+0.34^2}\%$ where p_t is the transverse momentum in GeV/c. The dE/dx resolution is 6.9% for minimum ionizing particles.

2.3.3 Aerogel Čerenkov Counter (ACC)

The ACC is an array of threshold type silica aerogel Čerenkov counters. The ACC provides an information to separate charged kaons from charged pions in high momentum range (1.2 GeV/c $< p <$ 3.5 GeV/c), which extend the reach of TOF.

The ACC consists of the barrel and the endcap part. The configuration is shown in Figures 2.8 and 2.9.

The barrel ACC consists of 960 aerogel counters that are segmented into 16 division in z and 60 in ϕ. Five different refractive indices ($n = 1.01, 1.013, 1.015, 1.020, 1.028$) are used depending on the polar angle of the aerogel counter (See, Figure 2.8). The Čerenkov light from each barrel counter is fed into one or two fine-mesh photomultiplier(s) (FM-PMT) through air lightguides. The number of readout channels for the barrel ACC is 1,560 in total. The FM-PMT's can work in the 1.5 T magnetic field.

The endcap ACC is placed only in the forward side. It consists of 228 counters with $n = 1.03$. The counters are mounted in five concentric rings with different radii; each ring contains 36, 36, 48, 48 and 60 counters from inner to outer. Each endcap counter has one FM-PMT for readout and therefore the number of readout channels is 228.

2.3.4 Time of Flight counter (TOF)

The TOF is used to distinguish charged kaons from charged pions in the low momentum region. For a 1.2 m flight path, the TOF system with 100 ps time resolution is effective for particle momenta upto 1.2 GeV/c. The Trigger Scintillation Counter (TSC) together with the TOF generates the primary timing signal for the Level 1 trigger (See, section 2.4.1).

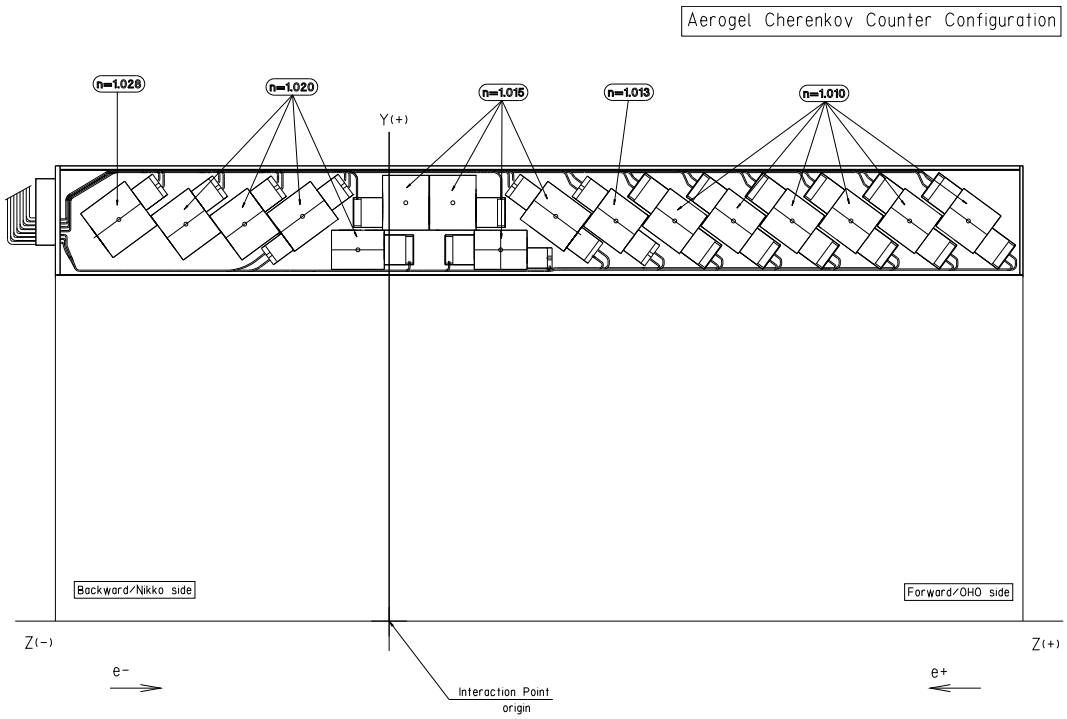

Figure 2.8: Barrel aerogel Čerenkov counter

The configuration of TOF/TSC is shown in Figure 2.10. The TOF system consists of 128 TOF counters and 64 TSC counters. Two trapezoidally shaped TOF counters (4 cm thick) and one TSC counter (0.5 cm thick) form one module. In total 64 TOF/TSC modules are placed at $r = 1.2$ m and cover $34^\circ < \theta < 120^\circ$. TOF is read out by FM-PMT's from both ends, while TSC is read out by single FM-PMT from the backward end. The total number of readout channels for TOF system is 320.

2.3.5 Electromagnetic Calorimeter (ECL)

The ECL measures the scintillation light from the electromagnetic shower generated in the crystals by charged and neutral particles, and determines the energy deposit of the particle. Photons and electrons deposit most of their energy in the crystals. We can thus measure the energy and momentum of the photon with a given origin of the photon (the IP, for example). The ECL provides various triggers; energy, number of isolated clusters, cosmic ray, and Bhabha event trigger. It also provides the secondary timing signal for the Level 1 trigger (See, section 2.4.1).

Figure 2.11 shows the overall configuration of the ECL. The ECL consists of total 8,736 CsI(Tℓ) crystals. The barrel part is placed at $r = 125$ cm and covers the polar angle region of 32.2° to 128.7°[4]. It is segmented into 46 in θ and 144 in ϕ and filled with 6,624 crystals. The forward endcap is placed at $z = +196$ cm and covers $12.01^\circ < \theta < 31.36^\circ$. It is segmented into 13 in θ and 48 to 144 in ϕ and filled with 1,152 crystals. The backward endcap is placed

[4]In the analysis we took $33^\circ$to 132°as the barrel ECL, which is not a big matter.

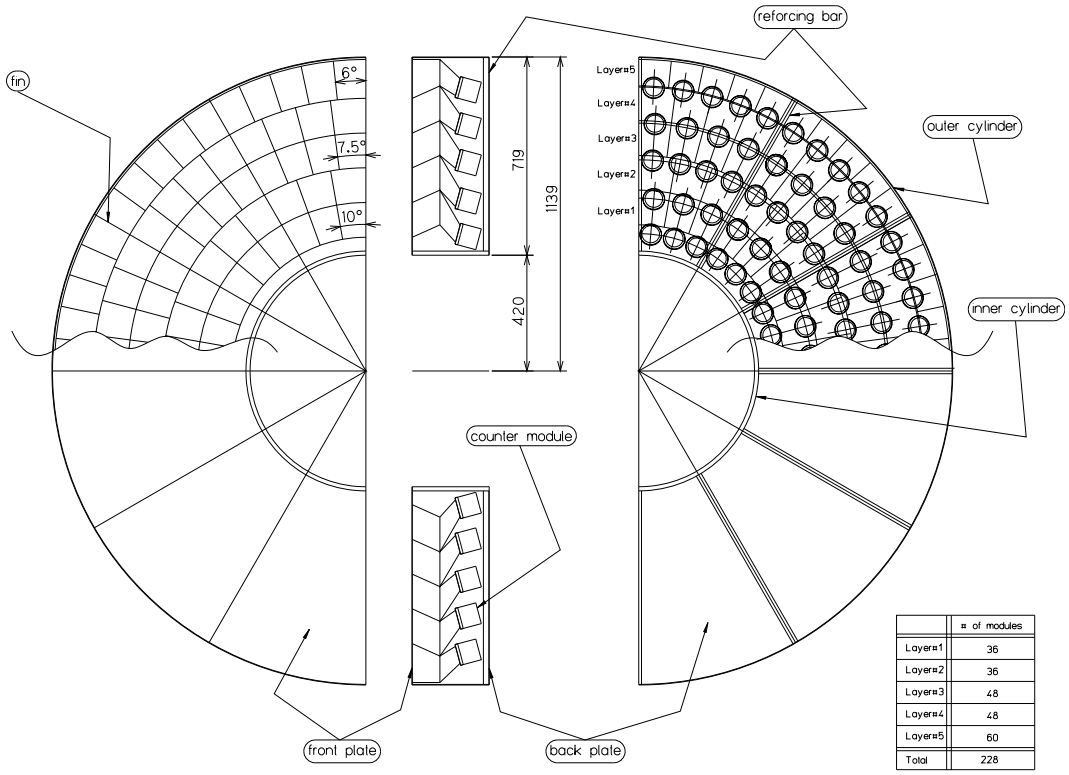

Figure 2.9: Endcap aerogel Čerenkov counter

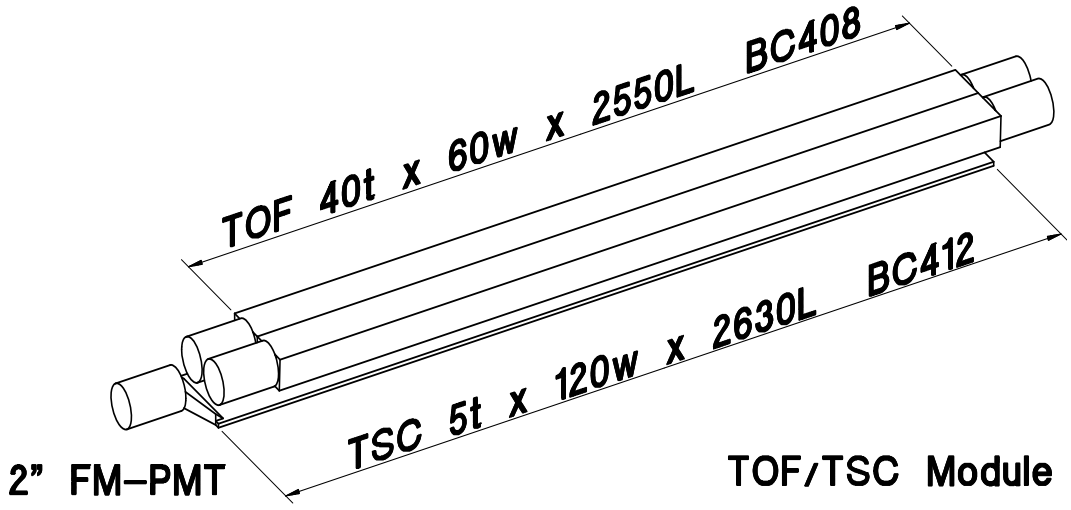

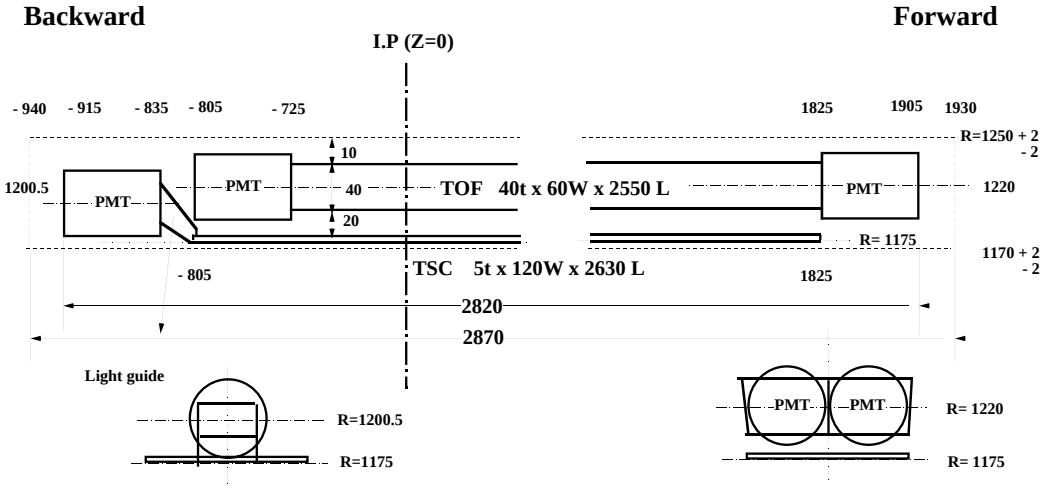

Figure 2.10: Time of flight and trigger scintillator counters

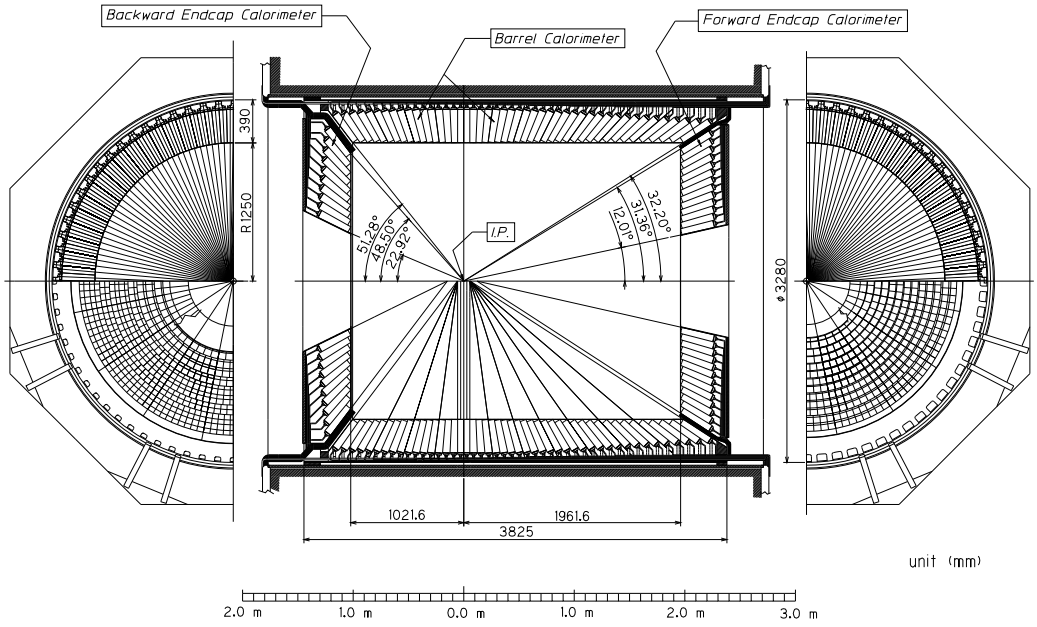

Figure 2.11: Electromagnetic calorimeter

at $z = -102\,\mathrm{cm}$ and covers $131.5° < \theta < 155.03°$. It is segmented into 10 in θ and 64 to 144 in ϕ, and filled with 960 crystals.

There are 29, 36 and 30 different types of crystal shape for barrel, forward endcap and backward endcap, respectively. The typical crystal for the barrel ECL is with about 5 kg weight, a trapezoid cross section with 5.5 cm sides in the front face and 6.5 cm in the back face, and 30 cm depth that correspond to 16 radiation length (X_0). Each crystal is read out by two 2 cm $\times$ 1 cm photodiodes.

Total amount of material in front of the CsI is, for example, $0.387X_0$ at $\theta = 90°$ [28]. The energy resolution measured by a photon beam test with the threshold energy of 0.5 MeV and with the 5×5 crystal matrix is $\sigma_E/E = 0.066\%/E \oplus 0.81\%/E^{1/4} \oplus 1.34\%$ and the position resolution is $\sigma_{pos} = 0.5\,\mathrm{cm}/\sqrt{E}$, with E in GeV [23].

2.3.6 K_L/μ Detector (KLM)

The KLM detector was designed to identify K_L's and muons with high efficiency over a broad momentum range above 600 MeV/c. The barrel part covers $45° < \theta < 125°$ and the forward (backward) endcap extend this to 20° (155°)

The KLM consists of alternating layers of glass-electrode resistive plate counters (RPCs) and 4.7cm-thick iron plates. There are 15 RPC and 14 iron layers in the octagonal barrel region and 14 RPC/iron layers in each of the endcaps.

The configuration of RPC is shown in Figure 2.12 and 2.13. RPC has two parallel plate electrodes with high bulk resistivity ($\geq 10^{10}\,\Omega$cm) separated by a gas-filled gap. We chose the gas mixture to be 62% HFC-134a, 30% argon, and 8% butane-silver. In the streamer mode, an ionizing particle traversing the gap initiates a streamer in the gas that results in a local discharge of the plates. This discharge is limited by the high resistivity of the plates and the quenching characteristics of the gas. The discharge induces a signal on external pickup strips

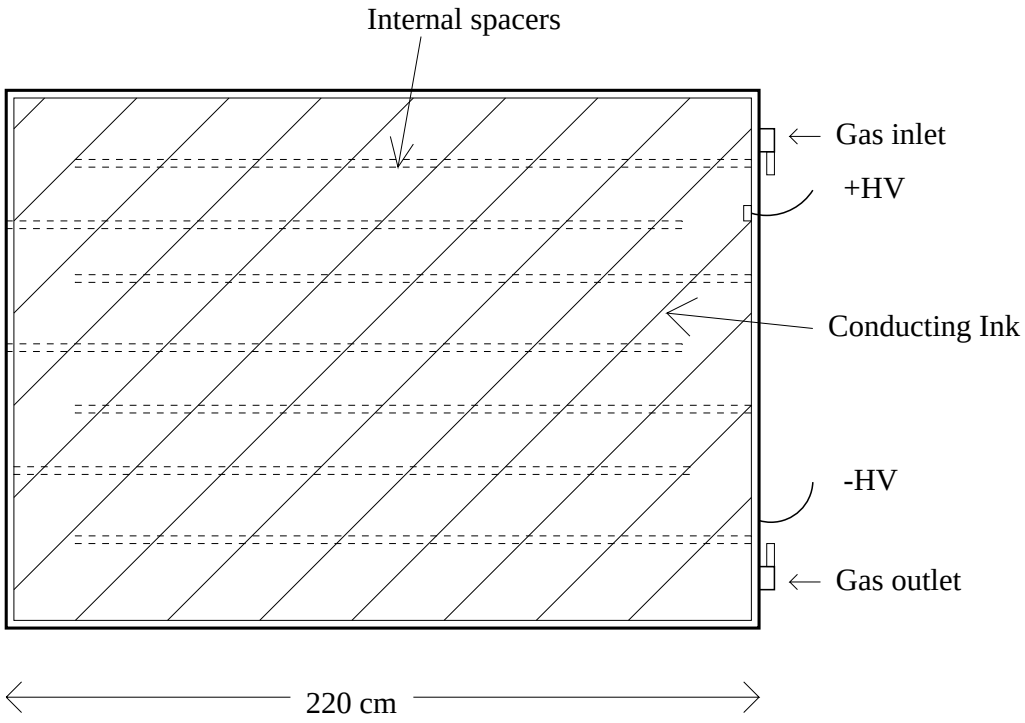

Figure 2.12: Barrel RPC

along z or ϕ directions.

The iron plates provide a total 3.9 interaction length of material for a particle traveling normal to the detector planes. In addition, ECL provides another 0.8 interaction length of material. A muon can be identified from the number of the iron layers penetrated. A K_L that interacts in the iron or ECL produces a shower of ionizing particles. The location of the shower determines the direction of the K_L.

More details can be found in the reference [24].

2.3.7 Extreme Forward Calorimeter (EFC)

The EFC measures the energy of photons and electrons at the extreme forward (backward) direction out of the ECL acceptance. The EFC covers $6.4^\circ < \theta < 11.5^\circ$ in the forward direction and $163.3^\circ < \theta < 171.2^\circ$ in the backward direction. The EFC detector is attached to the front faces of the cryostats of the compensation solenoid magnets of the KEKB storage ring, surrounding the beam pipe as shown in 2.14.

We use BGO ($Bi_4Ge_3O_{12}$) crystals, because the EFC is exposed in the high irradiation (about 5 MRad per year) of photons from the synchrotron radiation and the spent electrons. Both forward and backward EFC consists of BGO crystals divided into 5 segments in θ and 32 in ϕ, respectively. Typical cross-section of a crystal is about $2\,\mathrm{cm} \times 2\,\mathrm{cm}$, with $12X_0$ for forward and $10.5X_0$ for backward in the radiation length.

More details of EFC is described in [28].

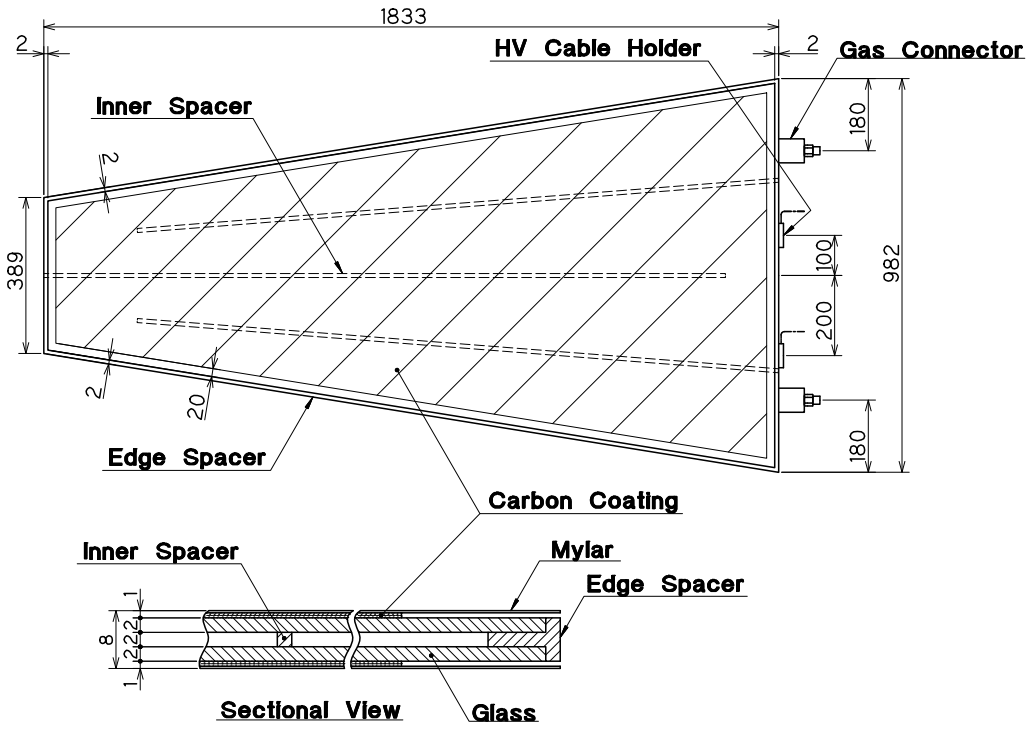

Figure 2.13: Endcap RPC

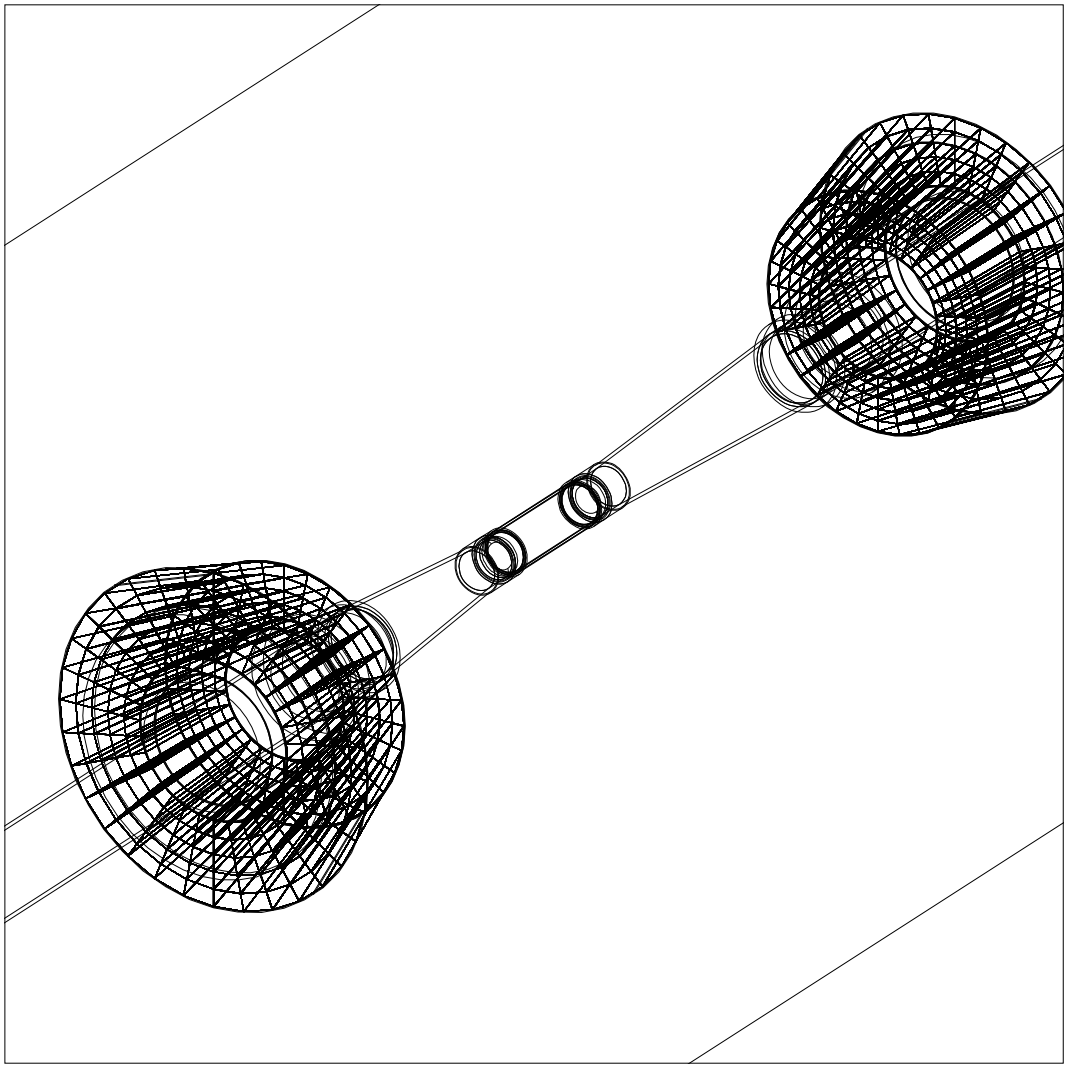

Figure 2.14: Extreme forward calorimeter

2.4 Trigger, Data Acquisition and Data Processing

In this section, the trigger system, the data acquisition system and off-line processing of the stored data are described. Although these issues are closely related to the detector, because of their impact on our data, namely, they can kill or bias the data before they are delivered to us for analysis, we will discuss about them in a separate section.

The trigger and data acquisition system is designed and has achieved to operate with the following conditions.

- typical trigger rate is 200 Hz
- maximum trigger rate is 500 Hz
- data size is 30 kB/event
- data transfer speed is 15 MB/s

2.4.1 Level 1 Trigger

In order to record the data of the physics events of our interest, we have to provide the common stop signal for TDC's and the gate signal for ADC's, which we call the Level 1 trigger. Our target is to achieve $\simeq 100\%$ trigger efficiency for $B\bar{B}$ events. To obtain such high efficiency, we have redundant triggers which are generally categorized into two independent triggers, namely the track trigger and the energy trigger. Since the DAQ deadtime, which increase linearly to the trigger rate, directly means the deficiency for $B\bar{B}$ events, the Level 1 trigger must have a power to suppress background to a tolerable level. In addition, in order to accommodate to the daily increase of the beam current and the beam background, the Level 1 trigger must have sufficient flexibility; the trigger rate should be reducible without causing a significant deficiency for $B\bar{B}$ events when the background rate is high.

Figure 2.15 shows the schematic view of the Level 1 trigger system. It consists of the sub-detector trigger systems and the central trigger system called the Global Decision Logic (GDL) [29]. The sub-detector triggers are combined at GDL. We form two independent and redundant triggers; the track trigger and the energy trigger. The track trigger is based on the CDC $r-\phi$ and z trigger, the TOF trigger and the number of isolated ECL cluster trigger. The energy trigger is based on the ECL energy sum trigger. The baseline trigger for hadronic events is a logical OR of the following triggers.

- tight 2 track trigger
- loose 3 track trigger
- number of isolated clusters ≥ 4
- energy sum > 1 GeV

The exact definitions and conditions of triggers activated during the runs are summarized in the Belle notes[30]. The efficiency of track (energy) trigger for hadronic events can be checked with the data subset for which we require the energy (track) trigger was fired. Since the efficiency of each trigger is greater than 97%, our trigger efficiency as an OR of these two is greater than 99.9%. Typical trigger rate was 200 Hz, with which the DAQ deadtime is about 4%.

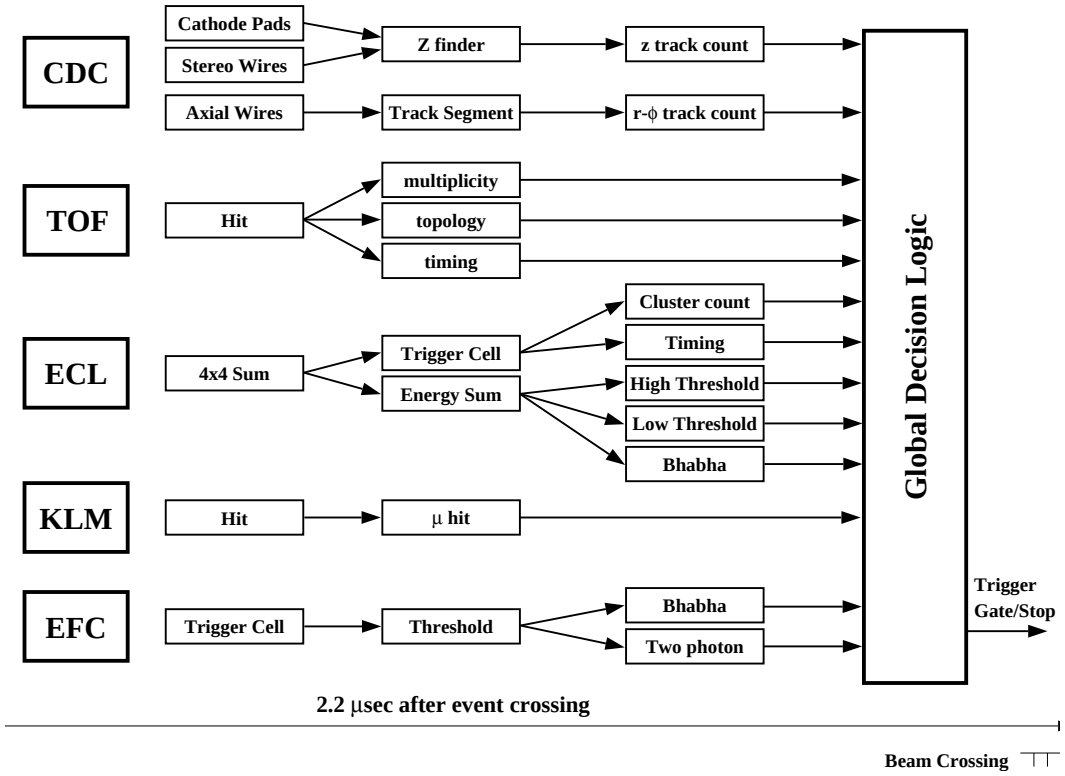

Figure 2.15: Belle trigger system

Another specially important issue of the Level 1 trigger for the Belle experiment is the trigger timing. As discussed in 2.2 our target beam bunch crossing rate is 500 MHz, and therefore we cannot use the bunch crossing timing for the event timing at the online level. The level 1 trigger must decide the online event timing not from a given accelerator signal but from the detector responce (trigger itself). The final trigger timing is decided from timing signals from the TOF and the ECL trigger systems. The TOF timing signal has less jitter than the ECL, but since the TOF does not cover the endcap region and is not sensitive to neutral particles, the ECL timing signal is used as a back-up [5]. Both the TOF and ECL timing signals are adjusted to 1.85 μs from the event crossing. If TOF timing signal is available, GDL asserts the final trigger at 350 ns after the TOF timing signal. If TOF is not available but ECL is available, GDL asserts the final trigger at 350 ns after the ECL timing signal. If either is not available, GDL determines the trigger timing itself from other trigger signals. In either case, the final trigger timing from GDL is adjusted to 2.2 μs from the event crossing. The jitter of the final trigger timing is order of 10 ns when the TOF timing singal was available, and 100 ns when only the ECL timing signal was available, which are precise enough for the online use.

[5] The rate of timing signal must be below 70 kHz in order to keep the fake timing probability due to a random coincidence in $\sim$ 300 ns window below 1%. The single hit rate on TOF exceeds 70 kHz and we have to require multiple hits on TOF for the timing signal; this is another reason that we need a back-up timing signal.

2.4.2 Data Acquisition (DAQ)

In order to achieve the data acquisition with a deadtime fraction less than 10% upto 500 Hz of trigger rate, a distributed-parallel DAQ system has been devised. A schematic view of the Belle data acquisition system is shown in Figure 2.16. The subsystems for readout from sub-detectors and also from the trigger systems run in parallel. We adopted a charge-to-time (Q-to-T) and time-to-digital-converter (TDC) technique to read out signals from most of the detectors. The data from each subsystem are combined into a single event record by the event builder, which converts the "detector-by-detector" parallel data streams to "event-by-event" data river. The event builder output is transfered to the online computer farm, where another level of event filtering (Level 3 software filter[6]) is possible after a fast event reconstruction. Here we monitor the quality of data and display the reconstructed event to check if the DAQ is going fine. Finally, the data are sent via optical fibers to the mass storage system located at the computer center of KEK which is 2 km appart from the Belle detector, and stored in tapes for off-line use.

A typical data size for a hadronic event is measured to be about 30 kB, therefore the maximum data transfer speed is required to be 15 MB/s to operate in 500 Hz.

2.4.3 Level 4 Software Filter

The purpose of the Level 4 software filtering is to reject background events just before the full event reconstruction in the very beginning of the DST (Data Summary Table[7]) production chain. High efficiencies are required not only for $B\bar{B}$ events, but also for $q\bar{q}$ $\gamma\gamma$, τ-pair, di-muon, and so on. Since this is done before the full reconstruction, a fast reconstruction software named `fzisan` [31] is used instead of the full reconstruction software.

The selection criteria of the Level 4 software filter is as follows.

- Selection by the Level 1 trigger information :
  Events with some specific trigger bits are saved for detector studies without any further processing.

- Energy measured by ECL :
  We require the ECL energy reconstructed by `fzisan` to be greater than 4 GeV. Concurrently a veto logic using the Level 1 information is applied against cosmic ray events.

- Selection of events with a track coming from the IP :
  By reconstructing charged tracks by `fzisan`, events are selected if at least one track with the transverse momeutum greater than 300 MeV/c is originating from the IP ($|dr| <$ 1.0 cm, $|dz| <$ 4.0 cm).

- Level 4 monitoring :
  For monitoring of the preformance of the Level 4 software filter, 1% of events which fail above selection criteria are saved.

The efficiency for high purity hadronic event real data sample is very close to 100%. The efficiency for some decay modes are checked with Monte Carlo (MC). For example, even for

[6] The Level 3 software filter has activated since the year 2001; has been deactivated for the data set of this thesis.

[7] Historically, this stood for Data Summary Tape.

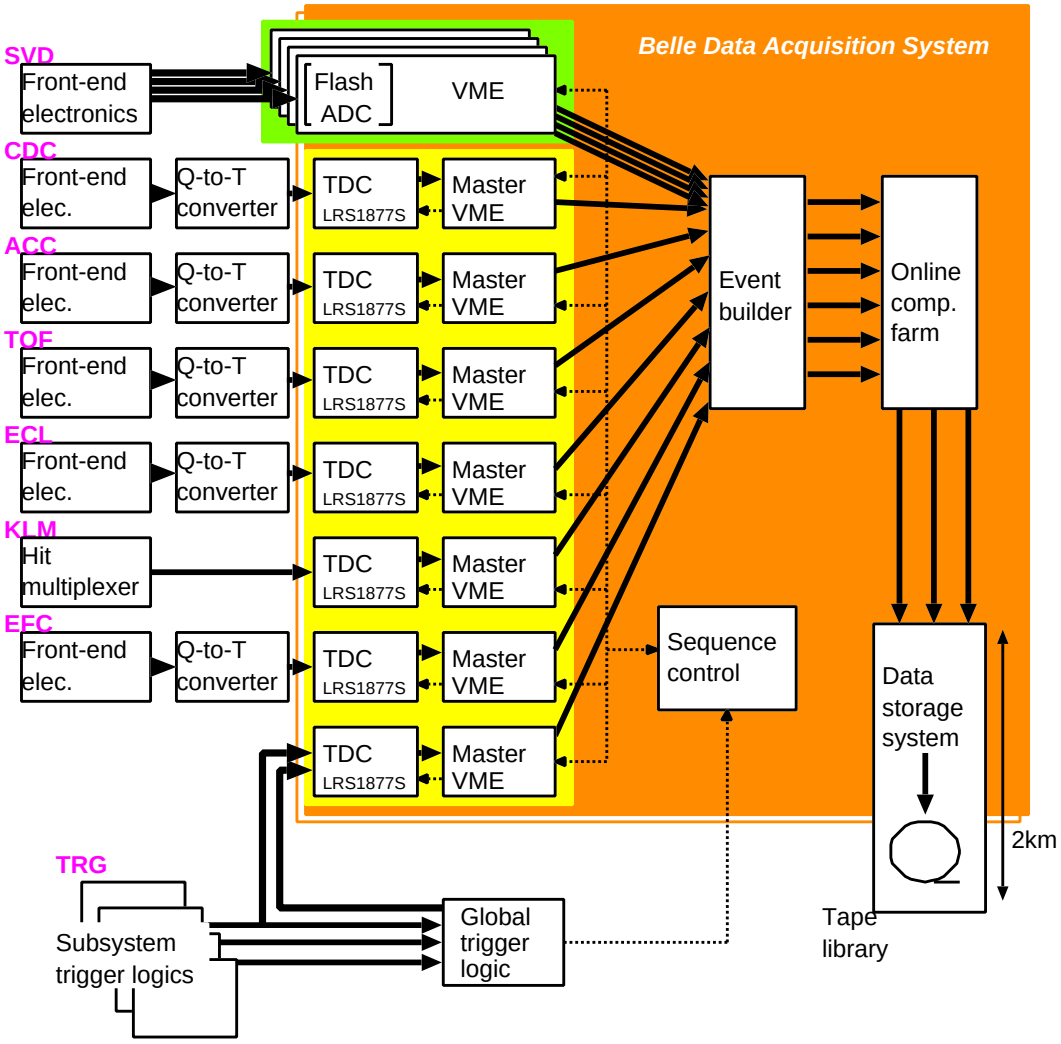

Figure 2.16: Belle DAQ system – data flow is shown in bold solid arrows, control flow is shown in broken arrows.

$B \to K_S \pi^0$ (The other B decays generically), the efficiency is 100%. On the other hand, the reduction factor of the whole Level 1 triggered events is about 1/4.

2.4.4 DST Production and Event Classification

The events accepted by the Level 4 software filter are reconstructed and the information is stored as DST. In this stage, the rawdata – the direct logs from data acquisition devices – are converted into physics objects of 4-vectors and so on.

At the most downstream of the reconstruction flow, events are examined if they satisfy certain selection criteria, and recorded as the skimmed data accordingly. The skim categories are for example as follows.

- `HadronA` : general hadronic events (loosest)
- `HadronB` : general hadronic events (standard)
- `HadronC` : general hadronic events (tightest)
- `HadronJ` : J/Ψ inclusive events
- `Bhabha` : $e^+e^- \to e^+e^-$ events
- `RadBhabha` : $e^+e^- \to e^+e^-\gamma$ events
- `GammaPair` : $e^+e^- \to \gamma\gamma$ events
- `CalQED` : QED events
- `MuPair` : $e^+e^- \to \mu^+\mu^-$ events
- `RadMuPair` : $e^+e^- \to \mu^+\mu^-\gamma$ events
- `TauPair` : $e^+e^- \to \tau^+\tau^-$ events
- `LowMult` : two photon, $e^+e^- \to e^+e^-e^+e^-$, etc.
- `BeamBG` : beam induced background events
- `GammaPhi` : $\gamma\phi$ events for KLM calibration
- `EFCBhabha` : Bhabha events with EFC hits
- `Cosmic` : Cosmic ray events
- `Random` : Random triggered events

In this thesis, we use `HadronB` skim for the main analysis and `RadBhabha` skim for photon finding systematics study.

Also at the same stage, we monitor the quality of reconstructed data by checking basic observables like the number of reconstructed tracks, the total visible energy, the hadronic cross-section, etc.

The calibration constants, which are used to correct detector responce, are kept in `PostgreSQL` [32] database in our system. After checking skimmed data created by DST

production job, the detector constants are improved on the weekly basis to correct for environmental effects.

A typical processing speed of DST production is around 40 Hz, depending on beam conditions. Using three CPU servers out of seven, we can process about $80\,\mathrm{pb}^{-1}$ per day, we can keep the DST production in track with DAQ with delay of normally one day.

Chapter 3

Reconstruction of $B \to X_s\gamma$ and Cuts

3.1 Overview

We start from the events that passed the general hadronic event selection criteria. We then select the events that contain a prominent hard photon in the event. We select the most energetic photon as the candidate of the primary photon of $B \to X_s\gamma$ decay. The recoil system (X_s) that carries the strangeness is semi-inclusively reconstructed from one kaon plus one to four pions. The contribution from modes which are not reconstructed by these combinations will be extrapolated at last.

We combine the photon and every X_s candidate to form a B meson. In order to kill an obvious wrong combination, we apply cuts on a candidate combination; we call these cuts "pre-selection". If there are still multiple candidates left, we select the best (most-B-like) candidate combination. We apply several cuts on the selected single candidate in order to suppress background events; we call these cuts "final cut".

In the following sections, first the general hadronic event extraction method from our raw data is described. We then discuss the reconstruction method step by step. The background events are then investigated and suppression methods for them are considered. The cuts are basically tuned so that it maximizes the figure of merit ($S/\sqrt{S+N}$), but some are moved around to control the systematic and theoretical uncertainty.

3.2 Hadronic event skim

We start from the general hadronic event skim `HadronB`. The skim criteria for `HadronB` is as follows.

- primary event vertex near IP : $|r| < 1.5\,\mathrm{cm}$, $|z| < 3.5\,\mathrm{cm}$
- number of "good" charged tracks : ≥ 3
  where "good" charged track is defined as : $p_t > 0.1\,\mathrm{GeV/c}$, $|dr| < 2.0\,\mathrm{cm}$, $|dz| < 4.0\,\mathrm{cm}$.
- total visible energy (in $\Upsilon(4S)$ rest frame) : $E_{vis} \geq 0.2\sqrt{s}$.
- momentum balance in z (in $\Upsilon(4S)$ rest frame) : $|\sum p_z| \leq 0.5\sqrt{s}$.

- ECL energy sum : $0.18 < E_{ECL}/\sqrt{s} < 0.8$.
- at least two ECL clusters in the barrel.
- Heavy jet mass : $M_{jet} > 0.25E_{vis}$ or $M_{jet} > 1.8\,\mathrm{GeV/c^2}$
  Jet masses are calculated in two hemispheres perpendicular to the event thrust axis. Jet mass will be about half of the visible energy for hadronic events, while it is below 2 GeV for τ and QED events.
- average cluster energy : $< 1\,\mathrm{GeV}$
  It is above 1 GeV for QED events, not for hadronic events.

The `HadronB` selection is 99% efficient for $B\bar{B}$ events, and 87% efficient for $q\bar{q}$ events, approximately.

3.2.1 Number of $B\bar{B}$

The number of $B\bar{B}$ pairs in the `HadronB` sample is estimated [33] by examining the 2nd Fox-Wolfram moment's ratio $R_2 = H_2/H_0$ distribution. R_2 is one of the famous event shape variable where for a spherical event topology ($B\bar{B}$) $R_2 \sim 0$ and for a jetty event topology ($q\bar{q}$) $R_2 \sim 1$. The definition of the Fox-Wolfram moments will be given in section 3.10.1 (equation 3.3).

On-resonance data consist of $B\bar{B}$ and $q\bar{q}$ events[1] in a ratio of about 1 to 3 as discussed in section 2.1. The R_2 distribution for $q\bar{q}$ can be determined from the off-resonance data. We can therefore determine the amounts of $q\bar{q}$ and $B\bar{B}$ contributions in the on-resonance data by fitting the R_2 distribution with that for $B\bar{B}$ MC and for the off-resonance data. Since we do not take the off-resonance data very often, the beam conditions during the on-resonance data taking and during the off-resonance data taking are somewhat different. This leads a systematic error in the number of $B\bar{B}$ determination. The fitted R_2 distribution is shown in Figure 3.1.

The dataset used for this analysis is listed in Table 3.1. It consists of $5.84\mathrm{fb}^{-1}$ taken on the $\Upsilon(4S)$ resonance and $0.59\mathrm{fb}^{-1}$ taken at 60 MeV below the resonance. The total number of $B\bar{B}$ pairs used for this analysis is 6.07×10^6.

3.2.2 Monte Carlo (MC) samples

For background study, we use 53×10^6 of generic $q\bar{q}$ and 18×10^6 of generic $B\bar{B}$ MC samples. They are large enough comparing to the real data size of this analysis given in Table 3.1. The generic $B\bar{B}$ samples are generated according to branching fractions listed in a table called `decay.dec`. It covers most of the known channels with branching fractions based on past measurements.

For signal events, the recoil intermediate state is taken as a mixture of the exclusive $K^*(892)$ resonance at the lowest end of the mass region and continuum X_s for the higher mass region which represents the higher K^* resonances ($K_1(1270)$, $K_1(1400)$, $K^*(1410)$, $K_2^*(1430)$, $K^*(1680)$, ...) and non-resonant components. Unlike the $K^*(892)$, higher resonances have broad mass widths and overlap each other, and form a continuum spectrum. The non-resonant

[1] Actually, there are small contributions from QED processes and beam background. By using the off-resonance data, these effects are also taken into account except for the run dependent contributions of the beam background. For detail, consult the reference [33].

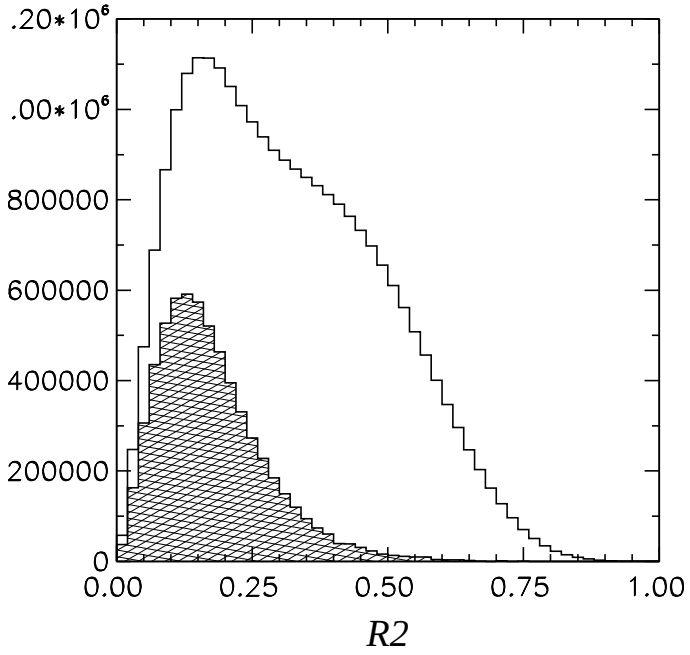

Figure 3.1: R2 distribution – $B\bar{B}$ distribution (Double Hatched) is extracted from the distribution for HadronB (Solid Line).

On resonance data

exp	run	library version	luminosity	$N_{B\bar{B}}$
7	6–243	b20000430_1200	245.5 pb^{-1}	$230017 \pm 1131\ ^{+2990.2}_{-2300}$
7	244–454	b20000430_1200	262.9 pb^{-1}	$220213 \pm 1169\ ^{+2862.8}_{-2202}$
7	455–475	b20000430_1200	28.0 pb^{-1}	$23516 \pm 335\ ^{+305.7}_{-235}$
7	537–727	b20000430_1200	290.7 pb^{-1}	$281517 \pm 1261\ ^{+36597}_{-2815}$
7	729–827	b20000430_1200	179.8 pb^{-1}	$172210 \pm 939\ ^{+22387}_{-1722}$
7	858–982	b20000430_1200	239.1 pb^{-1}	$244857 \pm 1122\ ^{+20813}_{-2449}$
7	983–1138	b20000430_1200	353.5 pb^{-1}	$353718 \pm 1435\ ^{+30066}_{-3537}$
7	1141–1229	b20000430_1200	358.3 pb^{-1}	$334156 \pm 1439\ ^{+28403}_{-3342}$
7	1231–1248	b20000430_1200	80.9 pb^{-1}	$75086 \pm 594\ ^{+6382}_{-751}$
7	1257–1270	b20000430_1200	32.5 pb^{-1}	$31642 \pm 368\ ^{+2690}_{-316}$
7	1271–1320	b20000430_1200	136.9 pb^{-1}	$149941 \pm 812 \pm 1499$
7	1321–1413	b20000430_1200	362.3 pb^{-1}	$398673 \pm 1471 \pm 3987$
7	1414–1439	b20000430_1200	93.6 pb^{-1}	$103809 \pm 657 \pm 1038$
7	1441–1486	b20000517_1555	188.1 pb^{-1}	$206706 \pm 978 \pm 2067$
7	1538–1639	b20000517_1555	243.6 pb^{-1}	$267657 \pm 1143 \pm 2677$
7	1641–1746	b20000517_1555	234.4 pb^{-1}	$251821 \pm 1114 \pm 2518$
7	1752–1825	b20000517_1555	252.1 pb^{-1}	$283878 \pm 1171 \pm 2839$
7	1826–1897	b20000517_1555	250.4 pb^{-1}	$274602 \pm 1163 \pm 2746$
7	1913–1996	b20000607_2210	260.2 pb^{-1}	$281517 \pm 1189 \pm 2815$
7	1997–2059	b20000607_2210	210.7 pb^{-1}	$229728 \pm 1046 \pm 2297$
7	2063–2123	b20000607_2210	234.8 pb^{-1}	$247730 \pm 1113 \pm 2477$
7	2124–2156	b20000607_2210	135.3 pb^{-1}	$144704 \pm 805 \pm 1447$
7	2294–2430	b20000607_2210	289.8 pb^{-1}	$308694 \pm 1270 \pm 3087$
7	2432–2515	b20000607_2210	140.2 pb^{-1}	$149319 \pm 821 \pm 1493$
7	2516–2620	b20000607_2210	219.8 pb^{-1}	$234023 \pm 1070 \pm 2340$
7	2621–2665	b20000607_2210	117.9 pb^{-1}	$130692 \pm 747 \pm 1307$
7	2668–2796	b20000607_2210	226.3 pb^{-1}	$241434 \pm 1089 \pm 2414$
7	2798–2819	b20000607_2210	43.7 pb^{-1}	$49958 \pm 438 \pm 500$
7	2820–2834	b20000607_2210	42.8 pb^{-1}	$48156 \pm 433 \pm 482$
7	2840–2854	b20000607_2210	45.1 pb^{-1}	$48771 \pm 442 \pm 488$
7	2856–2865	b20000607_2210	42.7 pb^{-1}	$46464 \pm 430 \pm 465$
	total		5841.9 pb^{-1}	$6065211 \pm 10337\ ^{+154995}_{-121019}$

Off resonance data

exp	run	library version	luminosity	no. of events
7	1490–1536	b20000607_2210	120.5 pb^{-1}	370885
7	2163–2231	b20000607_2210	243.6 pb^{-1}	741832
7	2232–2293	b20000607_2210	225.7 pb^{-1}	694342
	total		589.8 pb^{-1}	1807059

Table 3.1: Analyzed data.

components are expected to be small. An exclusive $K\pi\gamma$ reconstruction analysis [34] supports this fact at least for the two-body components. The way to mix the exclusive $K^*(892)$ and the continuum X_s sample will be described in section 4.3.1.

3.3 Photon candidate selection

A prominent signature of $B \to X_s\gamma$ is a high energy primary photon in the final state. When a b quark at rest decays into an s quark and a photon, the photon energy will be monochromatic. It is smeared by a gluon emission, by the Fermi motion of the b quark in the B meson, and by a nonzero momentum of the B meson in the $\Upsilon(4S)$ rest frame. Of course, it is smeared by the reconstruction resolution, finally. According to theoretical predictions [35][38], the primary photon energy spectrum in the $\Upsilon(4S)$ rest frame peaks around 2.3 GeV.

A photon candidate is reconstructed from an ECL cluster of 5×5 crystals that does not match to any charged track, where charged tracks are reconstructed by the CDC and extrapolated to the ECL inner surface. Isolation for a photon in the barrel ECL from charged tracks is shown in Figure 3.2(a).

Since we will require that the primary photon and the recoil system form a B meson and cut tightly on the recoil mass later, cuts on the primary photon energy are redunant and ineffective to the final result. But these are useful in skimming the data and rejecting events in the very early stage of the analysis, thus greatly speeding up the processing time. We take the most energetic photon as the primary photon candidate if its energy in the $\Upsilon(4S)$ rest frame is between 1.8 and 3.4 GeV. The energy spectrum is shown in Figure 3.2(b).

The primary photon candidate is required to be inside the acceptance of the barrel ECL ($33^\circ < \theta_\gamma < 132^\circ$) in order avoid systematic uncertainty in the endcap region. A fake photon candidate due to the poor efficiency of charged tracking in the endcap region can be avoided by this. This cut also kills initial state radiation (ISR) $q\bar{q}\gamma$ background which has a large cross section at small angles. The θ_γ distribution is shown in Figure 3.2(c).

In order to kill photons comming from π^0 or η decay, we require the shower shape to be consistent to a single isolated electromagnetic shower; we require that more than 95% of the shower energy is inside the central 3×3 matrix, say E9/E25> 0.95. Also, we combine the primary photon candidate with another photon candidate and reject if the invariant mass is consistent with a π^0 or η. The veto criteria are as follows.

- $|M_{\gamma\gamma} - M_{\pi^0}| < 18$ MeV/c^{2}and $|\vec{p}_\gamma^{2nd}| > 20$ MeV/c
- $|M_{\gamma\gamma} - M_\eta| < 32$ MeV/c^{2}and $|\vec{p}_\gamma^{2nd}| > 200$ MeV/c

The energy cut for the second photon is calculated in the $\Upsilon(4S)$ rest frame, which is applied to avoid over-vetoing by fake combinations. The distributions for E9/E25 and $M_{\gamma\gamma}$ is shown in Figure 3.2(d) and (e).

3.4 Charged kaon($K^\pm$)/pion($\pi^\pm$) selection

Charged tracks are reconstructed by the CDC and the SVD. We calculate the momentum of a track from the curvature and extrapolate the track to obtain the momentum at the closest point to the coordinate origin in $x - y$ plane [2].

[2]This is better to be the run-dependent IP rather than the coordinate origin.

(a) Isolation

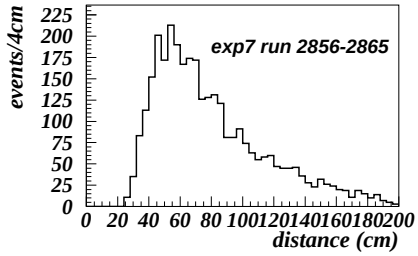

(b) Energy

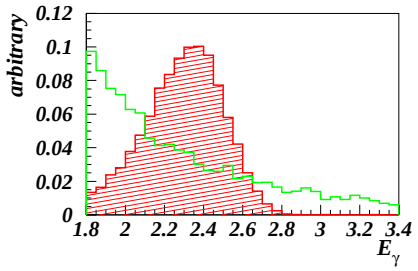

(c) Theta

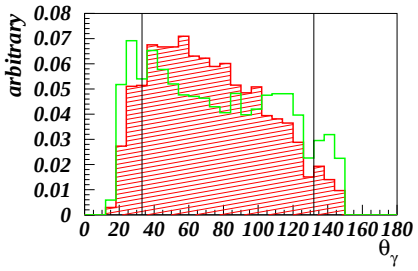

(d) E9/E25

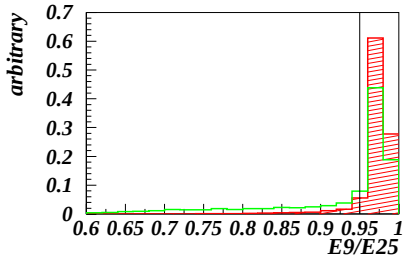

(e) $M_{\gamma\gamma}$

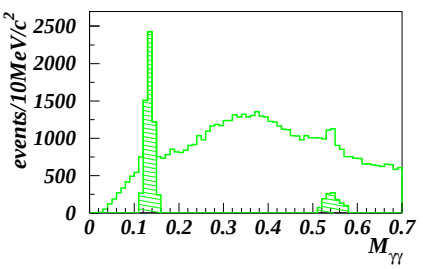

Figure 3.2: Variables for photon selection or selected photons – (a)Distance from a photon in barrel ECL to the nearest charged track.
Energy spectrum (b) for signal MC (hatched) and $q\bar{q}$ MC (open). The signal photon is semi-monochromatic due to quasi-two-body decay.
Polar angle distribution (c) for signal MC (hatched) and $q\bar{q}$ MC (open).
E9/E25 distribution (d) for signal MC (hatched) and $q\bar{q}$ MC (open).
$M_{\gamma\gamma}$ distribution (e) for $q\bar{q}$ MC. π^0 and η peaks are clearly seen. From all combinations (open), π^0 and η contributions are vetoed (hatched).

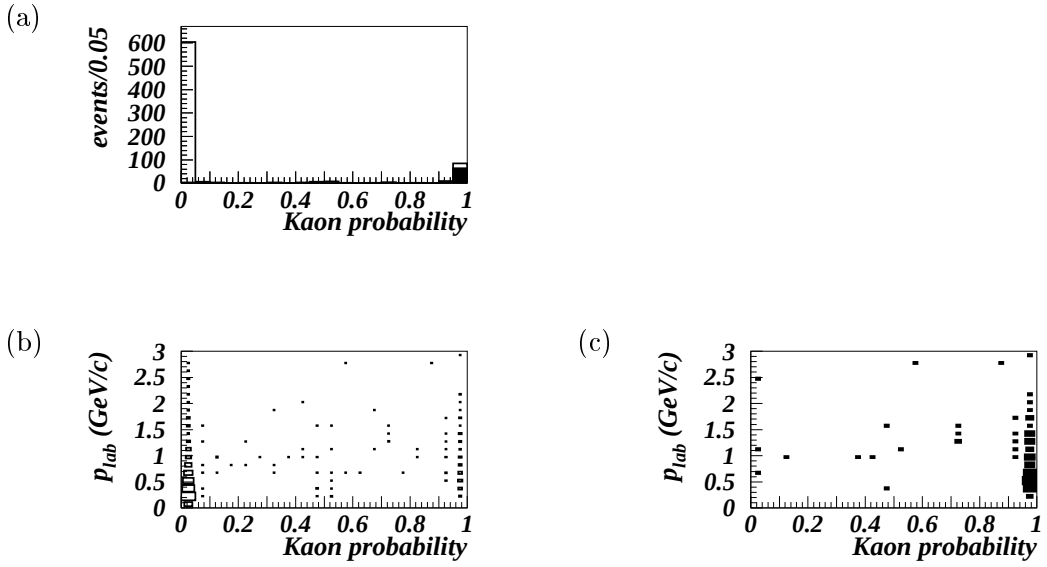

Figure 3.3: (a) Kaon probability of charged tracks in MC; for all tracks (open) and for MC tagged $K^{\pm}$ (solid).
Kaon probability vs momentum of charged tracks in MC for all tracks (b) and for MC tagged $K^{\pm}$ (c).

Particle identification is attempted in point that whether the particle is pion-like or kaon-like by utilizing all three PID devices. For every charged track, likelihood from ACC, TOF and CDC $\mathrm{d}E/\mathrm{d}x$ are calculated for pion and kaon hypotheses. A combined likelihood is constructed for each hypothesis in such a way that a pion-like track gives zero and a kaon-like track gives one.

Figure 3.3 shows the combined kaon probability for charged tracks. A K/π separation cut is applied for them; kaon candidates with a probability of greater than 0.9 and pion candidates with less than 0.9. The kaon selection efficiency for real data is typically 65% while the pion selection efficiency is 98%. The four momentum of each track is given according to its particle (mass) hypothesis.

3.5 Neutral kaon(K^0_S) selection

K^0_S is reconstructed from π^+ and π^-. Every charged track is taken as a pion, regardless of the PID information. We select good K^0_S candidates based on the following variables.

- dr : The closest approach of either track from the run-dependent IP in $x-y$ plane. (Either pion must not come from the IP as a primary decay product of B.)
- $d\phi$: The azimuthal angle between the K^0_S momentum direction and the K^0_S vertex direction in regard to the run-dependent IP. (K^0_S vertex position must be in a direction consistent to its momentum.)

$\vert\vec{p}\vert$ (GeV/c)	dr (cm)	$d\phi$ (cm)	z_dist (cm)	fl (cm)
< 0.5	> 0.05	< 0.3	< 0.8	–
$0.5 - 1.5$	> 0.03	< 0.1	< 1.8	> 0.08
> 1.5	> 0.02	< 0.03	< 2.4	> 0.22

Table 3.2: K^0_S quality cuts summary

- z_dist : The distance between the two tracks at their interception point in $x - y$ plane. (The two tracks must form a vertex.)
- fl : The flight length of the K^0_S in $x - y$ plane. (K^0_S has a finite lifetime.)

The K^0_S quality cuts are applied according to its momentum as summarized in Table 3.2. Finally, the reconstructed mass is required to be within 8 MeV/c^2 from the nominal K^0 mass.

Figure 3.4 shows distributions of the listed four quality variables and Figure 3.5 shows the K^0_S invariant mass distribution. The K^0_S selection efficiency is approximately 60%.

3.6 Neutral pion(π^0) selection

Neutral pion candidates are reconstructed from two photon clusters each with more than 20 MeV energy deposit. The invariant mass is required to be within 16 MeV/c^2 of the nominal π^0 mass. Then the π^0 momentum is recalculated with a mass constraint fit.

Figure 3.6 shows the reconstructed two photon mass distribution. There remain many combinatorial background events without any further cut. We use only upto 1 π^0 to form a recoil system candidate, and the contribution of π^0's to the signal reconstruction efficiency is not very large, so we do not badly need to improve our π^0 selection at this moment. The π^0 selection efficiency is approximately 60%, taking the effects of acceptance and photon finding deficiencies into account.

3.7 Recoil system (X_s) reconstruction

The X_s intermediate state is reconstructed from 1 kaon (either $K^\pm$ or K^0_S) and 1 to 4 pions (including 0 or 1 π^0). Therefore, we have 16 different combination modes – whether kaon is charged or neutral (2 ways) times number of pions (4 ways) times whether π^0 is included or not (2 ways) – in X_s (hence B) reconstruction. To represent these 16 modes in short, we use four digit numbers; each digit denotes the number of $\pi^0, \pi^\pm, K^0_S, K^\pm$, from left to right. For example, "mode 1201" means $K^\pm\pi^+\pi^-\pi^0\gamma$ mode. As for the possibilities to reconstruct X_s with more pions, we will discuss in appendix A.

The total charge of an X_s candidate is required to be 0 or ± 1. The charge sum of the pions of the X_s is also required to be 0 or ± 1, too. The second requirement forbids for example a combination like $K^+\pi^-\pi^-\gamma$; which must be a decay from B^- and then the B and K meson charges become inconsistent. The decay vertex of an X_s candidate is calculated from all of the used charged particles with the run-dependent beam profile constraint. The beam profile used here is obtained from vertices of Bhabha scattering, and then smeared by the effect of

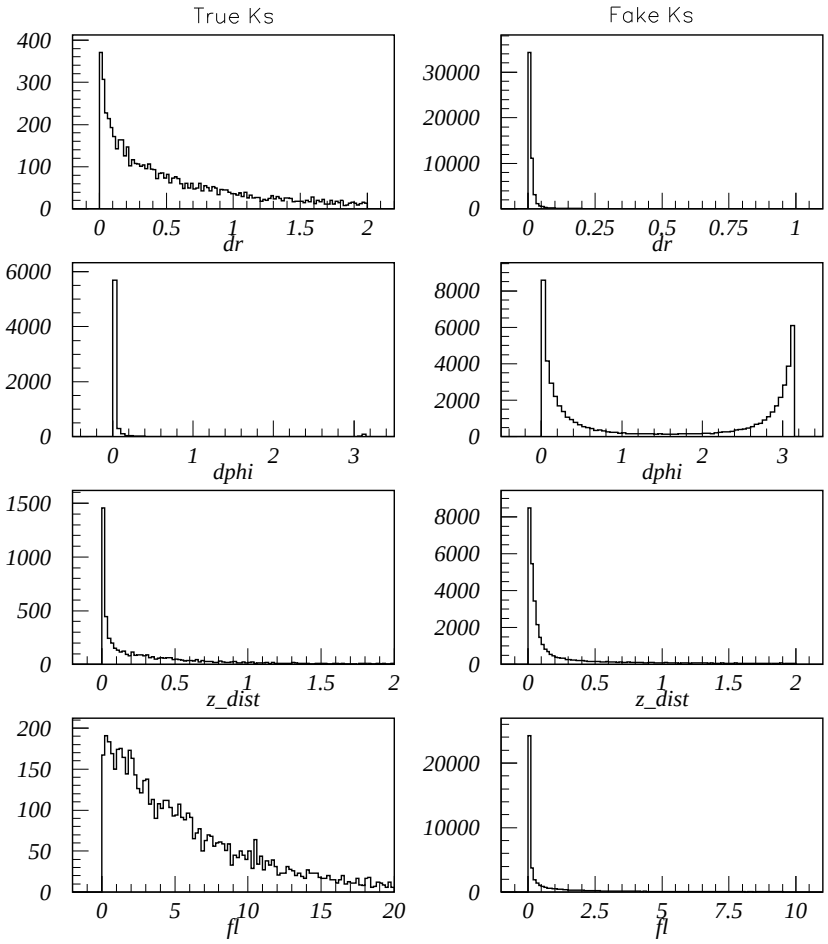

Figure 3.4: The four variables described in text for MC tagged K_S^0 (left) and for random combinations (right). Plots are made without applying the mass cut.

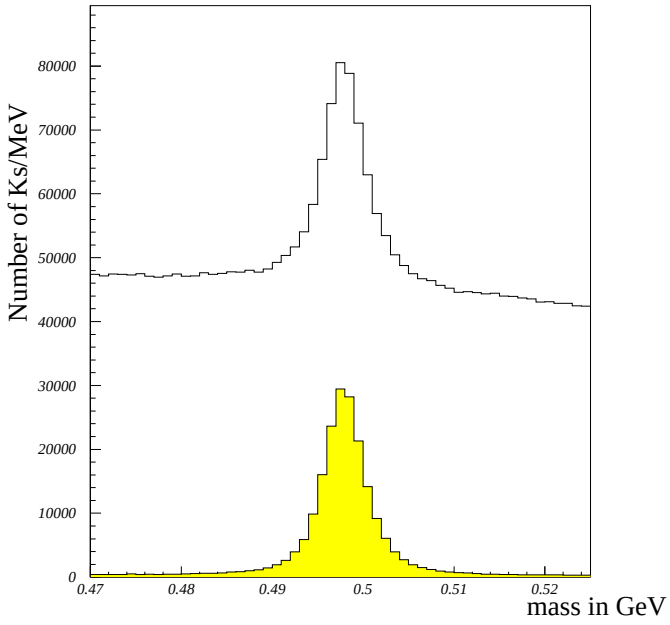

Figure 3.5: K_S^0 invariant mass distribution before the four quality cuts (open) and after (solid).

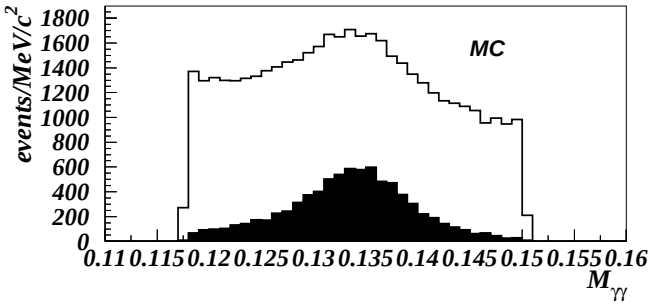

Figure 3.6: Invariant mass distribution of $\pi^0 \to \gamma\gamma$ candidate in $q\bar{q}$ MC – for all combination (open) and for MC tagged π^0 (solid).

the finite lifetime of B mesons. Except for the $K^0_S\pi^0\gamma$ mode, all other 15 modes can form a vertex. For these 15 modes, we require the vertex confidence level to be nonzero, namely we remove candidates those which could not form a vertex at all.

3.8 B reconstruction

The primary photon candidate and an X_s candidate are combined to form a B meson candidate. Two independent kinematic variables, the beam constrained B meson mass (M_B) and the energy difference (ΔE) are calculated in the Υ(4S) rest frame, which are defined as follows.

$$M_B = \sqrt{{E_{beam}}^2 - |\vec{p}_B|^2} \quad (3.1)$$

$$\Delta E = E_{X_s} + E_\gamma - E_{beam}. \quad (3.2)$$

In order to reject wrong combinations, cuts are applied to these variables. We require $M_B > 5.2$ GeV/c^2 and $-0.150 < \Delta E < 0.100$ GeV. The ΔE distribution for signal MC is shown in Figure 3.7. The M_B distribution will show up in Figure 4.7 of section 4.2.

In addition, the angle between X_s and γ in the Υ(4S) rest frame [3] ($\angle X_s\gamma$) is calculated, and required to be greater than 167°. With this back-to-back cut, a correlation between SFW and M_B vanishes to the level which we will discuss later in section 4.1.1. Figure 3.8 shows the $\angle X_s\gamma$ for MC tagged signal events. Since $\angle X_s\gamma$ is correlated with M_B a cut on $\angle X_s\gamma$ makes the beam constrained mass distribution for background enhanced around the B meson mass, too. It will be shown in Figure 4.1 in section 4.1.1. Nevertheless, this cut is necessary to reduce the correlation between SFW and M_B and to understand our background.

3.9 Best candidate selection

One inherent problem in our inclusive analysis of $B \to X_s\gamma$ is that we can form a large number of possible candidates as shown in Figure 3.9. The reason is because we form candidates in 16 different combination modes, and each of these mode can have more than one candidate. Even after the cuts applied above, we are left with 5 candidates in average for a signal event.

This requires the "best" or "most B like" candidate to be selected. We select the best candidate based upon the vertex of the X_s candidate. For the 15 modes that can form a vertex (except for $K^0_S\pi^0\gamma$ mode), the candidate with the best vertex confidence level is selected. The candidate with the largest $\angle X_s\gamma$ is chosen in the following cases:

1. there is no charged kaon or pion which forms the vertex ($K^0_S\pi^0\gamma$ mode)
2. there remains an ambiguity whether to add a π^0
3. there are several π^0 and K^0_S candidates to choose from.

[3] One may say that the X_s and the photon is back-to-back not in the Υ(4S) rest frame but in the B rest frame. Although the comment is completely true, since we form the B meson four momentum from the momenta of the X_s and the photon, they are back-to-back by definition in the B rest frame, and the variable makes no sense.

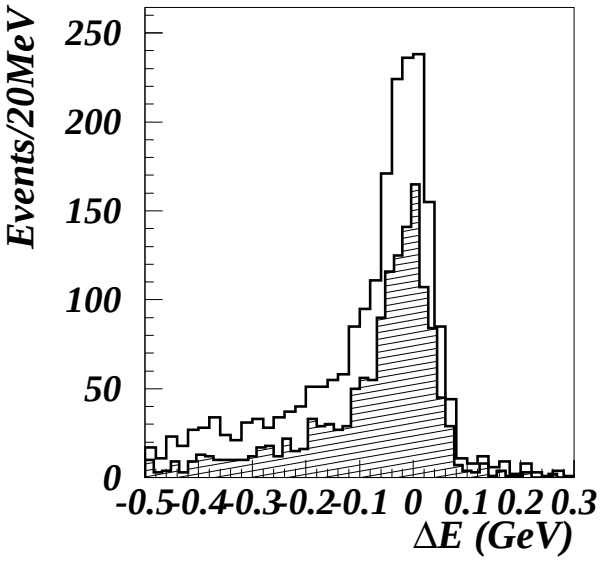

Figure 3.7: The energy difference ΔE for MC tagged signal events in the preselection box (open) and in the final cut box (hatched). The distribution peaks at 0 and have larger tail in negative side due to the shower leakage in the photon reconstruction.

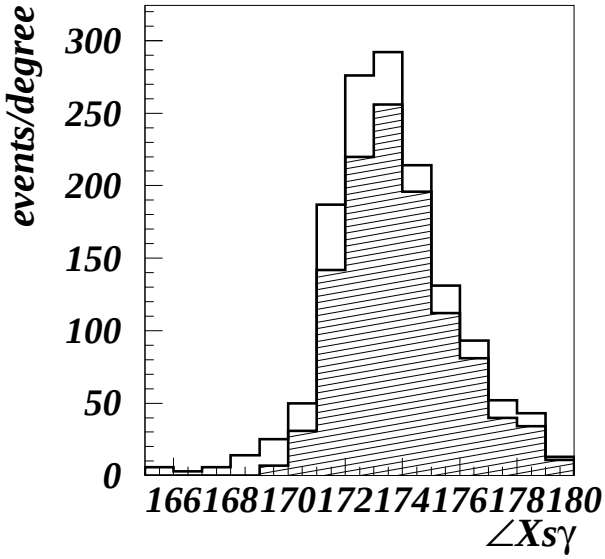

Figure 3.8: Angle between X_s and γ for MC tagged signal events in the preselection box (open) and in the final cut box (hatched). The distribution does not peak at 180° due to the nonzero momentum of B meson in the Υ(4S) rest frame.

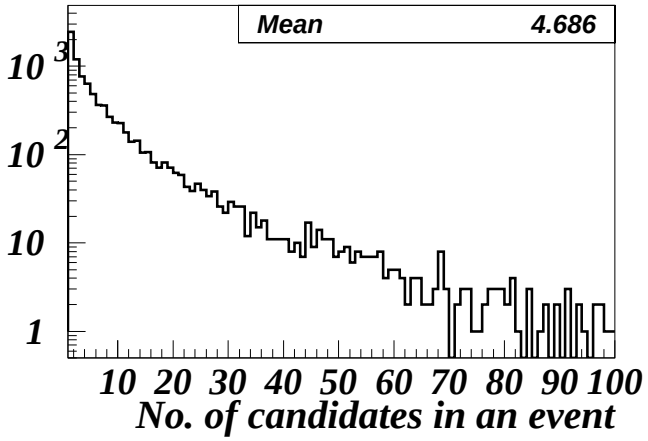

Figure 3.9: Number of possible B candidates per event for signal MC.

Selection by the vertex information does not make the $q\bar{q}$ background events be peaked [4] at the nominal B meson mass, which allow us to extract the signal yield from the observed beam constrained mass spectrum.

We call the cuts applied before/after selecting the best candidate as "preselection"/"final cut". Mode by mode signal population before and after the final cut is listed in the Table 3.3. Among the reconstructed events after the final cut, 78% were generated in one or two pion mode. In total, 68% are reconstructed correctly in generated mode [5]. The reduction factor of the number of events reconstructed in correct mode by the final cut is 31%, 25%, 13% and 4% for one to four pion mode, respectively. The final cut is tighter for the higher multiplicity mode, which is mostly due to the X_s mass cut. Tight cuts, especially on the X_s mass, leads a large model dependency. But it makes the systematic uncertainty smaller. Since we do not have enough off-resonance data to understand the $q\bar{q}$ background, we stay with rather tight cuts comparing to CLEO's analysis.

3.10 $q\bar{q}$ background suppression

$q\bar{q}$ light quark pair production is the largest background in this analysis. The high energy photon either from ISR or from high energy π^0 or η decays fakes our signal photon. The photon property cuts take an important role to suppress these background events as described in section 3.3. In this section, we introduce another powerful suppression method generally used to suppress $q\bar{q}$ background, which is the event shape variable.

The basic idea of the event shape variable is as follows. The $\Upsilon(4S)$ mass is just about twice of the B meson mass. Therefore, in the $\Upsilon(4S)$ rest frame, when the $\Upsilon(4S)$ decays into

[4] Unfortunately, as mentioned in section 3.8, the $\angle X_s\gamma$ cut makes the $q\bar{q}$ events be enhanced around the nominal B meson mass.

[5] Naively, this does not mean that the signal is reconstructed with the correct particles.

	0101	0201	0301	0401	1001	1101	1201	1301	0110	0210	0310	0410	1010	1110	1210	1310	sum
0101	**731**	117	28	14	90	252	147	58	4	0	0	0	0	6	2	0	1449
0201	6	**418**	88	43	8	107	329	135	1	2	1	0	0	4	3	2	1147
0301	0	4	**59**	20	0	4	57	97	0	0	0	2	0	0	0	4	247
0401	0	0	3	**22**	0	1	5	23	0	0	0	0	0	0	0	2	56
1001	20	20	9	7	**282**	134	88	30	0	1	0	0	0	1	1	0	593
1101	3	56	45	19	11	**408**	244	146	1	1	0	0	0	3	2	0	939
1201	2	24	72	62	4	57	**432**	311	0	2	1	2	0	0	4	8	981
1301	0	7	15	47	0	2	46	**145**	0	0	0	0	0	0	0	3	265
0110	9	19	3	1	0	24	22	14	**224**	12	3	1	6	115	21	10	484
0210	0	6	11	7	0	7	38	21	4	**41**	10	3	0	43	29	18	238
0310	0	3	5	6	0	0	8	19	0	3	**9**	1	0	9	16	17	96
0410	0	0	0	1	0	0	1	2	0	0	0	**0**	0	0	0	2	6
1010	0	0	2	0	1	9	7	8	9	4	2	0	**34**	58	19	2	155
1110	1	4	9	2	0	17	36	37	0	19	10	1	0	**135**	57	26	354
1210	0	4	5	4	0	4	23	36	0	2	14	1	1	14	**58**	44	210
1310	0	1	1	4	0	0	7	21	0	2	5	6	0	1	10	**34**	92
2001	2	5	0	1	5	21	20	17	0	0	0	0	0	1	1	1	74
2101	0	3	7	8	0	14	49	43	0	0	0	0	0	0	1	5	130
2201	0	2	4	9	0	3	28	72	0	0	0	1	0	1	2	4	126
2301	0	0	0	10	0	0	4	21	0	0	0	0	0	0	0	1	36
2010	0	0	0	0	1	1	2	1	1	0	0	1	0	5	0	4	16
2110	0	1	1	1	0	1	5	9	1	0	1	0	0	7	5	7	39
2210	0	1	0	1	0	0	4	10	0	0	0	0	0	0	2	5	23
2310	0	0	0	1	0	0	2	4	0	0	0	0	0	0	0	0	7
others	16	40	62	77	15	112	267	402	3	4	10	9	2	35	33	81	1168
sum	790	735	429	367	417	1178	1871	1682	248	93	66	28	43	438	266	280	8931

	0101	0201	0301	0401	1001	1101	1201	1301	0110	0210	0310	0410	1010	1110	1210	1310	sum
0101	**228**	15	1	0	13	32	8	1	1	0	0	0	0	0	0	0	299
0201	0	**112**	3	0	3	11	26	2	0	0	0	0	0	0	0	0	157
0301	0	0	**7**	1	0	0	1	0	0	0	0	0	0	0	0	0	9
0401	0	0	1	**0**	0	0	0	0	0	0	0	0	0	0	0	0	1
1001	2	3	0	0	**90**	10	1	0	0	0	0	0	0	0	0	0	106
1101	0	6	1	0	1	**103**	24	1	0	0	0	0	0	0	0	0	136
1201	0	3	7	2	0	5	**56**	9	0	0	0	0	0	0	0	0	82
1301	0	0	0	0	0	0	6	**7**	0	0	0	0	0	0	0	0	13
0110	0	0	0	1	0	0	0	0	**60**	1	1	0	2	15	0	0	80
0210	0	1	0	0	0	0	2	0	0	**12**	0	0	0	7	6	0	28
0310	0	0	0	0	0	0	0	0	0	0	**2**	0	0	2	4	1	9
0410	0	0	0	0	0	0	0	0	0	0	0	0	0	0	0	0	0
1010	0	0	0	0	0	0	0	0	2	0	0	0	**12**	9	2	0	25
1110	0	0	0	0	0	2	2	1	0	4	1	0	0	**28**	5	0	43
1210	0	0	0	0	0	0	0	0	0	0	0	0	0	3	**6**	1	10
1310	0	0	0	1	0	0	1	0	0	0	0	0	0	0	1	**1**	4
2001	1	1	0	0	0	1	0	0	0	0	0	0	0	0	0	0	3
2101	0	0	0	0	0	1	6	1	0	0	0	0	0	0	0	0	8
2201	0	0	0	1	0	2	0	1	0	0	0	0	0	0	0	0	4
2301	0	0	0	0	0	0	0	2	0	0	0	0	0	0	0	0	2
2010	0	0	0	0	0	0	0	0	0	0	0	0	0	0	0	0	0
2110	0	0	0	0	0	0	0	0	0	0	0	0	0	0	0	0	0
2210	0	0	0	0	0	0	0	0	0	0	0	0	0	0	1	0	1
2310	0	0	0	0	0	0	0	0	0	0	0	0	0	0	0	0	0
others	4	4	2	1	6	10	8	3	0	0	0	0	0	4	2	3	47
sum	235	145	22	7	113	177	141	28	63	17	4	0	14	68	27	6	1067

Table 3.3: Mode by mode population for signal MC which contains 38K events at the beginning. The upper table is after the preselection and before the final cuts, while the lower table is after the final cuts. Rows represent the generated mode and columns represent the reconstructed mode. The definition of the four digit number is given in section 3.7.

two B mesons, the B's are almost at rest. This leads to a spherical event topology for $B\bar{B}$ decay. On the other hand, if we create a $q\bar{q}$ pair of lighter quarks ($q = u, d, s, c$) with the same energy, the quarks will fragment into back to back jets leading to a jetty event topology. Thus, we can distinguish $B\bar{B}$ events from $q\bar{q}$ events by checking the event topology.

3.10.1 Fox-Wolfram Moment

The Fox-Wolfram moments H_l, l = 0,1,2,... are defined as follows.

$$H_l = \sum_{i,j} \frac{|\vec{p_i}||\vec{p_j}|}{E_{vis}^2} P_l(\cos\theta_{ij}), \tag{3.3}$$

where θ_{ij} is the opening angle between particles i and j, E_{vis} is the total visible energy of the event, and $P_l(x)$ is the Legendre polynomial of order l. For a spherical event, H_l tend to be $\approx$ 0. For 2-jet events, H_{2l} tend to be ≈ 1 and H_{2l+1} tend to be ≈ 0. Usually, the Fox-Wolfram moments are normalized to H_0 and give $R_l = H_l/H_0$.

3.10.2 Super Fox-Wolfram

In this analysis we know which tracks come from one B and which tracks come from the other B. We can thus divide an R_l into three variables according to the suffixes i and j in equation 3.3 :

- *kinematic* part :
  i and j run over the decay particles of the $B \to X_s\gamma$;
- *major* part :
  i runs over the decay particles of the $B \to X_s\gamma$, j runs over the other B;
- *minor* part :
  i and j run over the particles which are not used to form the $B \to X_s\gamma$.

We linearly combine six variables R_l^{major} ($l = 2, 4$) and R_l^{minor} ($l = 1, 2, 3, 4$) into a single variable which we call the Super Fox-Wolfram (SFW). $R_l^{kinematic}$ terms are highly correlated with the kinematic variables we have used already to reconstruct the B meson, so we throw these terms out. R_1^{major} and R_3^{major} are also correlated and thrown out. In order to remove a correlation further, only the primary photon is used among the decay particles of $B \to X_s\gamma$. In addition, since this variable is not a Lorentz invariant, it takes different values in different coordinate systems; we chose the signal side B meson rest frame to calculate these moments instead of the popularly used Υ(4S) rest frame. This helps a lot to reduce the correlation between the SFW and the M_B, which will be discussed in section 4.1.1 (Figure 4.2). The SFW can finally be written as follows :

$$\mathrm{SFW} = \sum_{l=2,4} \alpha_l R_l^{maj} + \sum_{l=1,2,3,4} \beta_l R_l^{min} \tag{3.4}$$

where the R_l's are defined as

$$\begin{aligned} R_l^{major} &= \frac{\sum_{i,\gamma} |\vec{p_i}||\vec{p_\gamma}| P_l(\cos\theta_{i\gamma})}{\sum_{i,\gamma} |\vec{p_i}||\vec{p_\gamma}|} \\ R_l^{minor} &= \frac{\sum_{i,j} |\vec{p_i}||\vec{p_j}| P_l(\cos\theta_{ij})}{\sum_{i,j} |\vec{p_i}||\vec{p_j}|}. \end{aligned} \tag{3.5}$$

The Fisher Discriminant [36] coefficients α_2, α_4, β_1, β_2, β_3 and β_4 are chosen to maximize the separation between signal and background. The values are listed in Table 3.4.

term	coefficient	term	coefficient
		β_1	-0.448423
α_2	-2.87846	β_2	-0.540553
		β_3	0.238562
α_4	-0.775015	β_4	0.876081

Table 3.4: Coefficients for the SFW fisher discriminant

The SFW variable gives a good signal to $q\bar{q}$ background seperation as shown in Figure 3.10. A detailed explanation of Figure 3.10 will be given in section 4.1.1 where the SFW plays another important role. We can also add the higher R_l^{maj}'s or R_l^{min}'s, or other shape variables like thrust, virtual calorimeter, and so forth, but nothing improved the separation significantly any further.

3.11 Suppression of background from Υ(4S)

The background contribution from B decay processes other than $B \to X_s\gamma$ is estimated from generic $B\bar{B}$ MC sample. The total amount of these background contributions are expected to be small comparing to the $q\bar{q}$ background.

In viewpoint of the quark decay, background is categorized into $b \to cW^-$ and $b \to uW^-$. The $b \to uW^-$ channel is KM suppressed and much smaller than the contribution via $b \to cW^-$ channel. To suppress the $b \to cW^-$ channel, we require the X_s mass to be less than 2.05 GeV/c^2. In order to decrease the theoretical extrapolation error, looser X_s mass cut is more preferable. On the other hand, a tight X_s mass cut helps to reduce the correlation between the SFW and the M_B as we will discuss in section 4.3. The cut is chosen as loose as possible while controlling the correlation.

The background comes mainly in case a high energy π^0 or η yields a high energy photon. For example, $B \to D\rho^\pm$ and $\rho^\pm \to \pi^\pm\pi^0$ yields a high momentum π^0. This kind of background will be suppressed by the π^0/η veto and the shower shape cut.

Since the B meson lifetime is not short, B and $\bar{B}$ decay at different positions. Therefore, unlike $q\bar{q}$ background, the decay particles may not come from one vertex. The X_s vertex cut can suppress $B\bar{B}$ background when tracks are picked up not from a single but from both B mesons.

Antineutron ($\bar{n}$) may be another background source in this analysis. If an $\bar{n}$ annihilate in a CsI crystal, there will be a large energy deposit. We do not really know the $\bar{n}$ spectrum in B decay since it has not been (and will not be) measured, nor the response of CsI calorimeter to $\bar{n}$ since we do not (and will not) have an $\bar{n}$ beam test result. The amount of such unknown background contribution is, however, small enough after all the cuts are applied as we will discuss in section 4.1.2.

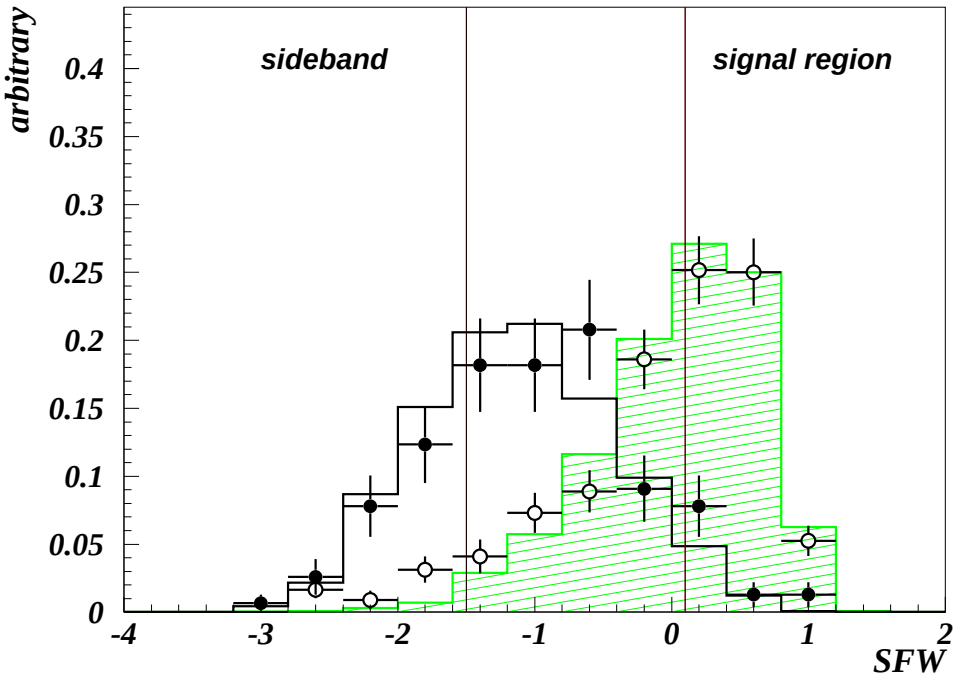

Figure 3.10: Super Fox-Wolfram variable comparison between data and MC – MC signal (hatched histogram) and $B \to D\pi$ data (open circles) distributes in higher side; $q\bar{q}$ MC (open histogram) and off-resonance data (solid circles) distributes in lower side.

3.12 Summary of Cuts

A summary of the preselection and the final cut, with signal efficiency and background reduction factor is given in Table 3.5. The efficiency numbers are obtained from MC studies.

For the photon, applying cuts at preselection or at the final cut does not make any physical difference since we take the most energetic photon as one single candidate. In the actual manner, we only apply the E_γ cut at the preselection, and all other cuts in final.

Note again that the cuts on M_{X_s} and E_γ in the preselection are redundant; (1) the M_{X_s} preselection after E_γ preselection has no effect except for the computing power consumption, and (2) the E_γ preselection has no effect with tight M_{X_s} cut finally.

	total efficiency		
	$B \to X_s\gamma$(%)	$q\bar{q}(\times 10^{-6})$	$B\bar{B}(\times 10^{-6})$
preselection			
$1.8 < E_\gamma < 3.4$ GeV	—	—	—
$M_{X_s} < 3.5$ GeV/c^2	—	—	—
X_s vertex confidence level >0	—	—	—
$\angle X_s\gamma > 167$ °	—	—	—
$M_B > 5.2$ GeV/c^2	—	—	—
$-0.150 < \Delta E < 0.100$ GeV	—	—	—
preselection total	24.5	7180	887
final cut			
$33° < \theta_\gamma < 132°$	20.8	6057	765
E9/E25 > 0.95	19.2	4035	675
π^0/η veto	14.1	1339	209
$M_{X_s} < 2.05$ GeV/c^2	8.0	450	14
$M_B > 5.27$ GeV/c^2	5.6	114	3.9
SFW > 0.1	2.8	5.6	1.5

Table 3.5: summary of event selection and efficiency

Chapter 4

Data analysis

4.1 Background subtraction

To extract the amount of signal events in our data, we have to estimate and subtract the background. Therefore we must know its shape and normalization. For this purpose, we try to use data as much as possible and rely on MC as little as possible, in order to avoid systematic uncertainty.

We will find that the $q\bar{q}$ background contribution can finally be subtracted by using the SFW sideband data after a full workout on the SFW variable. We will also see that the $B\bar{B}$ background contribution is small enough and can be explained by our MC.

4.1.1 $q\bar{q}$ background

$q\bar{q}$ background shape

Traditionally in B physics at $\Upsilon(4S)$ resonance, off-resonance data are used to estimate the $q\bar{q}$ background. However, in the first stage of an asymmetric B factory experiment, we have the top priority in measuring the $\sin 2\phi_1$ of the Kobayashi-Maskawa unitarity triangle, for which we do not need off-resonance data so much. Hence, we do not have enough off-resonance data that we can use to subtract the $q\bar{q}$ background in this analysis, unfortunately.

Instead, we introduce a new method utilizing the SFW sideband data as the $q\bar{q}$ background sample,. Figure 3.10 shows comparisons of SFW shapes for the off-resonance data to the $q\bar{q}$ MC and the $B \to D\pi$ data to the $X_s\gamma$ signal MC. There is a reasonable agreement between the $q\bar{q}$ MC and the off-resonance data. To compare the signal MC with the $B \to D\pi$ data, we treat the primary pion in $B \to D\pi$ as the primary photon to calculate the SFW. The $q\bar{q}$ background contamination in the $B \to D\pi$ data is subtracted by fitting the beam constrained mass distribution with Gaussian plus ARGUS function[1]. The SFW sideband region was chosen as SFW<-1.5 so that there are a large number of background events. In the sideband region, there are about 6 times as large statistics of $q\bar{q}$ events as in the signal region (SFW<0.1). Signal events in the SFW sideband region is expected to be only 0.7%. $B\bar{B}$ background is also negligible in this region, because its event topology and SFW shape is similar to that of the signal.

[1]The ARGUS function describes the background shape for the beam constrained mass well. It is defined with two free parameters P_1 and P_2 as $f(x) = P_1 x \sqrt{1-\left(\frac{x}{E_{beam}}\right)^2} \exp\left\{P_2\left(1-\frac{x}{E_{beam}}\right)^2\right\}$

The SFW must not have correlation with the beam constrained mass, with which we do subtract the $q\bar{q}$ background. Otherwise we will subtract an incorrect shape and therefore a wrong amount. This finally worked with the following ideas.

Figure 4.1 shows how the beam constrained mass distribution for $q\bar{q}$ background changes with various $\angle X_s\gamma$ cut. In order to make this plot, $\angle X_s\gamma$ cut is removed from preselection and applied at the final cut temporary for convenience. Our $\angle X_s\gamma$ preselection was chosen as 167°, to suppress the correlation.

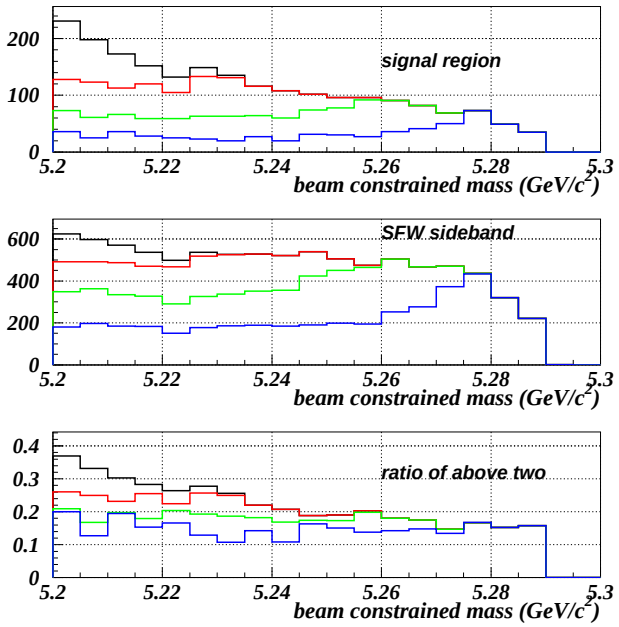

Figure 4.1: Beam constrained mass distribution for $q\bar{q}$ MC – in signal region(Top), in SFW sideband(Middle) and the ratio of the two(Bottom) with different $X_s\gamma$ angle cut. Cut values are, from outer to inner, >0°, >160°, >165°and >170°. Our cut is chosen as >167°.

Figure 4.2 shows a comparison between two SFW variables. The "standard" SFW is calculated in the $\Upsilon(4S)$ rest frame from 8 input variables, R_l^{major} and R_l^{minor} for $l = 1, 2, 3, 4$. The "improved" SFW, described in section 3.10.2, removes the previously existing correlation with M_B as showin in Figure 4.2. We call the "improved" SFW just as SFW for simplicity throughout the thesis.

Figure 4.3 shows a comparison of beam constrained mass spectra in the SFW sideband and in the signal box for the $q\bar{q}$ MC and for the off-resonance data. In either case, the spectra are consistent within error. We conclude that M_B shape for $q\bar{q}$ background in signal region is well described by the shape in SFW sideband. Figure 4.4 shows the M_B shape for on-resonance data in the SFW sideband. The shape is generally similar to that for MC, if we are aware of the fact there can be a systematic difference between MC and data. The systematic effect on the signal yield will be estimated in section 4.2 and the systematic effect on the signal reconstruction efficiency will be estimated in section 5.2.

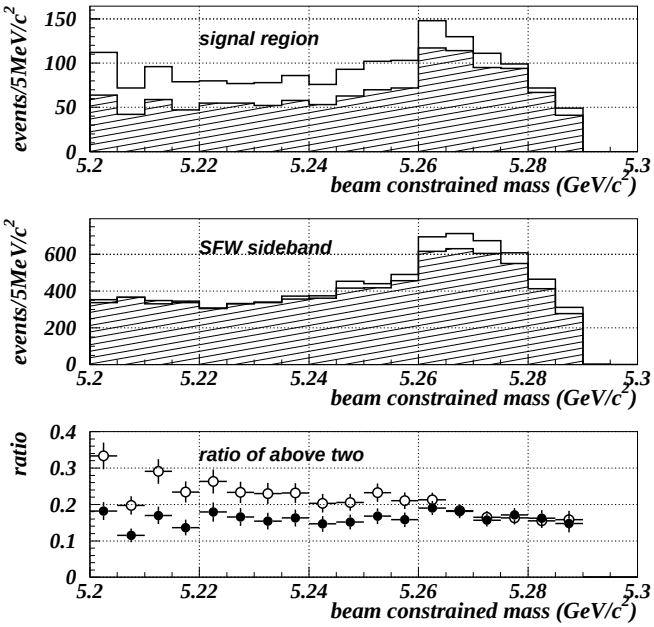

Figure 4.2: Beam constrained mass distribution for $q\bar{q}$ MC – in signal region (top), in SFW sideband (middle), and the ratio of the two (bottom) with standard SFW (open histogram or open circles) and with improved SFW(hatched histogram or solid circles).

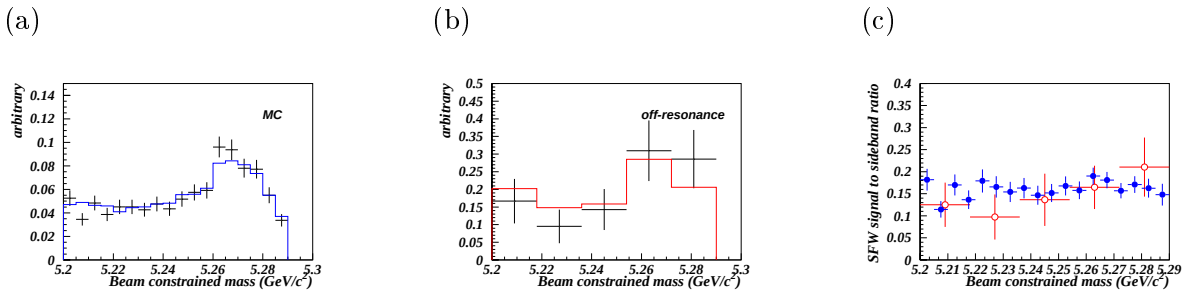

Figure 4.3: Beam constrained mass spectra for $q\bar{q}$ events – $q\bar{q}$ MC (a) in SFW sideband (histogram) and in SFW signal region (error bars)
off-resonance data (b) in SFW sideband (histogram) and in SFW signal region (error bars)
Ratio of Spectra in SFW signal region to in SFW sideband (c) for $q\bar{q}$ MC (solid circles) and off-resonance data (open circles).
Flat distribution in (c) demonstrates that the SFW and the beam constrained mass are uncorrelated.

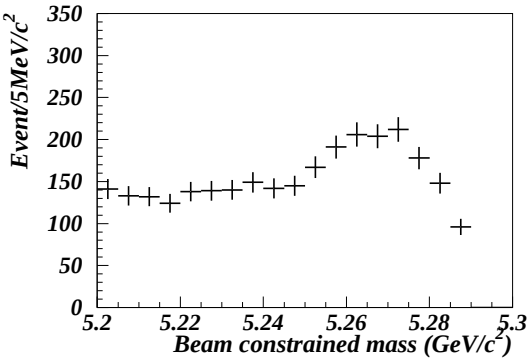

Figure 4.4: Beam constrained mass spectra for $q\bar{q}$ events for the on-resonance data in the SFW sideband region.

Estimation of the continuum background yield

To subtract the $q\bar{q}$ background spectrum in the signal region, we have to scale the sideband spectrum properly since the amount of $q\bar{q}$ background in the signal region is about 1/6 of that in the SFW sideband. Signal to sideband region scaling factor is defined from the two beam constrained mass spectra for $q\bar{q}$ background $f_{q\bar{q}}^{signal\ region}(m)$ and $f_{q\bar{q}}^{SFW\ sideband}(m)$ as $r_{q\bar{q}}$ in the equation below.

$$f_{q\bar{q}}^{signal\ region}(m) = r_{q\bar{q}} \times f_{q\bar{q}}^{SFW\ sideband}(m) \tag{4.1}$$

First, we estimate the $r_{q\bar{q}}$ both from $q\bar{q}$ MC and from off-resonance data.

Figure 4.3(c) is the beam constrained mass spectrum in the signal region divided by that in the sideband for $q\bar{q}$ MC and for off-resonance data. In both cases, the flat distributions demonstrate that the beam constrained mass and the SFW do not have a significant correlation. Although the off-resonance data size is statistically limited, off-resonance data points are consistent to the MC data points within the statistical fluctuations. Fitting the distribution by a constant, the scaling factor $r_{q\bar{q}}$ is obtained to be 0.160 ± 0.005 from MC.

The $r_{q\bar{q}}$ for the on-resonance data will be decided by fitting later (in section 4.2), and confirmed to be consistent to the MC expectation.

4.1.2 Υ(4S) background

We do not have a clean Υ(4S) background sample. The SFW sideband is not usable for Υ(4S) background since the SFW shape for $B\bar{B}$ background is similar to that of the $B \to X_s\gamma$ signal. In order to estimate the background from Υ(4S), we use a well tuned MC. Figure 4.5 shows the momentum spectrum for π^0 from B decay [37]. Our generic $B\bar{B}$ MC reproduces the π^0 momentum spectrum in the relevant momentum region, and therefore describes the $B\bar{B}$ background well.

We checked the SFW shape in the M_B sideband region (M_B<5.25), where the signal population is small. Without the vertex cut on X_s, we see a bulk of events in our SFW signal region as shown in Figure 4.6(a), which cannot be explained by our $B\bar{B}$ MC. This is

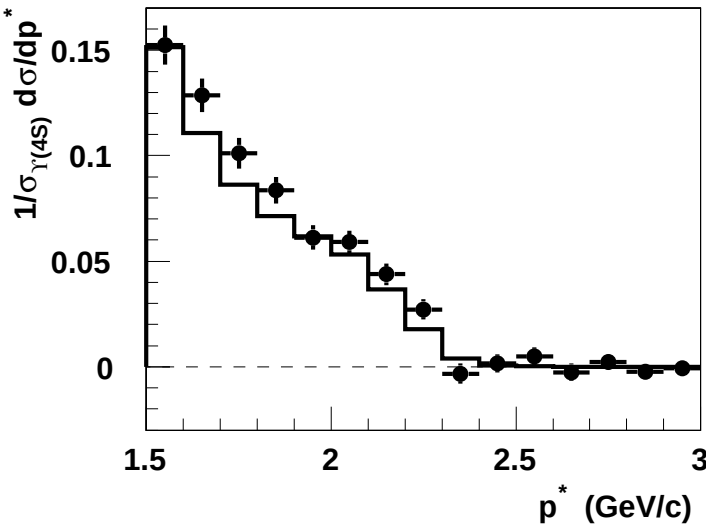

Figure 4.5: The momentum spectrum for π^0 from B decay – MC (histogram) and data (error bars) shows a general agreement in the relevant high momentum region.

possibly due to a systematic difference in the SFW calculation between data and MC, or due to background contributions which are not implemented in our $B\bar{B}$ MC properly – it may be from non-$B\bar{B}$ Υ(4S) decay[2], or from antineutron, or anything else. But, with our vertex cut on X_s which requires the vertex confidence level to be nonzero, the unknown contribution is decreased to a negligible level and the background contribution become consistent to our $B\bar{B}$ MC estimation as shown in Figure 4.6(b). We note that the error bars in Figure 4.6 are statistical only; the systematic error will be estimated in section 5.2.7.

4.2 The B mass spectrum and the signal yield

We know the beam constrained mass spectrum of the main background ($q\bar{q}$) from the SFW sideband data with a better statistics. We use $B\bar{B}$ MC for Υ(4S) background. The $B\bar{B}$ background, whose contribution in the signal region is estimated to be $9.1\pm$ 1.8, is subtracted from the data. We then do a likelihood fit for the remaining data spectrum with the SFW sideband and the signal MC spectra, floating the normalization of each spectrum. The result is shown in Figure 4.7. The scaling factor $r_{q\bar{q}}$ determined by the fit is 0.168 ± 0.010, which is consistent to our estimation in section 4.1.1. Fitting confidence level was 70.9%. The M_B resolution for data is approximately 4.4 MeV/c^2.

To test the effect of the variation of $r_{q\bar{q}}$ with M_B, the sideband spectrum is artificially tilted and the fitting procedure is redone. With a constant slope, making the population at 5.3 GeV/c^2 10% higher(lower) than what it is while keeping the population at 5.2 GeV/c^2 as it is, the background yield in the signal region will be overestimated(underestimated). We found $\pm$4.7% error on the signal yield.

[2]Non-$B\bar{B}$ decay from Υ(4S) does not necessarily have a spherical event topology.

(a) (b)

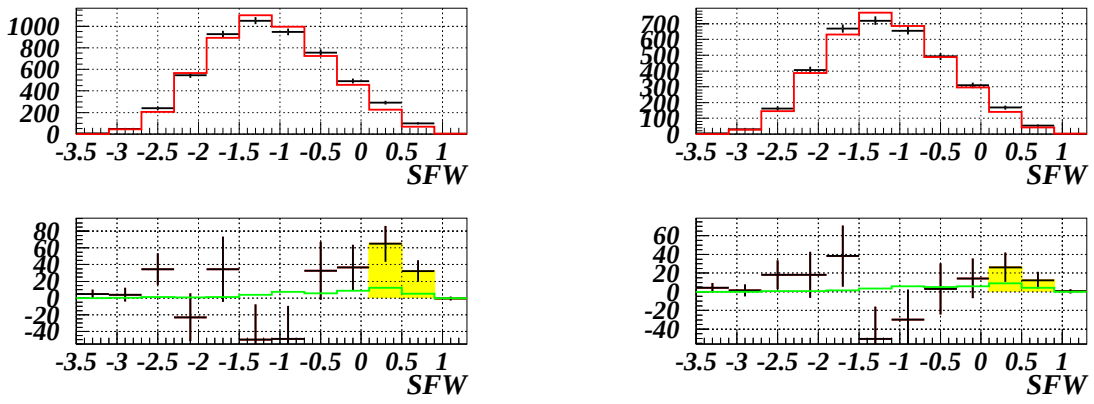

Figure 4.6: SFW distribution in M_B<5.25 with (b) and without (a) the vertex cut on X_s– [Top] Data (error bars) in comparison to $q\bar{q}$ MC (histogram)
[Bottom] $q\bar{q}$ contribution is subtracted (error bars) and compared to $B\bar{B}$ MC (open histogram). Enhancement in our signal region (SFW>0.1) can not be explained by our $B\bar{B}$ MC in (a); it becomes consistent with the vertex cut (b).

The numbers of observed signal and background events are listed in Table 4.1. We observed

$$106.5 \pm 16.7 \pm 5.3 \tag{4.2}$$

of signal events. The first error is statistical, which is propagated from the following terms and will be added to the overall statistical error.

- the statistical error on the observed events
- the fitting error on the $q\bar{q}$ background

The second error is systematical, which is propagated from the following terms and will be added to the overall systematic error.

- the statistical error on the $B\bar{B}$ MC
- the systematic effect of the variation of $r_{q\bar{q}}$ with M_B

4.3 X_s mass spectrum

The SFW variable has a significant correlation with the X_s mass. As shown in Figure 4.8, the ratio of two M_{X_s} spectra in the signal region to the sideband is flat in the lower M_{X_s} region, but blows up in the higher M_{X_s} region. For the $q\bar{q}$ background subtraction, we use the $q\bar{q}$ MC spectrum, which is normalized by the number of events obtained as in Table 4.1 in section 4.2. Figure 4.9 shows the extracted M_{X_s} spectrum. We see a clear peak of $K^*(892)$

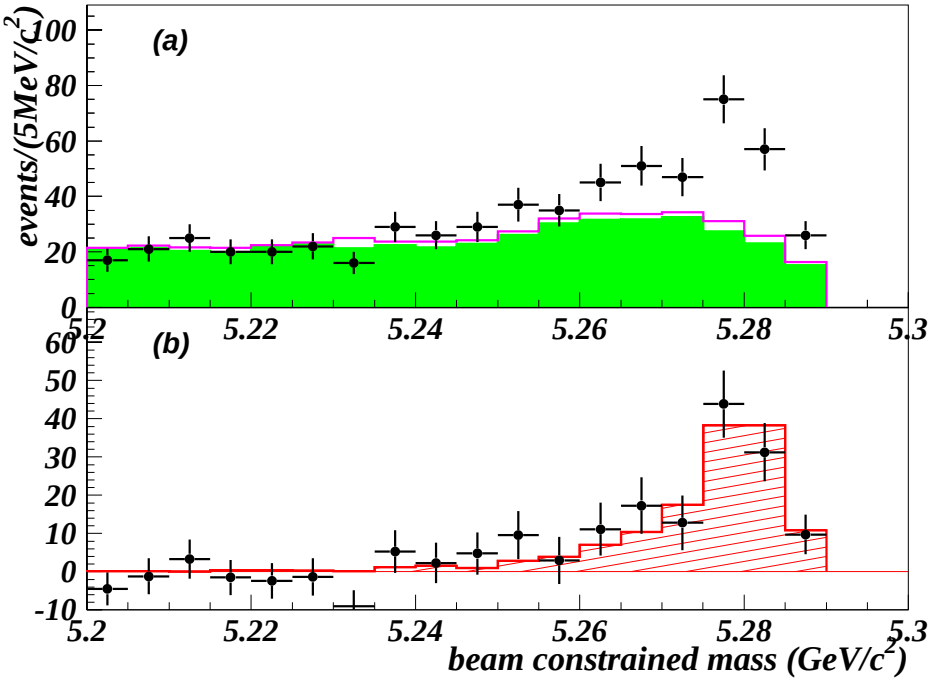

Figure 4.7: Subtraction and fit result – (a) Observed data (error bars) compared to SFW sideband background data (solid histogram) and $B\bar{B}$ MC (open histogram). (b) subtracted signal (error bars) compared to signal MC (hatched histogram).

	notation	yield and error
observed in SFW sideband	$N_{side}^{observed}$	634
observed in signal box	$N_{sig}^{observed}$	222
MC $B\bar{B}$ remaining in signal box	$N_{sig}^{B\bar{B}MC}$	27
$q\bar{q}$ in signal box	$B_{q\bar{q}}$	$N_{side}^{observed} \times r_{q\bar{q}} = 106.4 \pm 7.5$
$B\bar{B}$ in signal box	$B_{B\bar{B}}$	$N_{sig}^{B\bar{B}MC} \times r_{B\bar{B}} = 9.1 \pm 1.8$
background total	B	$B_{q\bar{q}} + B_{B\bar{B}} = 115.5 \pm 7.5$
signal	S	$N_{sig}^{observed} - B = 106.5 \pm 16.7 \pm 5.3$

Table 4.1: Yield in the signal extraction procedure.

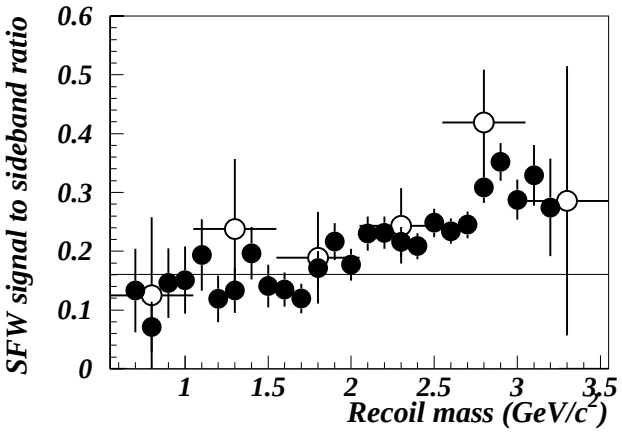

Figure 4.8: X_s mass spectrum in the SFW sideband – The correlation between the SFW and the M_{X_s} is not large upto M_{X_s}= 2.05, but is significant in the whole region. Symbols are defined as in Figure 4.3(c).

followed by a continuum distribution of overlapped higher resonances. We note that our cut $M_{X_s} < 2.05$ is chosen (1) to avoid the blow-up in Figure 4.8 and (2) to reduce $B\bar{B}$ background contribution (See, left plot of Figure 4.9).

4.3.1 Determination of Exclusive $K^*(892)$ to Inclusive X_s Ratio r_{mix}

In the bottom plot of Figure 4.9, we count the number of the signal yield in $M_{X_s} < 1.15$ GeV/c^2 region and in $1.15 < M_{X_s} < 2.05$ GeV/c^2 region, respectively. Their ratio (r_{mix}) is calculated to be 0.30 ± 0.09. Once we obtain the r_{mix}, we model the recoil mass spectrum for $B \to X_s\gamma$ so that the model reproduces the observed r_{mix}; we will discuss concretely about the way of modeling in section 5.1. That means we have a new signal MC sample and we have to iterate the fitting procedure of the beam constrained mass spectrum using the new signal MC. [3] The r_{mix} is found to be stable to the iterations.

4.4 Checks for observed data

In the following subsections, we check some of the important spectra in this analysis. Although these do not have direct impacts on the final result of the branching fraction, we can, by checking these spectra, confirm that we are not astray.

4.4.1 Photon energy spectrum

The photon energy also has a significant correlation with SFW. Again, for the photon energy spectrum, we use $q\bar{q}$ MC to subtract, which is normalized by the number of events obtained

[3] This sounds as the matter of "egg first or hen first". In reality, the first model is built with CLEO's number.

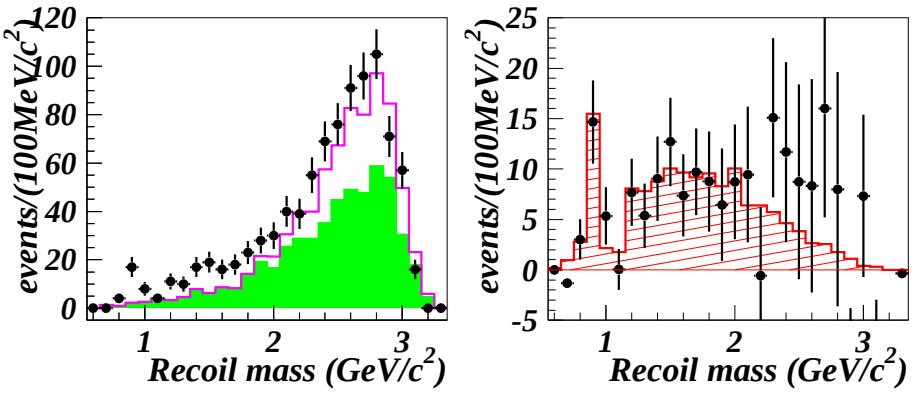

Figure 4.9: X_s mass distribution for data. Symbols are defined as in Figure 4.7.

as in Table 4.1.

Figure 4.10 shows the extracted photon energy spectrum. The low energy side of the photon spectrum is distorted by the M_{X_s} cut as shown in Figure 4.11. A Cut on M_{X_s} does not appear as a sharp cut-off in E_γ, but as a suppression in a broad region. This is because the beam constrained mass and ΔE have a finite widths, and also because of the finite momentum of B meson in the $\Upsilon(4S)$ rest frame. Correcting the distorting effect by MC (the left plot of Figure 4.11), the population in the low energy side increases and the photon energy spectrum looks as shown in Figure 4.12. In the high energy side, where the monochromatic photon of $B \to K^*(892)\gamma$ mainly contributes, we have less m_b dependence.

4.4.2 Pion multiplicity

We also checked the pion multiplicity for data. From the extracted population shown in Figure 4.13(c), $K^*(892)\gamma$ exclusive sample may be overpopulated in our signal MC, since the bin for one pion has a bit larger population than data. But it is still within the statistical fluctuation, and we persist in our MC add-up-ratio discussed in section 4.3.1. Agreement in Figure 4.13(c) demonstrates that the JETSET hadronization is reliable at this moment.

4.4.3 Angular distribution of the photon

The photons should be smoothly distributed throughout the detector acceptance. A "hot spot" might be due to an anomaly of the detector. The angular distribution of the photon is checked for the observed events (signal + background). There is no single hot channel in either θ or ϕ distribution. We note that the bin size is chosen to be approximately equal to the crystal size.

4.4.4 Yield for each dataset

The data used in this analysis were collected over more than half a year. As shown in Table 3.1, the software library was upgraded several times during the period. If an unusually

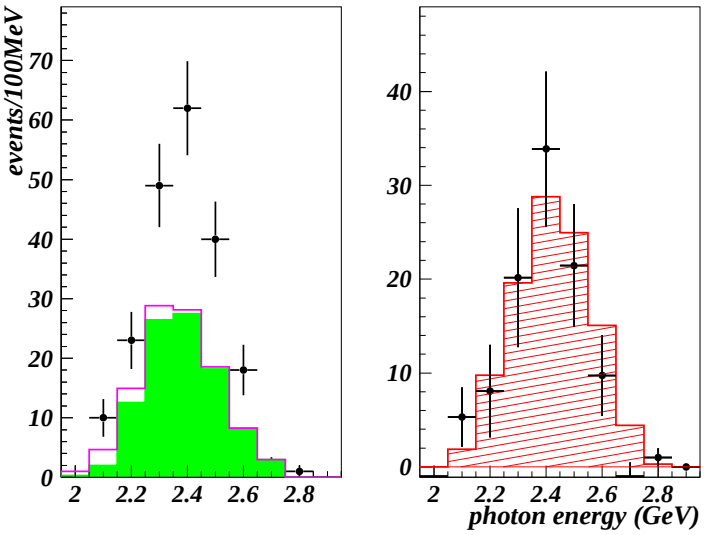

Figure 4.10: Photon energy spectrum for data. Symbols are defined as in Figure 4.7.

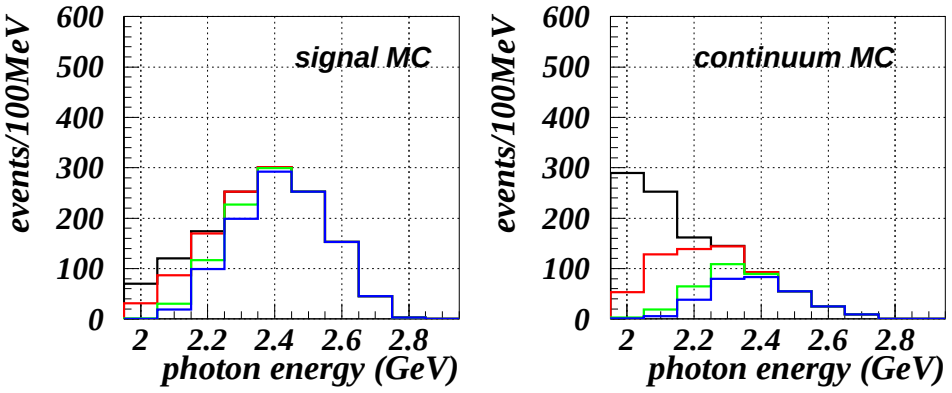

Figure 4.11: Photon energy spectrum with various cut on M_{X_s} – Cut values are, from outer to inner, 3.5, 2.45, 2.15, 1.85 in GeV/c^2. [Left] signal MC [Right] $q\bar{q}$ MC.

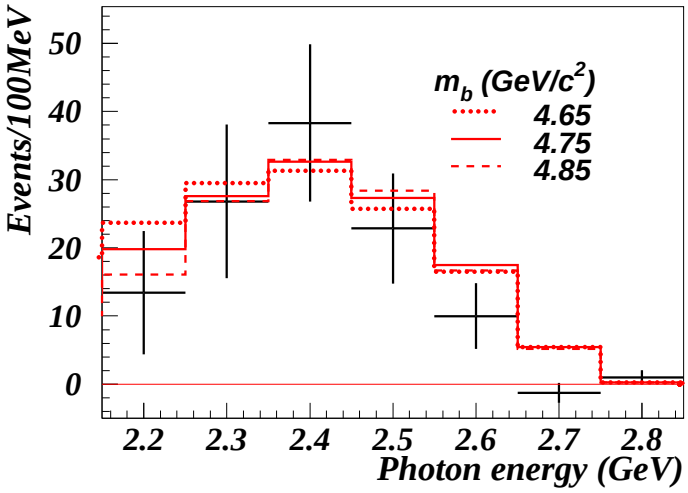

Figure 4.12: Photon energy spectrum corrected for the distortion effect by M_{X_s} cut. Data points (error bars) are compared with the models of the three m_b parameter values (histograms).

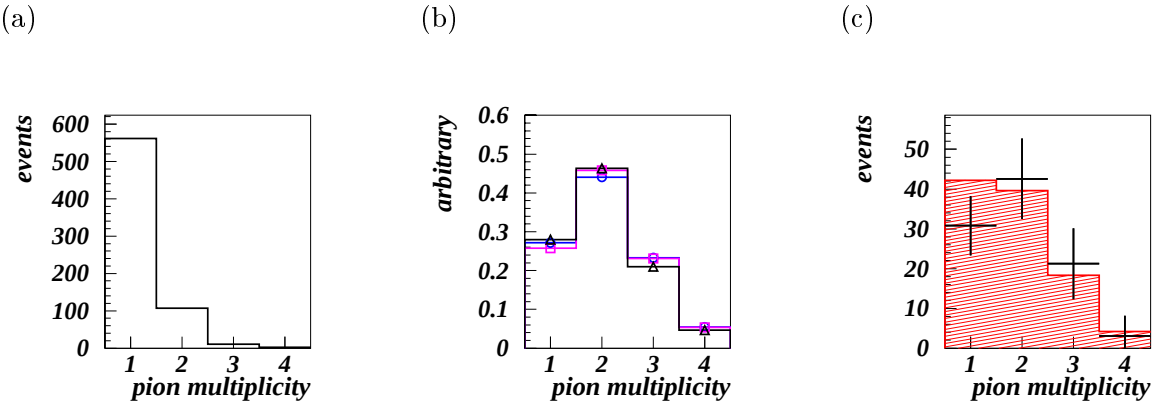

Figure 4.13: Pion multiplicity for $K^*(892)\gamma$ MC (a), inclusive sample for $M_{X_s} > 1.15\,\mathrm{GeV/c^2}$ (b), and extracted signal (c). In (b), population is similar for $m_b = 4.65\,\mathrm{GeV/c^2}$ (circles), $m_b = 4.75\,\mathrm{GeV/c^2}$ (squares) and $m_b = 4.85\,\mathrm{GeV/c^2}$ (triangles).

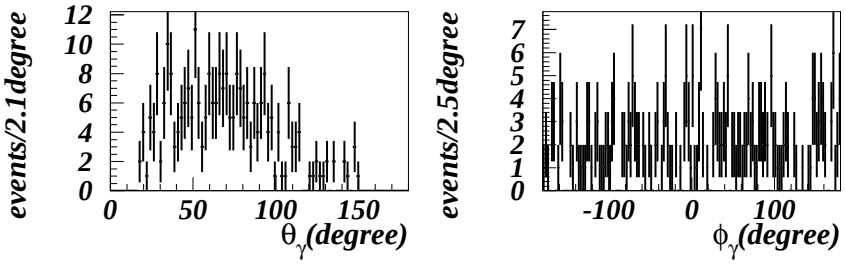

Figure 4.14: Angular distribution of the photon

Period	Integrated Luminosity (fb^{-1})	Yield			Yield/fb^{-1}
		$N_{sig}^{observed}$	$N_{side}^{observed}$	S	
a (6-1320)	2.21	74	208	35.6	16.1
b (1321-1996)	1.88	81	225	40.3	21.4
c (1997-2865)	1.75	67	201	30.5	17.4

Table 4.2: Yield summary for different run period

large fraction of the signal yield is contained in a specific run period, then we must suspect the result.

We divide the data into three periods : (a) run 6 to 1320 [$2.2\,\mathrm{fb}^{-1}$], (b) run 1321 to 1996 [$1.9\,\mathrm{fb}^{-1}$] and (c) run 1997 to 2865 [$1.7\,\mathrm{fb}^{-1}$]. The observed beam constrained mass spectrum in these three run periods are shown in Figure 4.15.

We estimated the signal yield for each run period as summarized in Table 4.2. We used the scaling factor $r_{q\bar{q}}$ obtained from the full dataset in section 4.2 commonly in each run period.

There are no significant run dependency either in spectra or in the signal yield.

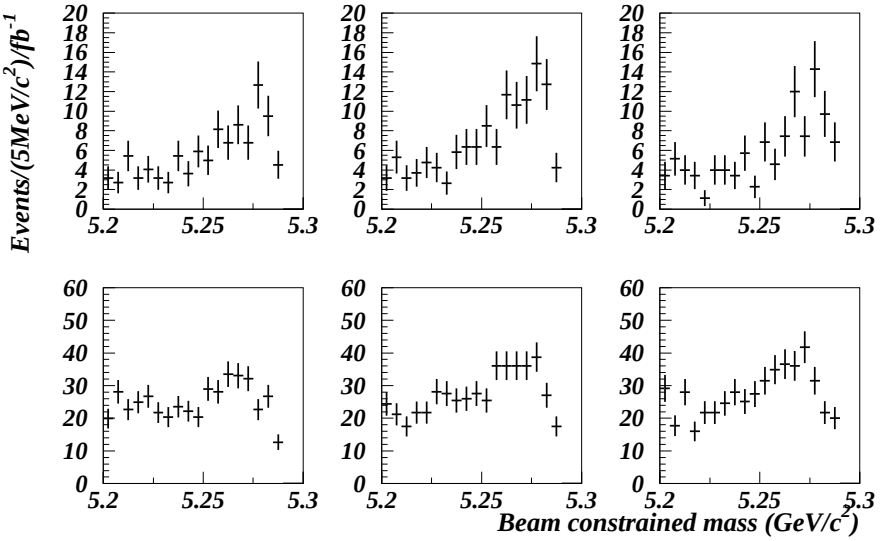

Figure 4.15: Beam constrained mass spectrum for the three run periods (a), (b) and (c) from left to right. Top histograms are in the signal regin and the bottom histograms are in the SFW sideband. Histograms are normalized by each integrated luminosity.

Chapter 5

Signal reconstruction efficiency

5.1 Modeling the $B \to X_s\gamma$

We obtained the value of r_{mix} in section 4.3.1. Now we can explain how we modeled our signal MC. First, we have generated samples of $K^*(892)\gamma$ and $X_s\gamma$ separately. Each contains $N_{K^*} \sim 10\,\mathrm{K}$ and $N_{X_s} \sim 34\,\mathrm{K}$ events, respectively. Figure 5.1 shows how the two samples are reconstructed in two M_{X_s} regions; $M_{X_s} < 1.15$ GeV/c^2 and $1.15 < M_{X_s} < 2.05$ GeV/c^2. Among N_{K^*} of $K^*(892)\gamma$ events, 548 events are reconstructed in $M_{X_s} < 1.15$ GeV/c^2 and 133 events are reconstructed in $1.15 < M_{X_s} < 2.05$ GeV/c^2. Similarly for $X_s\gamma$, 17 events in $M_{X_s} < 1.15$ GeV/c^{2}and 767 in $1.15 < M_{X_s} < 2.05$ GeV/c^2. Let's denote these four numbers as L_{K^*}, H_{K^*}, L_{X_s} and H_{X_s}, for simplicity. Suppose we mix the whole sample of the $X_s\gamma$ and a part (factor α) of $K^*(892)\gamma$ sample, we expect that $(\alpha \times L_{K^*} + L_{X_s})$ events will be reconstructed in $M_{X_s} < 1.15$ GeV/c^2 region and $(\alpha \times H_{K^*} + H_{X_s})$ events in $1.15 < M_{X_s} < 2.05$ GeV/c^2. Once we have obtained r_{mix}, α can be calculated by a simple mathematics, namely,

$$r_{mix} = \frac{\alpha L_{K^*} + L_{X_s}}{\alpha H_{K^*} + H_{X_s}} \tag{5.1}$$

$$\alpha = \frac{r_{mix} H_{X_s} - L_{X_s}}{L_{K^*} - r_{mix} H_{K^*}} \tag{5.2}$$

$$= 0.4257. \tag{5.3}$$

Going one step ahead, we can deduce the signal reconstruction efficiency (ϵ_{MC}) from the above information again by a simple mathematics.

$$\epsilon_{MC} = \frac{\alpha(L_{K^*} + H_{K^*}) + (L_{X_s} + H_{X_s})}{\alpha N_{K^*} + N_{X_s}} \tag{5.4}$$

The inclusive sample of the X_s intermediate state was generated as an equal mixture of $s\bar{d}$ and $s\bar{u}$ quark pairs to follow the recoil mass spectrum of the Kagan-Neubert model [38]. We take the parameter $m_b = 4.75\,\mathrm{GeV/c^2}$ for our central model. Hadronization of the X_s intermediate state is done by JETSET [39]. Mixing it with the exclusive $K^*(892)\gamma$ sample in the ratio N_{X_s} to αN_{K^*}, our model for recoil mass looks as shown in Figure 5.2; and the center value of signal reconstruction efficiency is calculated from MC results to be

$$\epsilon_{MC} = 2.84\%.$$

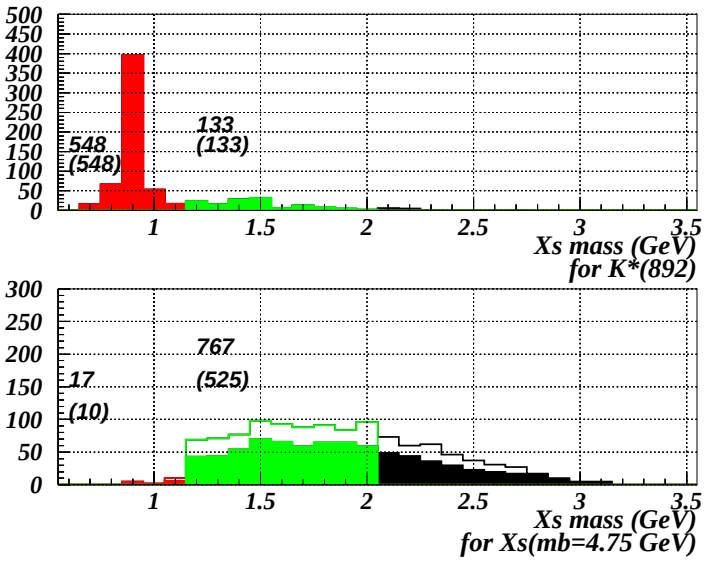

Figure 5.1: Reconstructed X_s mass spectrum for exclusive $K^*(892)\gamma$ MC and inclusive $X_s\gamma$ – The number represents the events reconstructed in each region. Numbers in parentheses and solid histogram are for those generated in M_{X_s}<2.05 region. Typically, 77% of the events reconstructed below 2.05 GeV/c^2 are genuine and the rest are from the region above 2.05 GeV/c^2.

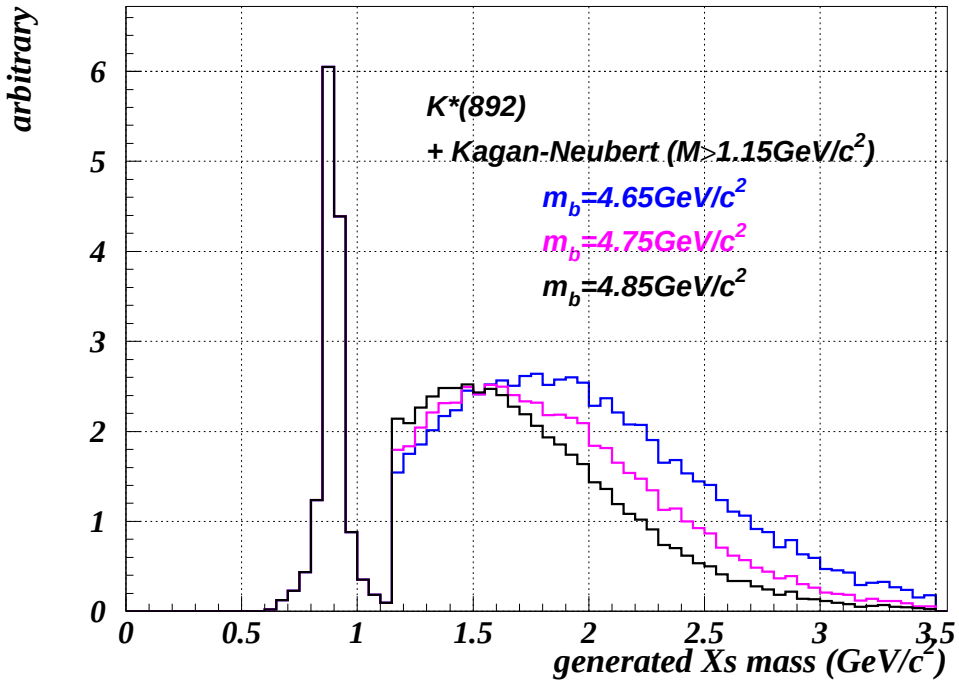

Figure 5.2: Generated recoil mass spectrum based upon Kagan-Neubert model with various parameters. Lower m_b tends to yield higher M_{X_s}.

Figure 5.2 shows the theoretical uncertainty in the recoil mass prediction. We have generated another two sets of signal MC in the same procedure for two parameter values ($m_b = 4.65$, $4.85\mathrm{GeV/c^2}$). In each case, the mixture ratio of exclusive $K^*(892)$ to inclusive X_s is fixed to $r_{mix} = 0.30$.

Figure 5.3 shows the reconstructed X_s mass distributions for these two samples, which is to be compared to Figure 5.1. The reconstruction efficiency for signal is calculated as in equation 5.4 and are summarized in Table 5.1 in comparison to the central case ($m_b = 4.75\mathrm{GeV/c^2}$).

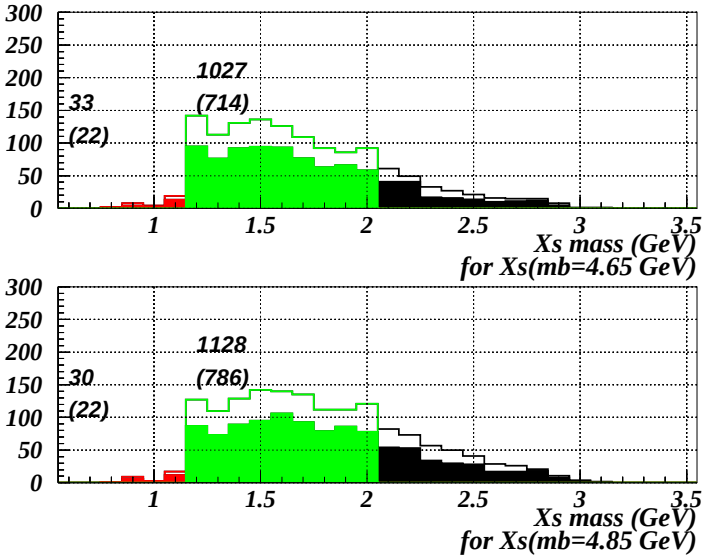

Figure 5.3: Reconstructed X_s mass spectrum for MC $B \to X_s\gamma$ with $m_b = 4.65\mathrm{GeV/c^2}$ and $m_b = 4.85\mathrm{GeV/c^2}$. Numbers and histograms are defined as in Figure 5.1.

Here, the error on the efficiency is propagated only from the error on r_{mix}. Errors on L_{K^*}, H_{K^*}, L_{X_s} and H_{X_s} are the statistical error of MC sample which are taken into the systematic error in section 5.2.8.

We get different signal efficiencies for different m_b parameter values. The efficiency numbers for $m_b = 4.65(4.85)$ GeV/c^2 is 13.8% lower (15.4% higher) than the central efficiency. Combining the error from theoretical model difference and the error from r_{mix}, we quote $^{+15.0\%}_{-16.1\%}$ error on the signal efficiency as the theoretical error[1].

We note that $m_b = 4.80 \pm 0.15\,\mathrm{GeV/c^2}$ is suggested in the reference [38]. We use $m_b = 4.75 \pm 0.10\,\mathrm{GeV/c^2}$. The parameter range of $\pm 0.10\,\mathrm{GeV/c^2}$ is suggested in a private communication with A. Ali, who has suggested the same range to CLEO. The central value is lowered because $mb \geq 4.90\,\mathrm{GeV/c^2}$ is disfavored as we will see in section 6.2.

[1]We also tested some of JETSET parameters which determine the characteristics of hadronization. We found they only have negligible effects on the signal reconstruction efficiency.

	$K^*(892)$		
N_{K^*}	9999		
L_{K^*}	548		
H_{K^*}	133		
	continuum X_s		
	m_b=4.65GeV/c^2	m_b=4.75GeV/c^2	m_b=4.85GeV/c^2
N_{X_s}	31370	33556	41986
L_{X_s}	19	17	30
H_{X_s}	607	767	1128
α	0.3259	0.4257	0.6162
ϵ	(2.45± 0.15)%	(2.84± 0.15)%	(3.28± 0.16)%
$\Delta\epsilon/\epsilon$	5.9%	5.4%	4.8%

Table 5.1: Generated and reconstructed numbers of events and efficiencies for signal MC samples.

5.2 Systematics correction

In this section, we test the efficiencies obtained from MC with high statistics control data samples. We assume that our MC describes our detector and storage ring well and only needs a correction for real data. We define our signal reconstruction efficiency as follows.

$$\epsilon_{data} = \epsilon_{MC} \times f_c = \epsilon_{MC} \times \frac{\epsilon_{data}^{best\ selection}}{\epsilon_{MC}^{best\ selection}} \times \frac{\epsilon_{data}^{SFW,\ \pi^0/\eta\ veto}}{\epsilon_{MC}^{SFW,\ \pi^0/\eta\ veto}} \times \frac{\epsilon_{data}^{tracking}}{\epsilon_{MC}^{tracking}} \times \frac{\epsilon_{data}^{photon}}{\epsilon_{MC}^{photon}} \times \frac{\epsilon_{data}^{PID}}{\epsilon_{MC}^{PID}} \tag{5.5}$$

We suppose that the associated errors are uncorrelated, and define the systematic error on the signal reconstruction efficiency as follows.

$$\frac{\delta\epsilon}{\epsilon} = \frac{\delta\epsilon^{best\ selection}}{\epsilon^{best\ selection}} \oplus \frac{\delta\epsilon^{SFW,\ \pi^0/\eta\ veto}}{\epsilon^{SFW,\ \pi^0/\eta\ veto}} \oplus \frac{\delta\epsilon^{tracking}}{\epsilon^{tracking}} \oplus \frac{\delta\epsilon^{photon}}{\epsilon^{photon}} \oplus \frac{\delta\epsilon^{PID}}{\epsilon^{PID}} \oplus \frac{\delta\epsilon_{MC}^{stat}}{\epsilon_{MC}} \tag{5.6}$$

Namely, we use ϵ_{data} for the branching fraction determination; and since we know it only with the precision of $\delta\epsilon$, we quote it as the systematic error.

As stated earlier, we use 16 different reconstruction modes in this analysis, so the breakdowns of efficiencies are different mode by mode. Equation 5.6, therefore, can be broken down

as follows.

$$\begin{aligned}
\epsilon_{data}^{0101} &= \epsilon_{MC}^{0101} S_{common} S_T^2 S_{\pi^\pm} S_{K^\pm} \\
\epsilon_{data}^{0201} &= \epsilon_{MC}^{0201} S_{common} S_T^3 S_{\pi^\pm}^2 S_{K^\pm} \\
\epsilon_{data}^{0301} &= \epsilon_{MC}^{0301} S_{common} S_T^4 S_{\pi^\pm}^3 S_{K^\pm} \\
\epsilon_{data}^{0401} &= \epsilon_{MC}^{0401} S_{common} S_T^5 S_{\pi^\pm}^4 S_{K^\pm} \\
\epsilon_{data}^{1001} &= \epsilon_{MC}^{1001} S_{common} S_T S_{\pi^0} S_{K^\pm} \\
\epsilon_{data}^{1101} &= \epsilon_{MC}^{1101} S_{common} S_T^2 S_{\pi^0} S_{\pi^\pm} S_{K^\pm} \\
\epsilon_{data}^{1201} &= \epsilon_{MC}^{1201} S_{common} S_T^3 S_{\pi^0} S_{\pi^\pm}^2 S_{K^\pm} \\
\epsilon_{data}^{1301} &= \epsilon_{MC}^{1301} S_{common} S_T^4 S_{\pi^0} S_{\pi^\pm}^3 S_{K^\pm} \\
\epsilon_{data}^{0110} &= \epsilon_{MC}^{0110} S_{common} S_T S_{\pi^\pm} S_{K_S} \\
\epsilon_{data}^{0210} &= \epsilon_{MC}^{0210} S_{common} S_T^2 S_{\pi^\pm}^2 S_{K_S} \\
\epsilon_{data}^{0310} &= \epsilon_{MC}^{0310} S_{common} S_T^3 S_{\pi^\pm}^3 S_{K_S} \\
\epsilon_{data}^{0410} &= \epsilon_{MC}^{0410} S_{common} S_T^4 S_{\pi^\pm}^4 S_{K_S} \\
\epsilon_{data}^{1010} &= \epsilon_{MC}^{1010} S_{common} S_{\pi^0} S_{K_S} \\
\epsilon_{data}^{1110} &= \epsilon_{MC}^{1110} S_{common} S_T S_{\pi^0} S_{\pi^\pm} S_{K_S} \\
\epsilon_{data}^{1210} &= \epsilon_{MC}^{1210} S_{common} S_T^2 S_{\pi^0} S_{\pi^\pm}^2 S_{K_S} \\
\epsilon_{data}^{1310} &= \epsilon_{MC}^{1310} S_{common} S_T^3 S_{\pi^0} S_{\pi^\pm}^3 S_{K_S}
\end{aligned} \tag{5.7}$$

where,

$$\begin{aligned}
S_{common} &= \frac{\epsilon_{data}^{best\ selection}}{\epsilon_{MC}^{best\ selection}} \times \frac{\epsilon_{data}^{SFW,\ \pi^0/\eta\ veto}}{\epsilon_{MC}^{SFW,\ \pi^0/\eta\ veto}} \times \frac{\epsilon_{data}^{\gamma}}{\epsilon_{MC}^{\gamma}} \\
S_T &= \frac{\epsilon_{data}^{tracking}}{\epsilon_{MC}^{tracking}} \\
S_{\pi^\pm} &= \frac{\epsilon_{data}^{PID(\pi^\pm)}}{\epsilon_{MC}^{PID(\pi^\pm)}} \\
S_{\pi^0} &= \frac{\epsilon_{data}^{PID(\pi^0)}}{\epsilon_{MC}^{PID(\pi^0)}} \\
S_{K^\pm} &= \frac{\epsilon_{data}^{PID(K^\pm)}}{\epsilon_{MC}^{PID(K^\pm)}} \\
S_{K_S} &= \frac{\epsilon_{data}^{PID(K_S)}}{\epsilon_{MC}^{PID(K_S)}}
\end{aligned} \tag{5.8}$$

These 16 terms are correlated each other. The overall systematic error on the signal reconstruction efficiency is estimated by summing up the 16 terms with proper weights which are given in Table 3.3, and fluctuating the factor S one by one within its error while other factors are fixed.

In the following subsections, we test each efficiency factor with a proper control sample, compare the efficiency for MC and data, and obtain the factor S. We summarize the results finally in section 5.2.8.

5.2.1 Photon

The photon efficiency is obtained from a study of the radiative Bhabha events ($e^+e^- \to e^+e^-\gamma$) and the $\eta \to \gamma\gamma$ decay. The study of $e^+e^- \to e^+e^-\gamma$ is complicated due to difficulties in the electron reconstruction compared to photon reconstruction and the fact that we can not perfectly seperate $e^+e^- \to e^+e^-\gamma$ from $e^+e^- \to e^+e^-\gamma\gamma$ where one of the photons is not detected.

To understand the efficiency we divide its source into 5 contributions. Firstly we assume some of the photons are mis-reconstructed in a wrong position, mostly due to the pair-production at the material of inner detectors. Secondly if the energy leakage from the crystal is very large, we mis-reconstruct the energy. Thirdly there is a small chance that we loose the photon completely, possibly through a gap. Fourthly there is a small chance that we loose some photons if a charged track is found nearby. Finally, we loose photons by the E9/E25 cut. We multiply the five effects (we call them angle efficiency, energy efficiency, escaping deficiency, matching efficiency and E9/E25 efficiency) to obtain the photon detection efficiency.

The first two efficiencies are obtained from the radiative Bhabha study by defining ΔE_γ, $\Delta\theta_\gamma$, $\Delta\phi_\gamma$ as the deviation of the reconstructed photon cluster from that expected from e^+ and e^- (Figure 5.4). From the QED skim file and the radiative Bhabha MC, we select the events that have an e^+ track and e^- track in the barrel CsI region ($33^\circ < \theta < 132^\circ$). We require the vertex displacement to be within 5 mm in z and 2mm in r from the IP. The total energy deposit is required to be greater than 11 GeV. Then we form the expected photon momentum from momenta of e^+ and e^- tracks and the beam energy, and require that the expected photon have 2-3 GeV $\Upsilon(4S)$ rest frame energy in the barrel CsI and outside a 10° cone of either track.

The angle efficiency is estimated from a subset of the above sample that has $|\Delta E_\gamma| < 40$ MeV, to further suppress the $e^+e^- \to e^+e^-\gamma\gamma$ effect. We checked the angle distribution and counted the fraction of events that fall in 3σ of the peak. Here we use ϕ distribution in which the initial state radiation into the beampipe has little effect (middle plots of the Figure 5.4).

Similarly, we restrict the photon direction to be within 2σ of the $\Delta\theta_\gamma$ and $\Delta\phi_\gamma$ and count the number of events inside a $-0.2 < \Delta E_\gamma < 0.1$ window (right plots of the Figure 5.4). We noticed that the angle efficiency is much smaller than MC true efficiency (about 90%). This can be explained as the efficiency loss by the electron side, and it is somewhat consistent with the electron efficiency given by a photon conversion study [40].

The escaping deficiency is hard to determine from the data, but from our MC study we found $1.9 \pm 0.6\%$. We assume 100% error on this deficinecy for the real data deficiency. Here we defined the photon to be escaped when the MC true photon of 2-3 GeV $\Upsilon(4S)$ rest frame energy is in the barrel and $e^+\,e^-$ tracks are well reconstructed, yet we found that the total invisible energy is more than 1 GeV.

We also tested the matching efficiency using the embedded MC single photon into data. We observe about a 1% loss, and we take this as the maximum uncertainty since it is a very small loss.

The E9/E25 efficiency is tested with an $\eta \to \gamma\gamma$ sample. For an energetic photon from η decay with energy in $\Upsilon(4S)$ rest frame greater than 2 GeV, we apply the E9/E25 cut and we compared the yields before and after the cut for both MC and data. The yield is extracted by fitting the peak with a Crystal Ball line shape [2] plus a thrid polynomial as shown in Figure 5.5.

[2] This function uses the NaI line shape as obtained by the Crystal Ball experiment [41].

The results are summarized in Table 5.2, in which we see the data and MC efficiency is consistent within the error.

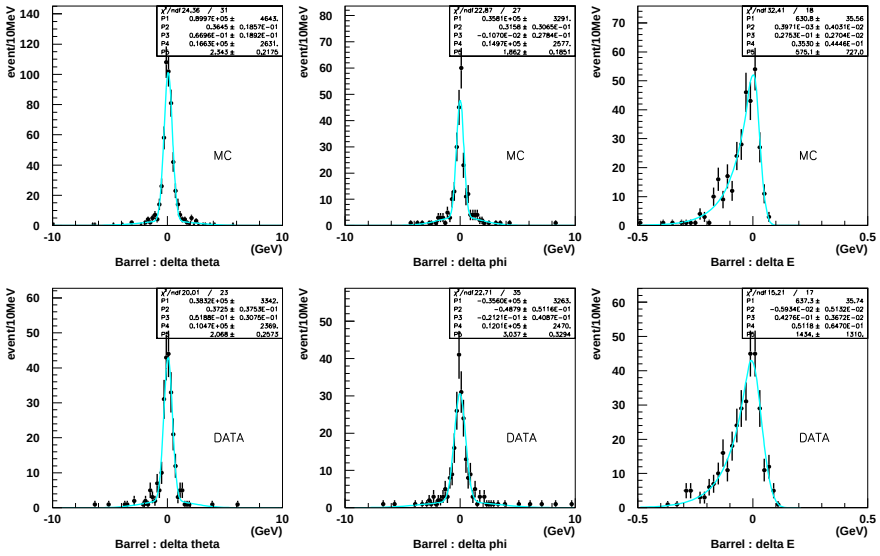

Figure 5.4: Raidative Bhabha Scattering Study – $\Delta\theta_\gamma$ (left) $\Delta\phi_\gamma$ (middle) and ΔE_γ (right) distribution for the radiative Bhabha MC(top) and data(bottom). The shape is fitted with a double-gaussian ($\Delta\theta_\gamma$, $\Delta\phi_\gamma$) and the Crystal Ball line shape (ΔE_γ)

	MC	Data
angle eff.	80.2 ± 2.5	80.9 ± 2.5
energy eff.	95.3 ± 1.2	94.0 ± 1.3
escaping def.	1.9 ± 0.6	1.9 ± 1.9
matching eff.	(99.0)	99.0 ± 1.0
E9/E25 eff.	93.7 ± 0.1	94.9 ± 0.1
combined eff.(%)	69.6 ± 2.4	70.1 ± 2.8
ratio	–	1.007 ± 0.053

Table 5.2: Summary of photon detection efficiency from radiative Bhabha decays

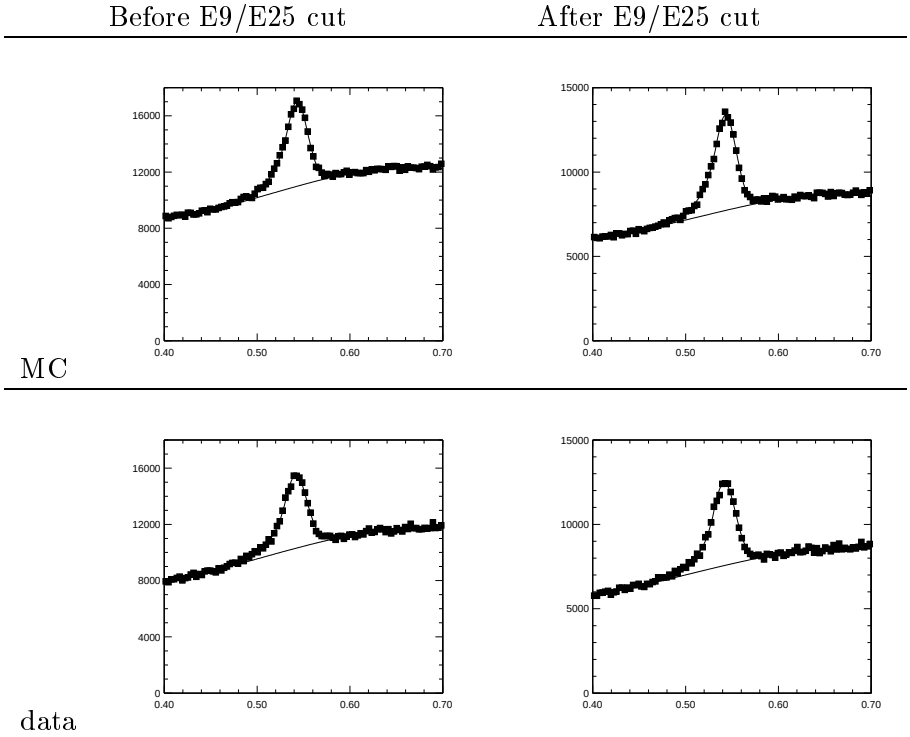

Figure 5.5: $\eta \to \gamma\gamma$ study for E9/E25 cut efficiency – before (left) and after (right) E9/E25 cut for continuum MC [Top] and data [Bottom]. Holizontal axes are for the invariant mass for the two photons ($M_\gamma\gamma$) in GeV/c^2. Virtical axes are for the number of events per 3 MeV/c^2. Fitting functions are Crystal Ball line shape and the third polynomial.

5.2.2 Tracking

We check the tracking efficiency from $\eta \to \pi^+\pi^-\pi^0$ and $\eta \to \gamma\gamma$ decays. The branching ratio of these two decays are precisely known and almost correctly implemented in the MC generator. Assuming the systematic difference in the photon detection cancels out by taking the ratio, we obtain the relative tracking efficiency difference by

$$\frac{\epsilon_{data}(\pi^+\pi^-)}{\epsilon_{MC}(\pi^+\pi^-)} = \frac{N_{data}(\eta \to \pi^+\pi^-\pi^0)/N_{data}(\eta \to \gamma\gamma)}{N_{MC}(\eta \to \pi^+\pi^-\pi^0)/N_{MC}(\eta \to \gamma\gamma)} \tag{5.9}$$

where N denotes the number of signal yield and ϵ denotes the two track reconstruction efficiency.

The procedure to obtain the yield N is as follows. First, the η candidate is selected with $p_{CM}(\eta) > 2.2\,\mathrm{GeV/c}$ in each channel for continuum MC and data. The photon energy is required to be greater than 100 MeV. The charged track momentum range is selected to match the signal distribution.

Then in MC, the true η is selected to fit the signal and background shapes seperately. The background shape is fitted with a second order polynomial in both channels. The signal shape is a Crystal Ball line shape for $\eta \to \gamma\gamma$ and a gaussian for $\eta \to \pi^+\pi^-\pi^0$ decays. Finally the data is fitted with the fixed signal and background shape, with the normalization and the signal peak position as free parameters. The distribution is shown in Figure 5.6.

Unwillingly, the η branching fractions in the generic `decay.dec` are slightly different from the PDG values. The $\mathcal{B}(\eta \to \gamma\gamma)$ is lower (38.8% from $(39.21 \pm 0.24)\%$), $\mathcal{B}(\eta \to \pi^+\pi^-\pi^0)$ is higher (23.6% from $(23.1 \pm 0.5)\%$). Therefore the double ratio is corrected by a factor of 1.032 ± 0.023 (1.016 ± 0.012 for the single track efficiency).

Possible systematics in the photon reconstruction are checked by changing the photon selection criteria. We redo the fitting procedure by changing the photon energy cut from 100 MeV to 200 MeV and by restricting the photon in the barrel region of the CsI. The results, shown in Table 5.3, stay within the fitting error, so we conclude the systematic error from the photon is small.

From these two track results, we take the square root of each obtained result for the single track efficiency ratio and systematic error. The obtained results show slightly smaller tracking efficiency in the real data. We assume the fitting error as the tracking efficiency systematic error.

	p($\pi^+\pi^-$)>2 GeV	p($\pi^+\pi^-$)>3 GeV
$N_{data}(\eta \to \gamma\gamma)/N_{MC}(\eta \to \gamma\gamma)$	1.411 ± 0.011	
$N_{data}(\eta \to \pi^+\pi^-\pi^0)/N_{MC}(\eta \to \pi^+\pi^-\pi^0)$	1.348 ± 0.037	1.405 ± 0.120
$\epsilon_{data}(\pi^+\pi^-)/\epsilon_{MC}(\pi^+\pi^-)$	0.955 ± 0.028	0.996 ± 0.086
raw single tracking efficiency ratio	0.977 ± 0.014	0.998 ± 0.043
systematics 1: $E_\gamma > 200$ MeV	0.980 ± 0.016	0.992 ± 0.044
systematics 2: barrel photon only	0.972 ± 0.015	0.952 ± 0.045
MC branching ratio correction factor	0.986 ± 0.012	
corrected single tracking efficiency ratio	0.991 ± 0.018	1.012 ± 0.045

Table 5.3: Summary of the tracking efficiency ratio study between data and MC using $\eta \to \pi^+\pi^-\pi^0/\eta \to \gamma\gamma$

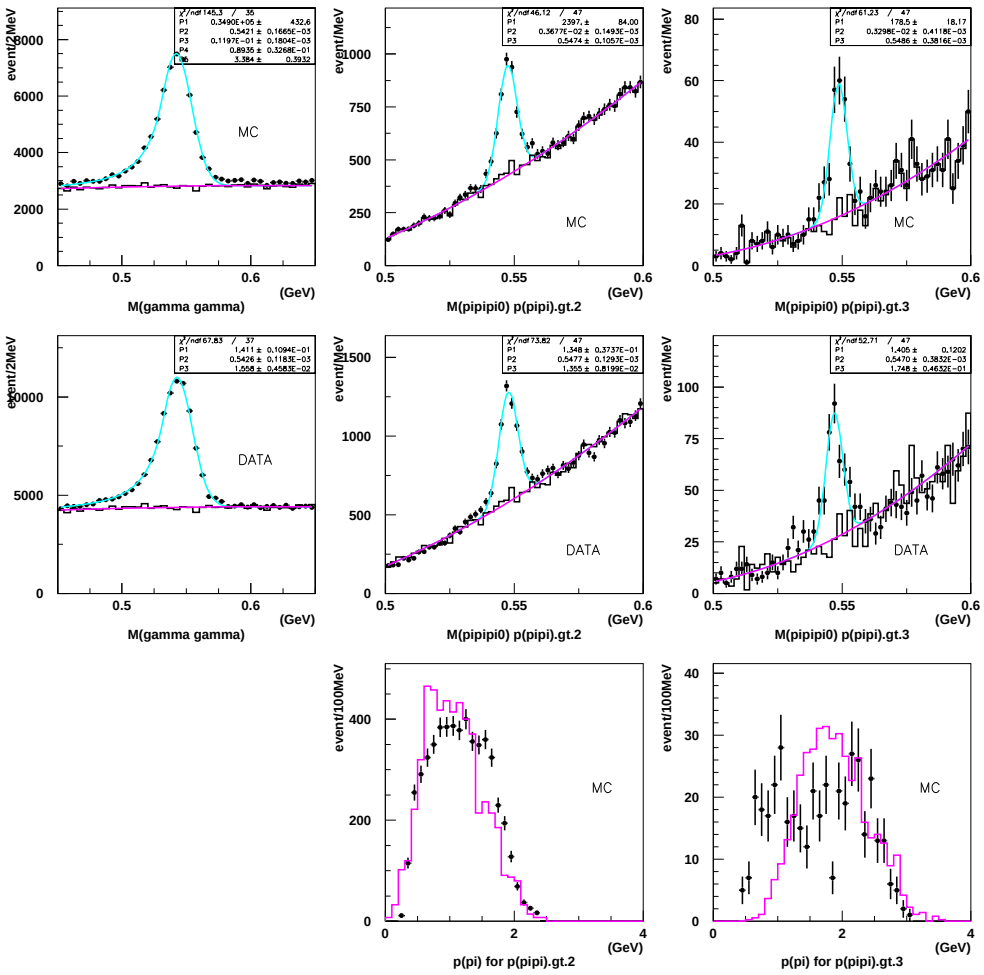

Figure 5.6: Tracking systematics check with $\eta \to \pi^+\pi^-\pi^0/\eta \to \gamma\gamma$. – The left two plots are for the $\eta \to \gamma\gamma$ channel and the middle(right) plots are for $\eta \to \pi^+\pi^-\pi^0$ channel with p($\pi^+\pi^-$)>2(3)GeV/c. The top three plots are MC mass distributions and the middle three plots are data mass distributions. Data points are signal plus background and the histogram is expected background from MC. The error bars of the bottom two plots show the momentum ranges of the track used in the η mass region. The overlaid histogram is the charged track momentum distribution from the $K^*(892)\gamma$ MC for pion(middle) and kaon(right) just to show that we selected the momentum range to match in either case.

5.2.3 $\pi^{\pm}$ ID

We check the charged π identification efficiency from the same $\eta \to \pi^+\pi^-\pi^0$ decay sample that was used in the tracking efficiency estimation. Using the same fitting procedure, we obtain the yield for data and MC with the no PID cut case, for the single track PID case and the both track PID case, as shown in Figure 5.7. By comparing the the ratio, we obtain the absolute PID efficiency and the relative ratio between data and MC as summarized in Table 5.4

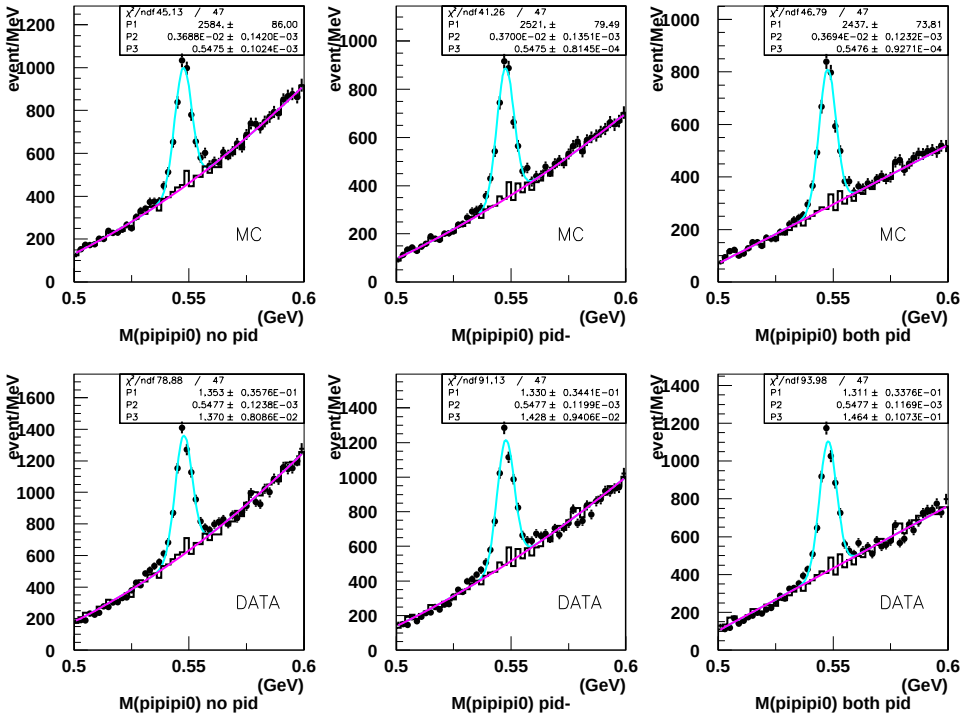

Figure 5.7: Pion identification systematics check with $\eta \to \pi^+\pi^-\pi^0$ – The top plots are MC mass distributions and the middle plots are data mass distributions. From left to right, no PID case, single PID case, both PID case are shown. Data points are signal + background.

		no PID	single PID (+ track)	single PID (− track)	both PID
MC					
	yield	2584 ± 86	2584 ± 80	2521 ± 79	2437 ± 74
	ϵ (ave.)		$(97.8 \pm 0.5)\%$		
Data					
	yield	3496 ± 86	3450 ± 80	3353 ± 79	3195 ± 74
	ϵ (ave.)		$(96.3 \pm 0.7)\%$		
Data/MC ratio			0.985 ± 0.008		

Table 5.4: Summary of the pion indentification efficiency ratio study between data and MC using $\eta \to \pi^+\pi^-\pi^0$decays.

5.2.4 $K^\pm$ ID

To check the kaon identification, we seperate the kaons into two categories; those combined with 1 pion (charged or neutral) and with 2 or more pions. Due to the kinematics, kaons from each of these modes have different momentum spectrum; for the case of $K + 1\pi$ we use $\phi \to K^+K^-$ sample, while for $K+2$, 3 or 4 π we use $D_s^+ \to \phi(\to K^+K^-)\pi^+$ sample, in order to have the similar momentum range in each case.

K^+K^- invariant mass spectra in $\phi \to K^+K^-$ are shown in Figure 5.8. Each spectrum is fitted by Breit-Wigner function[3] plus threshold function[4]. The ϕ yield is checked for MC and data with and without kaon identification cut as summarized in Table 5.5.

		no KID	single KID (+ track)	single KID (− track)	both
MC					
	yield	19618.4 ± 340.9	14100.9 ± 211.1	13981.8 ± 206.7	10783.4 ± 158.2
	ϵ(average)		$(74.14 \pm 0.32)\%$		
Data					
	yield	8716.5 ± 258.0	5212.0 ± 140.0	5188.2 ± 139.7	3135.3 ± 93.3
	ϵ(average)		$(59.97 \pm 0.71)\%$		
	data/MC ratio		0.809 ± 0.010		

Table 5.5: Summary of kaon PID efficiency ratio between data and MC using $\phi \to K^+K^-$

$K^+K^-\pi^+$ invariant mass spectra in $D_s^+ \to \phi(\to K^+K^-)\pi^+$ are shown in Figure 5.9. Each spectrum is fitted by double Gaussian plus first order polynomial. The D_s yield is checked for MC and data with and without kaon identification cut as summarized in Table 5.6.

[3]The Breit-Wigner function is defined with the normalization parameter P_1, the width w and the peak position m as $P_1 \frac{(w/2)^2}{(x-m)^2+(w/2)^2}$.

[4]A threshold function is defined with four free parameters and the threshold x_0 as $P_1(x - x_0)^{P_2} \exp\left(P_3(x-x_0) + P_4(x-x_0)^2\right)$.

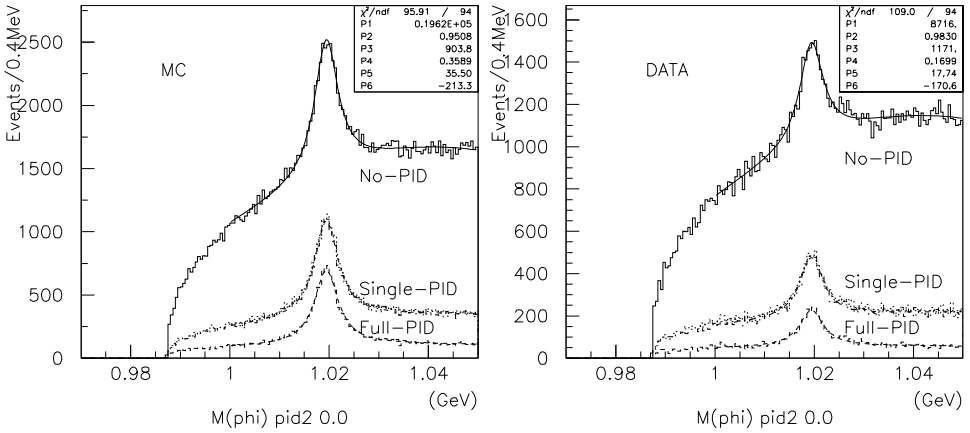

Figure 5.8: Kaon identification systematics check with $\phi \to K^+K^-$ – K^+K^- invariant mass distribution for MC(left) and Data(right) without PID, with single PID, and with double PID.

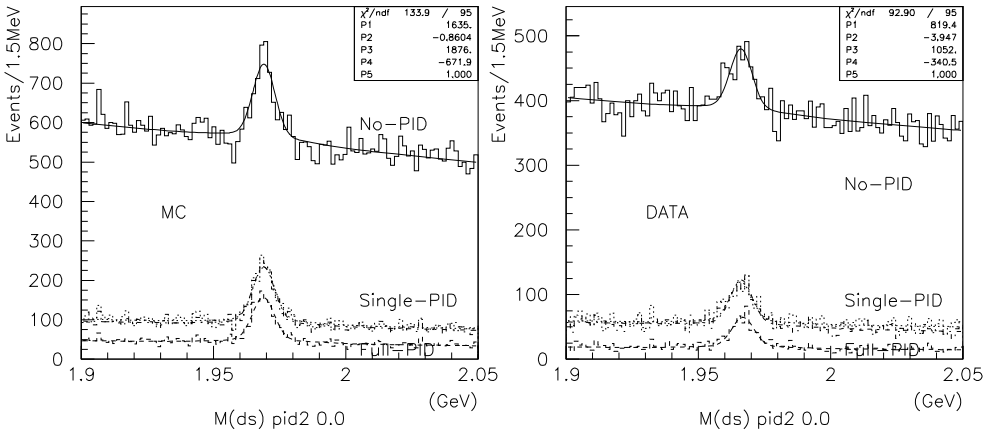

Figure 5.9: Kaon identification systematics check with $D_s^+ \to \phi(\to K^+K^-)\pi^+$ – $K^+K^-\pi^+$ invariant mass distribution for MC(left) and Data(right) without PID, with single PID, and with double PID.

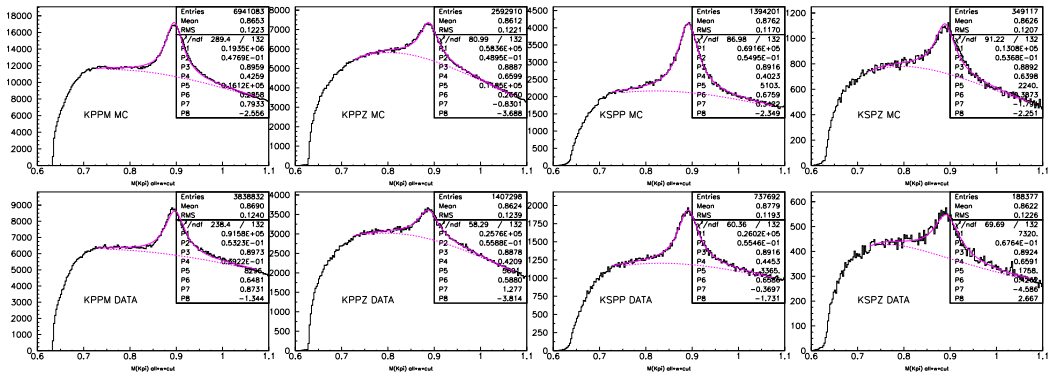

Figure 5.10: K_S and π^0 systematics check with $K^*(892)$ – $K\pi$ invariant mass distribution for MC (top) and Data (bottom), $K^+\pi^-$, $K^+\pi^0$, $K_S\pi^+$, and $K_S\pi^0$ from left to right.

5.2.5 K_s^0 and π^0

We use inclusive $K^*(892)$ sample to check the neutral kaon and pion reconstruction efficiencies. We reconstruct $K^*(892)$ in four modes, $K^+\pi^-$, $K^+\pi^0$, $K_S\pi^+$, and $K_S\pi^0$, and checked the yields. The momentum range is adjusted to our signal. $K\pi$ invariant mass spectra in four modes are shown in Figure 5.10. Each spectrum is fitted by Breit-Wigner function plus threshold function. Obtained yields are summarized in Table 5.7.

The yield is proportional to the efficiency product; for example, $N^{K^+\pi^-} \propto \epsilon^{K^+}\epsilon^{\pi^-}$. There-

		no KID	single KID (+ track)	single KID (− track)	both
MC					
	yield	1642.3 ± 97.6	1201.1 ± 51.9	1245.1 ± 51.7	971.9 ± 41.6
	ϵ(average)		$(76.99 \pm 1.02)\%$		
Data					
	yield	819.0 ± 79.3	537.7 ± 38.2	595.7 ± 38.2	406.3 ± 27.1
	ϵ(average)		$(70.12 \pm 1.78)\%$		
	data/MC ratio		0.911 ± 0.026		

Table 5.6: Summary of kaon PID efficiency ratio between data and MC using $D_s^+ \to \phi(\to K^+K^-)\pi^+$

	$K^+\pi^-$	$K^+\pi^0$	$K_S\pi^+$	$K_S\pi^0$
MC	214740 ± 2339	67929 ± 2930	69821 ± 1514	17308 ± 1391
Data	91578 ± 728	25760 ± 490	26024 ± 347	7320 ± 427

Table 5.7: Summary of $K^*(892)$ yield

fore the double ratio of yields gives the product of efficiency ratios as follows.

$$R_0 = \frac{\left(\frac{N_{data}^{K_S\pi^0}}{N_{MC}^{K_S\pi^0}}\right)}{\left(\frac{N_{data}^{K^+\pi^-}}{N_{MC}^{K^+\pi^-}}\right)} = \frac{\epsilon_{data}^{K_S}}{\epsilon_{MC}^{K_S}}\frac{\epsilon_{data}^{\pi^0}}{\epsilon_{MC}^{\pi^0}}\frac{\epsilon_{MC}^{K^+}}{\epsilon_{data}^{K^+}}\frac{\epsilon_{MC}^{\pi^-}}{\epsilon_{data}^{\pi^-}} \tag{5.10}$$

$$R_+ = \frac{\left(\frac{N_{data}^{K_S\pi^+}}{N_{MC}^{K_S\pi^+}}\right)}{\left(\frac{N_{data}^{K^+\pi^0}}{N_{MC}^{K^+\pi^0}}\right)} = \frac{\epsilon_{data}^{K_S}}{\epsilon_{MC}^{K_S}}\frac{\epsilon_{data}^{\pi^+}}{\epsilon_{MC}^{\pi^+}}\frac{\epsilon_{MC}^{K^+}}{\epsilon_{data}^{K^+}}\frac{\epsilon_{MC}^{\pi^0}}{\epsilon_{data}^{\pi^0}} \tag{5.11}$$

Here we suppose $\frac{\epsilon_{MC}^{K^+}}{\epsilon_{data}^{K^+}} = 1$ and $\frac{\epsilon_{data}^{\pi^+}}{\epsilon_{MC}^{\pi^+}} = 1$, we get

$$\frac{\epsilon_{data}^{K_S}}{\epsilon_{MC}^{K_S}} = \sqrt{R_0 R_+} = 0.987 \pm 0.055 \tag{5.12}$$

$$\frac{\epsilon_{data}^{\pi^0}}{\epsilon_{MC}^{\pi^0}} = \sqrt{R_0 / R_+} = 1.005 \pm 0.057 \tag{5.13}$$

5.2.6 Best candidate selection

Choosing the best candidate itself does not kill any event, but choosing a wrong combination may result the candidate out of the final cut box. To check our best candidate selection, we use $B \to D\pi$ sample. First $\bar{D}^0$ is formed from $K^+\pi^-$, and B^+ is formed from $\bar{D}^0$ and π^+. We require that each of the D mass (M_D), the beam constrained B mass (M_B) and the energy difference (ΔE) is within 3 sigma from what it should be. For these "exclusively tagged" events, we semi-inclusively reconstruct a D meson candidate from 1 K plus 1 to 4 pion(s) as we do in $B \to X_s\gamma$ reconstruction. Treating the primary pion from two body B decay as the primary photon of $B \to X_s\gamma$, we chose the best candidate in the same way; i.e. based upon the vertex of D and the angle between D and the primary pion. Figure 5.11 shows the semi-inclusively reconstructed M_B spectra for $B \to D\pi$ MC and the data. Commonly SFW>-1 cut is applied to remove the most of $q\bar{q}$ background in data. Additionally, M_D, M_B and ΔE are required to be in the 3 sigma window which are defined same as the exclusive tagging. If we do not choose the combination which we reconstructed exclusively beforehand and the chosen combination gives a wrong M_D and/or wrong M_B and/or wrong ΔE, it will be rejected by these cuts. Obtained yields and efficiencies are summarized in Table 5.8.

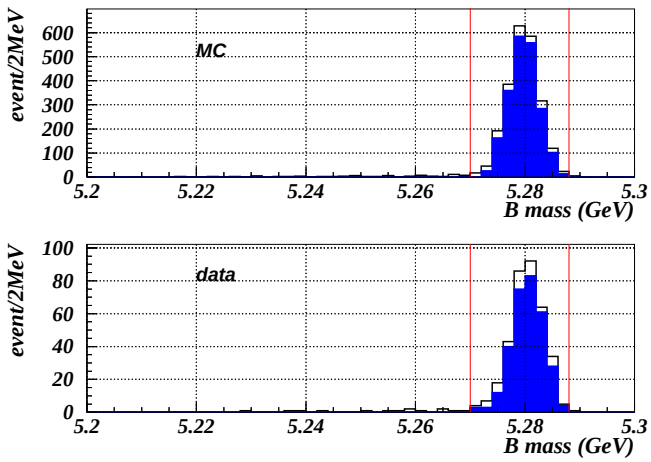

Figure 5.11: Efficiency of best candidate selection – [Top] MC [Bottom] $B \to D\pi$ data (Black) loose SFW cut (Solid Blue Area) after M_B, M_D, ΔE cut

	base cut	inside the tag window	efficiency
Data			
	368	309	83.97 ± 1.91 %
MC			
	2413	2091	86.66 ± 0.69 %
data/MC			0.969 ± 0.023

Table 5.8: best candidate selection systematics summary

5.2.7 SFW and π^0/η veto

The SFW shape for signal MC and data are checked as shown in Figure 3.10. For data, we checked with $B^- \to D^0\pi^-$ and $D^0 \to K^-\pi^+$ mode. The shape agrees within limited statistics.

To estimate the error on the SFW variable and π^0/η veto, we use $B^- \to D^0(K^-\pi^+)\pi^-$ sample. SFW is calculated with the same coefficients listed in Table 3.4, where the primary pion from two body B decay is treated as the primary photon in $B \to X_s\gamma$ case. The π^0/η veto is applied combining the primary pion with a photon candidate.

3 sigma cuts are applied on M_D and ΔE. To subtract background events and extract signal yield from data, we fit the beam constrained mass with ARGUS function plus Gaussian. For MC, the beam constrained mass distribution is fitted by Gaussian alone.

Figure 5.12 shows the fitting result. Signal yield with and without SFW cut (SFW>0.1) and π^0/η veto is summarized in Table 5.9.

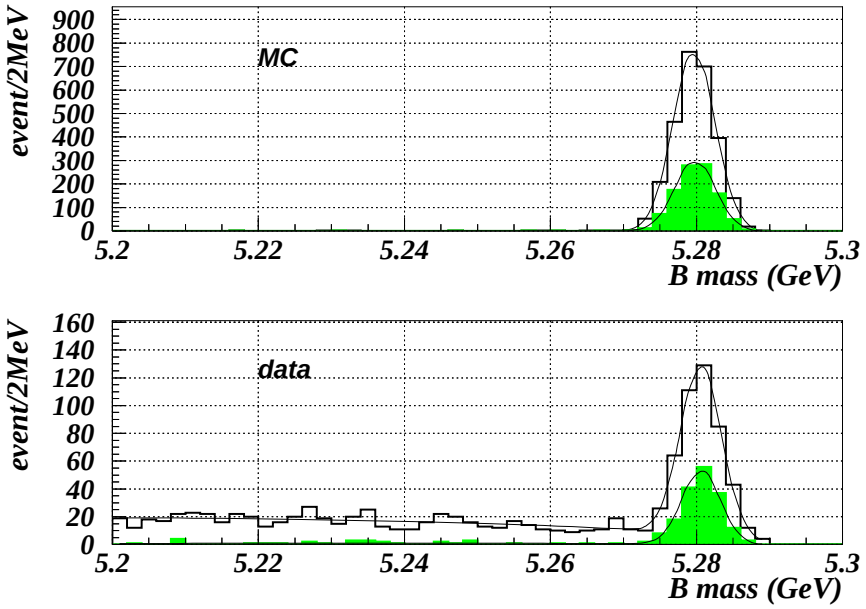

Figure 5.12: SFW and π^0/η veto systematics study with $B \to D\pi$ sample – [Top] MC [Bottom] data. Before SFW cut and π^0/η veto(Black Solid Line) After SFW cut and π^0/η veto(Green Solid Area).

	no cut	SFW>0.1, π^0/η veto	efficiency
Data			
	422.6±22.5	172.7±13.4	40.86 ± 2.57 %
MC			
	2753.4±52.5	1044.1±30.8	37.92 ± 0.91 %
data/MC			1.078 ± 0.073

Table 5.9: SFW systematics summary

5.2.8 Summary of systematic error on signal reconstruction efficiency

Combining these systematic errors for each reconstruction modes with appropriate weights, we obtain the overall correction factor (f_c) for the MC signal efficiency as follows.

$$f_c = 0.910 \pm 0.102 \tag{5.14}$$

The break down of the error is listed in Table 5.10. We use the corrected efficiency (ϵ_{data}) for branching fraction calculation, and error on correction factor (f_c) is added up to the systematic error.

	error (%)
tracking	$^{+4.7}_{-4.6}$
$K^{\pm}$ ID	± 1.8
$\pi^{\pm}$ ID	± 1.1
K^0_S ID	± 1.2
π^0 ID	± 3.1
photon ID	± 5.3
SFW and π^0/η veto	± 6.8
best candidate selection	± 2.4
MC statistics	± 3.0
Total	± 10.2

Table 5.10: Summary of systematic errors on signal efficiency.

5.3 Summary of signal reconstruction efficiency

Our signal reconstruction efficiency is first estimated by MC and tested with control data sample. Based on the Kagan-Neubert model, theoretical uncertainty on the efficiency is checked. Our signal reconstruction efficiency for data is determined as follows.

$$\epsilon_{sig} = 2.58 \pm 0.29 \, ^{+0.42}_{-0.39}\% \tag{5.15}$$

where the first error is systematic and the second is theoretical error.

Chapter 6

Conclusions and Discussions

6.1 $\mathcal{B}(B \to X_s\gamma)$

Our signal reconstruction efficiency is obtained in equation 5.15 of section 5.3. It was estimated with MC and corrected for data.

$$\epsilon_{sig} = (2.58 \pm 0.29\ ^{+0.42}_{-0.39})\%.$$

This number includes the efficiency of the `HadronB` selection.

The number of $B\bar{B}$ pairs analyzed was decided from the Fox-Wolfram's R_2 distribution as discussed in section 3.2.1.

$$N_{B\bar{B}}^{\texttt{HadronB}} = (6.07 \pm 0.01\ ^{+0.15}_{-0.12}) \times 10^6.$$

Since this is the number after the `HadronB` selection, the number of $B\bar{B}$ pairs before the `HadronB` selection should be $N_{B\bar{B}}^{\texttt{HadronB}}$ divided by the `HadronB` efficiency ($\epsilon_{\texttt{HadronB}} = 99\%$), or otherwise the ϵ_{sig} must exclude the `HadronB` efficiency.

We have extracted the signal yield in equation 4.2 of section 4.2 by examining the beam constrained mass spectrum.

$$N_{sig}^{observed} = 106.5\ \pm 16.7\ \pm 5.3.$$

From these, the branching fraction for $B \to X_s\gamma$ is

$$\begin{aligned} \mathcal{B}(B \to X_s\gamma) &= \frac{N_{sig}^{observed}}{N_{B\bar{B}}^{\texttt{HadronB}} \times \frac{1}{\epsilon_{\texttt{HadronB}}} \times \epsilon_{sig} \times 2} \\ &= (3.36\ \pm 0.53\ \pm 0.42\ ^{+0.50}_{-0.54}) \times 10^{-4}. \end{aligned} \tag{6.1}$$

where the first error is statistic, the second error is systematic, and the third is theory (model) error.

This result is consistent to the SM prediction [4], and also to the other experimental results [5][6]. Combining the CLEO's recent result [1] (unpublished) in 1998[42]

$$\mathcal{B}(B \to X_s\gamma) = (3.15 \pm 0.35 \pm 0.32 \pm 0.26) \times 10^{-4}. \tag{6.2}$$

and ours, the average branching fraction is

$$\mathcal{B}(B \to X_s\gamma) = (3.21 \pm 0.46) \times 10^{-4}. \tag{6.3}$$

[1] We could hear another updated result at the 4th International Conference on B Physics and CP Violation (BCP4), 19-23 February 2001, Ise-Shima, Japan. <http://www.hepl.phys.nagoya-u.ac.jp/public/bcp4/>

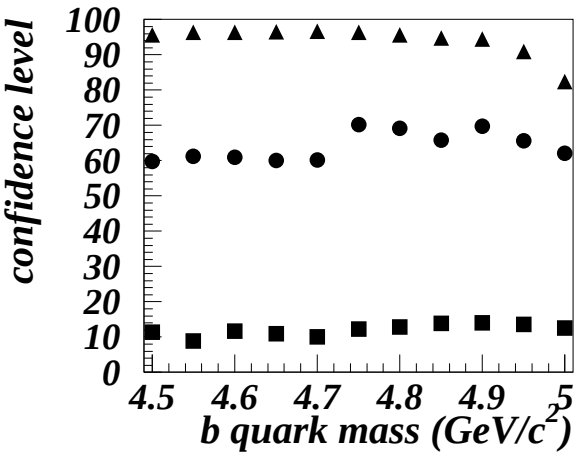

Figure 6.1: Goodness of fit between the predicted spectrum and the observed spectrum – M_B fit (circles), M_{X_s} fit (triangles) and E_γ fit (squares). Either has no power to limit m_b strictly.

6.2 Measurement of the b quark mass m_b

The b quark mass (m_b) is a fundamental parameter of the SM. Various phenomenological studies have suggested the mass in the range of $4.5 \sim 5.0\,\mathrm{GeV/c^2}$. The theoretical model for $B \to X_s\gamma$ by Kagan and Neubert gives different prediction of M_{X_s} or E_γ spectrum for different m_b. We compare the observed spectra with the model to put a limit on m_b.

In the signal yield extraction in section 4.2, we performed a fit for M_B, using signal MC and SFW sideband data. Similarly, we can fit for M_{X_s} and E_γ. Here, $q\bar{q}$ MC is used instead of SFW sideband data since there is a significant correlation between SFW and either of them. The r_{mix} parameter (See, section 4.3.1) is fixed to the value we obtained at $m_b = 4.75\,\mathrm{GeV}$. The fit results are shown in Figure 6.1. Unfortunately, with the current precision of measurement, we could not limit the m_b region.

Another approach is tested as follows. As explained in section 3.2.2, we model the recoil system as a mixture of $K^*(892)$ and higher continuum component. We took the threshold mass (m_{thres}) at $1.15\,\mathrm{GeV/c^2}$ that look reasonable in the observed M_{X_s} spectrum (Figure 4.9). The Kagan-Neubert model [38] originally gives a prediction not only in the higher mass region (above m_{thres}) but also in the lower mass region (below m_{thres}). They (and we) replaced the lower mass region by $K^*(892)$ in order to be more realistic. It means that the integration of the original Kagan-Neubert spectrum upto m_{thres} must be equal to the integration over $K^*(892)$. By changing the m_b parameter, the spectrum changes, and the m_{thres} shifts to give a consistent area. For a higher m_b, the spectrum tends to populate more in lower mass region, and therefore m_{thres} becomes lower. Here, the m_{thres} cannot be under the $K^*(892)$ resonance region, and this fact gives an upper constraint to m_b. We tested the model with m_b from $4.5\,\mathrm{GeV/c^2}$ to $5.0\,\mathrm{GeV/c^2}$ in $0.05\,\mathrm{GeV/c^2}$ step and found that $m_b \geq 4.9\,\mathrm{GeV/c^2}$ are not preferred because the m_{thres} become below $0.95\,\mathrm{GeV/c^2}$.

6.3 Ideas for future improvements

6.3.1 SFW′

Biggest weakness of this analysis is a large theoretical uncertainty. This is mainly due to our cut on M_{X_s}. Currently, our SFW cannot be uncorrelated to M_B without M_{X_s} cut. The most urgent issue is, therefore, to have a better sideband with which we can remove M_{X_s} cut. Using the event shape variable sideband as a $q\bar{q}$ sample is quite a good idea. Our SFW coefficients are tuned so that it gives the maximum signal to background separation. There is still more room to improve the SFW, in sense to have less correlation with M_B. We should tune the SFW so that it gives the minimum correlation with modelate separation power.

6.3.2 Vertex

We do not form a vertex in $K^0_S\pi^0\gamma$ mode. But, if we use a pseud-track of K^0_S, we can form a vertex with the beam profile constraint even for that mode. Also, we can re-fit the momentum of charged tracks, and re-calculate the momentum of photons using the vertex information. This will help to reduce choosing a wrong combination in the best candidate selection, and we will gain the signal reconstruction efficiency.

6.4 Summary

We measured the inclusive branching fraction for the radiative B meson decay $B \to X_s\gamma$ with Belle. The measurement is done semi-inclusively and extrapolated by the theory model of Kagan and Neubert. The measured recoil mass spectrum gave some constraint to the model. To understand the main background, we used the SFW sideband data, relying no longer on the off-resonance data. Therefore, we can expect a quick update of this measurement with smaller errors from Belle.

Appendix A

maximum number of pions for X_s reconstruction

In this analysis, the maximum number of pions to reconstruct X_s is set to four, of which only one π^0 is allowed.

Looking at the beam constrained mass spectrum for each the pion multiplicity shown in Figure A.1(a)-(d), four pion modes are not contributing much for the signal yield already. The maximum number of pions set to four is therefore reasonable.

On the other hand, looking at the beam constrained mass spectrum for each π^0 multiplicity, one π^0 mode still looks yielding the signal, and here comes an idea to allow upto two π^0's.

This idea turned out to be no good. As shown in Figure A.2, low multiplicity modes get cleaner and high multiplicity modes get dirtier than Figure A.1 case[1]. That makes the unbalance between modes larger, and hence the model dependence larger. As for the signal efficiency, it gained in low multiplicity modes, lost in high multiplicity modes, and was a small loss in total.

[1]One apology is that Figure A.1 is for 6.1M$B\bar{B}$ while Figure A.2 is for 5.5M$B\bar{B}$.

(a) one pion modes (b) two pion modes (c) three pion modes

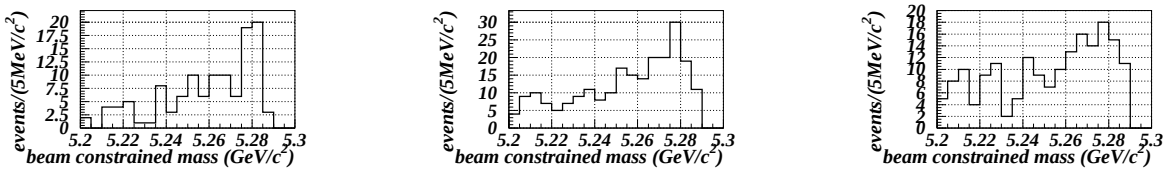

(d) four pion modes (e) zero π^0 modes (f) one π^0 modes

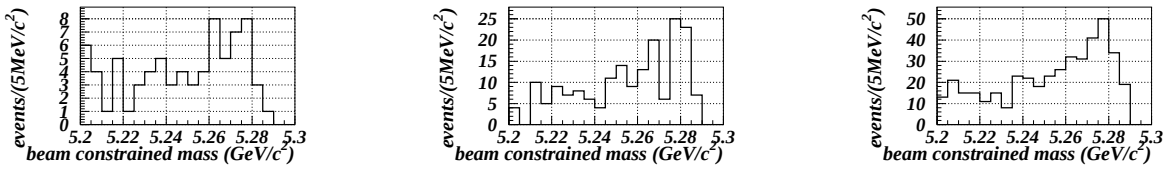

Figure A.1: Raw beam constrained mass with data for each pion multiplicity (background not subtracted) when upto one π^0 is allowed – one (a), two (b), three (c) and four (d) pion mode irrespective to pion charge; and zero (e) and one (f) π^0 mode irrespective to $\pi^{\pm}$ multiplicity.

(a) one pion modes (b) two pion modes (c) three pion modes

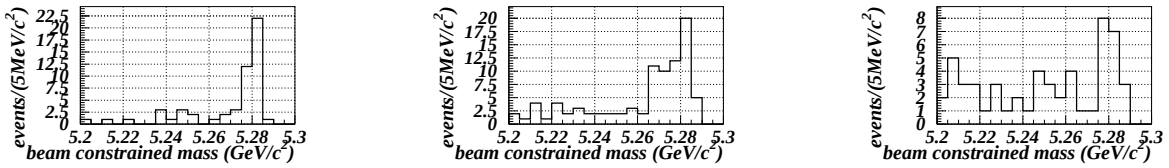

(d) four pion modes

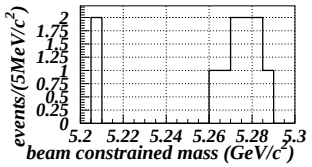

(e) zero π^0 modes (f) one π^0 modes (g) two π^0 modes

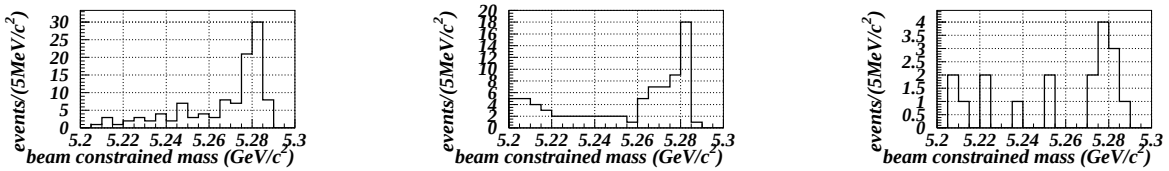

Figure A.2: Raw beam constrained mass distribution with data for each pion multiplicity (background not subtracted) when upto two π^0's are allowed – one (a), two (b), three (c) and four (d) pion mode irrespective to pion charge; and zero (e), one (f) and two (g) π^0's mode irrespective to $\pi^{\pm}$ multiplicity.

Bibliography

[1] J. H. Christenson, J. W. Cronin, V. L. Fitch and R. Turlay, Phys. Rev. Lett. **13**, 138 (1964).

[2] M. Kobayashi and T. Maskawa, Prog. Theor. Phys. **49**, 652 (1973).

[3] J. L. Hewett, hep-ph/9406302.

[4] K.Chetyrkin, M.Misiak, M.Münz, Phys. Lett. **B400**, 206, (1997); Erratum ibid. **B425**, 414, (1998);
A. J. Buras, A. Kwiatkowski and N. Pott, hep-ph/9707482.

[5] CLEO collaboration, Phys. Rev. Lett. **74**, (1995)

[6] ALEPH Collaboration, Phys. Lett. **B429**, (1998)

[7] CLEO III Public Documents,
<http://www.lns.cornell.edu/public/CLEO/CLEO3/CLEO3.html>

[8] The BaBar Homepage, <http://www.slac.stanford.edu/BFROOT/>

[9] Belle HOME PAGE, <http://belle.kek.jp/>

[10] The BTeV Project at Fermilab, <http://www-btev.fnal.gov/btev.html>

[11] HERA-B Home Page, <http://www-hera-b.desy.de/>

[12] LHCb Home Page, <http://lhcb.cern.ch/>

[13] S. Okubo, Phys. Lett. **5**, 165 (1963); G. Zweig, CERN-TH-412; J. Iizuka, Prog. Theor. Phys. Suppl. **37-38**, 21 (1966).

[14] D.E. Groom *el al.*, Eur. Phys. Jour. C **15**, 1 (2000). Update version is available at <http://pdg.lbl.gov/>.

[15] The CLEO Collaboration, Phys. Rev. D **62**, 051101(R) (2000).

[16] J. P. Alexander *et al.* (CLEO Collaboration), Phys. Rev. Lett. **77**, 5000 (1996).

[17] "KEKB B-factory design report", KEK Report 95-7 (1995).

[18] "Accelerator Design of the KEK B-Factory", KEK Report 90-24, (1991).

[19] G. Alimonti et al., Nucl. Instrum. Methods **A453**, 71 (2000).
Belle SVD Group, "Technical Design Report of Belle SVD" (1998).
<http://belle.kek.jp/~svd/tdr/tdr.ps.gz>

[20] H. Hirano et al., Nucl. Instrum. Methods **A455**, 294 (2000); M. Akatsu et al., Nucl. Instrum. Methods **A454**, 322 (2000).

[21] T. Iijima et al., Nucl. Instrum. Methods **A453**, 321 (2000).

[22] H. Kichimi et al., Nucl. Instrum. Methods **A453**, 315 (2000).

[23] H. Ikeda et al., Nucl. Instrum. Methods **A441**, 401 (2000).

[24] A. Abashian et al., Nucl. Instrum. Methods **A449**, 112 (2000).

[25] KEK Progress Report **2000-4**, (2000).

[26] S. Uno, et al., Nucl. Instrum. Methods **A330**, 55 (1993).

[27] S. Uno, et al., Nucl. Instrum. Methods **A374**, 421 (1996).

[28] Belle Collaboration, "Belle progress report 1995 April – 1996 March", KEK Progress Report 96-1 (1996).

[29] Works related to the GDL have mainly been done by Y. Ushiroda. Details of the GDL can be found in Y. Ushiroda's master thesis
<http://belle.kek.jp/bdocs/theses.html>
It is summarized in
Y. Ushiroda et al., Nucl. Instrum. and Methods **A438**, 460, (1999).

[30] for experiment number 3, Y. Ushiroda et al., Belle note **273**, (1999).
for experiment number 5, Y. Ushiroda et al., Belle note **280**, (2000).
for experiment number 7, S. Nishida et al., Belle note **350**, (2000).
for experiment number 9, S. Nishida et al., Belle note **381**, (2001).
for experiment number 11, S. Nishida et al., Belle note **423**, (2001).

[31] K. Hanagaki, M. Hazumi, and H. Kakuno, Belle note **299**, (2000).

[32] <http://www.postgresql.org/>

[33] B. C. K. Casey, Belle note **296**, (2000).

[34] S. Nishida, Belle note **389**, (2001).

[35] A. Ali, C. Greub, Phys. Lett. **B259**, 182, (1991)

[36] The fisher discriminant is used for example in D.M.Asner et al., CLEO collaboration, Phys. Rev. D **53**, 1039 (1996).

[37] C.S.Park, Belle note **339**, 2000

[38] A.L.Kagan, M.Neubert, Eur. Phys. J. **C7**, 5 (1999).

[39] T. Sjöstrand, Comp. Phys. Comm. **82**, 74 (1994).

[40] H. Kakuno and E. Nakano, Belle note **342**, 2000

[41] <http://cbdaq.phy.bnl.gov/Crystalball/crystalball.html>

[42] CLEO Collaboration, CLEO CONF **98-17**, (1998)